



저작자표시-비영리-변경금지 2.0 대한민국

이용자는 아래의 조건을 따르는 경우에 한하여 자유롭게

- 이 저작물을 복제, 배포, 전송, 전시, 공연 및 방송할 수 있습니다.

다음과 같은 조건을 따라야 합니다:



저작자표시. 귀하는 원저작자를 표시하여야 합니다.



비영리. 귀하는 이 저작물을 영리 목적으로 이용할 수 없습니다.



변경금지. 귀하는 이 저작물을 개작, 변형 또는 가공할 수 없습니다.

- 귀하는, 이 저작물의 재이용이나 배포의 경우, 이 저작물에 적용된 이용허락조건을 명확하게 나타내어야 합니다.
- 저작권자로부터 별도의 허가를 받으면 이러한 조건들은 적용되지 않습니다.

저작권법에 따른 이용자의 권리는 위의 내용에 의하여 영향을 받지 않습니다.

이것은 [이용허락규약\(Legal Code\)](#)을 이해하기 쉽게 요약한 것입니다.

[Disclaimer](#)

공학박사 학위논문

# **Synthesis and Characterization of Ternary Selenide Semiconductor Quantum Nanostructures**

삼성분계 셀레늄화 반도체 양자 나노구조의  
합성 및 분석

2016년 8월

서울대학교 대학원

화학생물공학부

양 지 응

# Synthesis and Characterization of Ternary Selenide Semiconductor Quantum Nanostructures

지도 교수 현택환

이 논문을 공학박사 학위논문으로 제출함  
2016년 4월

서울대학교 대학원  
화학생물공학부  
양지웅

양지웅의 공학박사 학위논문을 인준함  
2016년 6월

위원장	성영순	
부위원장	현택환	
위원	김대형	
위원	고민재	
위원	손재성	

## **Abstract**

# **Synthesis and Characterization of Ternary Selenide Semiconductor Quantum Nanostructures**

Jiwoong Yang

School of Chemical and Biological Engineering

The Graduate School

Seoul National University

Designed synthesis and characterization of nanomaterials is of key importance for various applications. Recently, the research focus in nanochemistry has shifted to multi-element nanomaterials with enhanced characteristics and/or multi-functionalities. In this respect, I–III–VI semiconductors and doped II–VI semiconductors are representative classes of materials for both the fundamental studies and future applications. This dissertation describes the synthesis of ternary selenide semiconductor

quantum nanostructures *via* Lewis acid-base reactions and their characterization. In particular, size-controlled Cu–In–Se quantum dots (QDs) have been produced and characterized, and their surface engineering for improved photovoltaic characteristics is discussed. In addition, synthesis and characterization of Mn<sup>2+</sup>-doped CdSe clusters is reported.

First, Cu–In–Se QDs, one of the most representative I–III–VI semiconductor nanomaterials, have been synthesized, and their size-dependent properties are examined. The developed preparation method, which utilizes selenocarbamate as Se precursor, can produce monodisperse Cu–In–Se QDs with diameters ranging from 2 nm to 10 nm. The energy band alignment of the QDs is finely tuned for the optimal position corresponding to the effective light absorption and injection of electrons into TiO<sub>2</sub> electrodes, and the effect of energy-band engineering of the QDs on their photovoltaic characteristics is investigated. Solar cell fabricated using 4 nm-sized Cu–In–Se QDs, which do not contain any toxic element, exhibits the conversion efficiency of 4.30% under one sun light intensity with an air mass 1.5 G (standard conditions).

Second, it has been demonstrated that the photovoltaic characteristics of Cu–In–Se QDs can be significantly enhanced by controlling charge carrier recombination *via* surface engineering of photoelectrodes. In particular,

varying the thickness of ZnS overlayers on QD-sensitized TiO<sub>2</sub> electrodes can noticeably improve their conversion efficiency. With thick ZnS overlayers, both interfacial recombination with the electrolyte and non-radiative recombination from the QDs are significantly reduced, while the energetic characteristics of photoanodes are preserved. The best cell yields the conversion efficiency of 8.10%, which is a record for heavy metal-free QD solar cells (Oct., 2015).

Finally, the last chapter describes the synthesis and characterization of single-sized Mn<sup>2+</sup>-doped CdSe clusters. Mass spectroscopy reveals that these clusters can be assigned to Cd<sub>13-x</sub>Mn<sub>x</sub>Se<sub>13</sub> clusters (x = 0, 1, or 2). Despite their small sizes, the doped clusters exhibit characteristics of diluted magnetic semiconductors. Interestingly, they exhibit multiple excitonic transitions with different magneto-optical activities, which can be attributed to fine structure splitting. Magneto-optically active states show a giant Zeeman splitting with g-factors of 81(±8) at 4 K. The results describe a new synthetic method for doped nanomaterials and facilitate understanding of doped semiconductor at the boundary between molecules and quantum dots.

**Keywords: Ternary Selenide Semiconductor, Quantum Nanostructures, Cu–In–Se, Photovoltaic, CdSe Clusters, Doping, Diluted Magnetic**

**Semiconductor**

**Student Number: 2011-22922**

# Contents

<b>Chapter 1. Multimetallic Selenide Semiconductor Nanocrystals and Dissertation Overview .....</b>	<b>1</b>
1.1 Introduction.....	1
1.2 Fundamentals of Uniform-Sized Colloidal Nanocrystals .....	6
1.3 Previous Studies on Copper–Indium–Selenide Semiconductor Nanocrystals .....	13
1.4 Doping of Semiconductor Nanoclusters: Research Background .....	24
1.5 Dissertation Overview .....	46
1.6 References.....	48
<b>Chapter 2. Synthesis and Size-Dependent Photovoltaic Characterization of Copper–Indium–Selenide Quantum Dots.....</b>	<b>55</b>
2.1 Introduction.....	55
2.2 Experimental Section.....	58
2.3 Result and Discussion.....	64
2.4 Conclusion .....	88
2.5 References.....	89

<b>Chapter 3. Improved Photovoltaic Characteristics of Copper–Indium–Selenide Quantum Dots by Suppressing Carrier Recombination via Surface Engineering .....</b>	<b>95</b>
3.1 Introduction.....	95
3.2 Experimental Section.....	98
3.3 Result and Discussion.....	104
3.4 Conclusion .....	134
3.5 References.....	135
<b>Chapter 4. Synthesis and Characterization of Mn<sup>2+</sup>- doped CdSe Clusters: The Smallest Doped Semiconductor .....</b>	<b>141</b>
4.1 Introduction.....	141
4.2 Experimental Sections .....	143
4.3 Result and Discussion.....	148
4.4 Conclusion .....	165
4.5 References.....	166
<b>Bibliography .....</b>	<b>171</b>
<b>국문 초록 (Abstract in Korean).....</b>	<b>175</b>

# **Chapter 1. Multimetallic Selenide Semiconductor Nanocrystals and Dissertation Overview**

## **1.1 Introduction**

In the last two decades, nanoscience and nanotechnology have attracted a lot of attention. Among various classes of materials, semiconductor nanocrystals have been intensively investigated because of their unique physicochemical properties.<sup>[1]</sup> When the size of a semiconductor is smaller than its Bohr diameter, charge carriers are effectively confined inside the nanocrystal. As a result, their density of states reflect the intermediate states between those of molecules and bulk semiconductors (Fig. 1.1).<sup>[1c]</sup> This phenomenon is called a “quantum confinement effect” and is mainly controlled by the size of semiconductor materials. The most representative example is a bandgap increase with decreasing nanocrystal size (Fig. 1.2).<sup>[1d]</sup> In addition to the size, confinement dimensions also affect the density of states of the nanocrystals (Fig. 1.1b).<sup>[2]</sup> Consequently, size- and shape-controlled synthesis of monodisperse nanocrystals was one of the important issues to exploit the potential of semiconductor nanocrystals with desired properties. Recently, the

research focus has rapidly shifted to multi-element nanomaterials with enhanced performance and/or multi-functionalities.<sup>[3]</sup> In contrast to binary compounds, the synthesis of multi-element inorganic nanocrystals is more challenging. It requires delicate synthetic control over the reaction between multiple elements. If the synthetic conditions are not well established, a mixture of undesired phases is produced. Due to the increasing reaction complexity, the development of novel synthetic routes is highly required.

Ternary I–III–VI Cu–In–Se compounds are important semiconducting materials, which contain three or more chemical elements.<sup>[4]</sup> Since these compounds have a direct band gap, which allows for solar energy absorption, they have been intensively studied for bulk thin film photovoltaic applications.<sup>[5]</sup> In addition, they do not contain heavy metal elements and thus represent promising alternatives to toxic Cd- and Pb-based conventional II–VI and IV–VI semiconductor quantum dots (QDs). However, the synthetic chemistry of I–III–VI semiconductor nanocrystals has not been investigated in detail, while various synthetic methods were established for binary II–VI semiconductor materials. As a result, photovoltaic characteristics of I–III–VI QDs have not been obtained, although they represent an important class of bulk thin film photovoltaics.

On the other hand, doped semiconductor nanocrystals have been recognized

as a class of multi-element semiconductor nanomaterials.<sup>[6]</sup> Doping, the process of controlled incorporation of impurities into a host matrix, is widely used in the modern semiconductor field, providing additional means of tuning nanocrystal properties. However, doping of semiconductor nanocrystals is very inefficient as compared to bulk counterparts.<sup>[7]</sup> In particular, doping of extremely small-sized ( $< 2$  nm) semiconductor particles has not been reported yet. It is still an open question whether this difficulty is related to the great synthetic issues or the more fundamental consequence of doping ultra-small semiconductor species themselves.

This chapter focuses on the research background and recent advances in the synthesis and characterization of ternary semiconductor nanocrystals. In particular, the preparation and properties of I–III–VI and doped II–VI semiconductor nanocrystals will be discussed in detail.

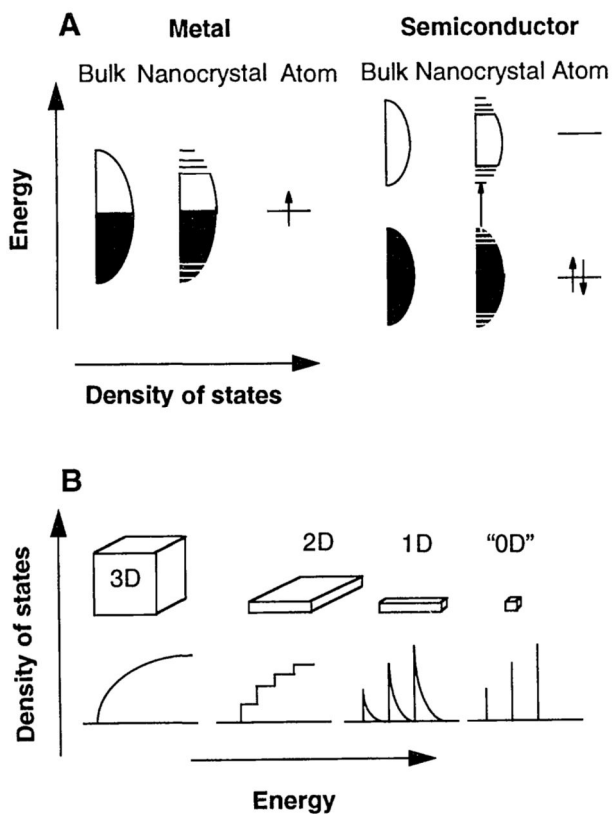


**Figure 1.1** (a) A schematic illustration describing the density of states for bulk semiconductors, semiconductor nanocrystals, and atoms. (b) A schematic illustration describing the density of states for semiconductor particles with 3, 2, 1, and 0 dimensions. The figure is reproduced with permission from Ref. [1b], American Association for the Advancement of Science.

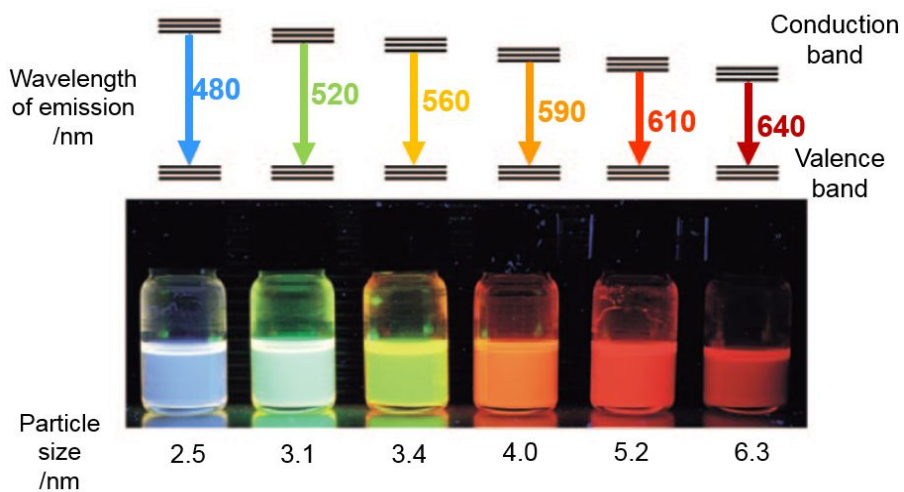


**Figure 1.2** Optical images of CdSe nanocrystal solutions with various particle sizes. The figure is reproduced with permission from Ref. [1c], John Wiley and Sons.

## 1.2 Fundamentals of Uniform-Sized Colloidal Nanocrystals

Prior to discussing the synthesis of multielement nanocrystals, it is imperative to understand fundamentals of the synthesis of uniformly sized nanocrystals. Monodisperse colloidal nanocrystals of various materials have been synthesized *via* different reaction pathways, including thermal decomposition, reduction, and non-hydrolytic sol-gel reactions. The ultimate generation of monodisperse nanocrystals through a variety of reaction pathways suggests the existence of a common mechanism for the formation of colloidal nanocrystals, which is independent of materials and/or reaction conditions.<sup>[8]</sup> The colloidal synthesis of nanocrystals usually consists of three steps: formation of monomers, nucleation, and final growth. This three-step mechanism is similar to that described by the LaMer model (Fig. 1.3), which was initially developed in the 1940s to characterize monodisperse hydrosol systems.<sup>[8a,9a-c]</sup>

In order to synthesize nanocrystals in solution, their nuclei must be generated so that further growth can occur.<sup>[9]</sup> These “seeds” can be either generated in a reaction mixture or introduced externally. The former reaction method, a homogeneous nucleation process, is widely used for the colloidal

synthesis of nanocrystals. The second route is known as a heterogeneous nucleation process and is less common for colloidal synthesis due to the difficulty of preparing uniform-sized nuclei.

Fig. 1.4a shows two different cases of homogeneous nucleation. When nucleation occurs randomly throughout the entire synthetic process, all crystals exhibit different growth profiles, ultimately resulting in polydisperse nanocrystals with a broad size distribution. In contrast, when all nuclei are generated at once, the crystals will grow under the same conditions during the reaction and the final product will be uniform in size. In other words, all crystals in a batch will have the same growth history. Therefore, a single-step nucleation step (separated from the growth process) is ideal for the synthesis of monodisperse nanocrystals.

In practice, a typical situation is different from the ideal single-event nucleation. During the actual reaction, nuclei are generated within a certain period, rather than in a single event. Consequently, the increase in the number and size of produced nanoparticles is inevitably accompanied by the broadening of their size distribution. The observed size deviation reaches maximum at the end of the nucleation step (Fig. 1.4b). Therefore, the nucleation process should be rapidly terminated and separated from the growth step in order to produce monodisperse nanocrystals. To initiate a

homogeneous and instantaneous nucleation process, high supersaturation is required, which can be achieved through the accumulation of monomer species prior to nucleation. When supersaturation reaches a critical point (*i.e.*, minimum supersaturation level for homogeneous nucleation), the nucleation process starts (Fig. 1.3). After that, the nucleation and subsequent growth rapidly alleviate the achieved supersaturation level by consuming monomers. The fast monomer consumption observed in these processes suppresses additional nucleation events during the remaining reaction period, and eventually, the nucleation process self-terminates. The described self-regulating nature of the nucleation process minimizes the required time for the nucleation. As a result, all crystals in the system have nearly identical growth histories, which is close to the ideal single-nucleation event. Such a “burst” nucleation process represents a key strategy for the synthesis of highly uniform nanocrystals.<sup>[8]</sup>

In addition to the burst nucleation process, additional control of the nanocrystal size distribution can be achieved during the growth stage. The growth of nanocrystals is largely affected by the competition between two reversible processes: solute precipitation onto the surface of nanocrystals and nanocrystal dissolution. When the precursor concentration significantly exceeds the solubility of nanocrystals, the growth rate is determined by the

solute diffusion rate from the bulk solution medium to the nanocrystal surface (diffusion-controlled mode). In this case, the dissolution of nanocrystals is negligible, and the solute species diffuse to the precipitates deposited on the nanocrystal surface. The size of colloidal nanocrystals is one of the most important parameters affecting their growth rate. According to the diffusion-controlled growth model, the amount of a solute required for diffusion and the related increase in the unit radius ( $dr$ ) are approximately proportional to  $r^2$  and  $r^3$ , respectively. Therefore, the growth rate (the increase in radius per unit time,  $dr/dt$ ) decreases as the crystal radius increases. This leads to a faster growth of smaller crystals, which in turn results in a narrow size distribution at the end of the growth step (Fig. 1.4b). This process is called “size focusing” of nanocrystals.<sup>[10]</sup>

The foregoing discussion is based on the diffusion-controlled growth model, which is not always applicable. When the solute concentration is much lower than the solubility of nanocrystals, nanocrystal dissolution can occur. In this case, some colloidal nanocrystals dissolve, while others continue growing. According to the Gibbs–Thomson relationship, when particles become smaller, their chemical potential increases. Therefore, the dissolution reaction is dominant for small-sized nanocrystals at low solute concentrations. Meanwhile, large nanocrystals are so stable that they continue growing by

acquiring the solute species released into the solution from the dissolved nanocrystals. During this process, known as “Ostwald ripening”, both the solute and nanocrystal concentrations generally decrease, while the particle mean size increases (please note that the discussion presented above represents only a very brief conceptual explanation).

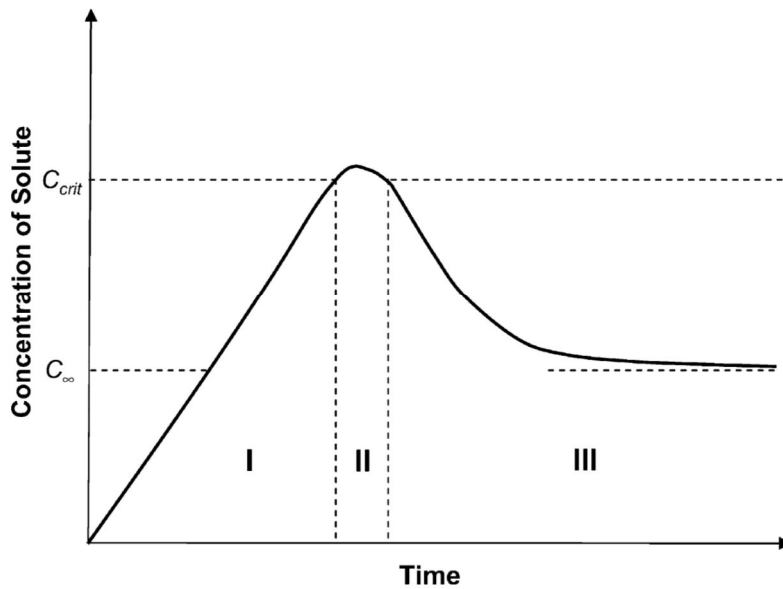


**Figure 1.3** The LaMer diagram describing the changes in the supersaturation level at different crystallization stages.  $S_c$  is the critical supersaturation level. The figure is reproduced with permission from Ref. [8a], Elsevier.

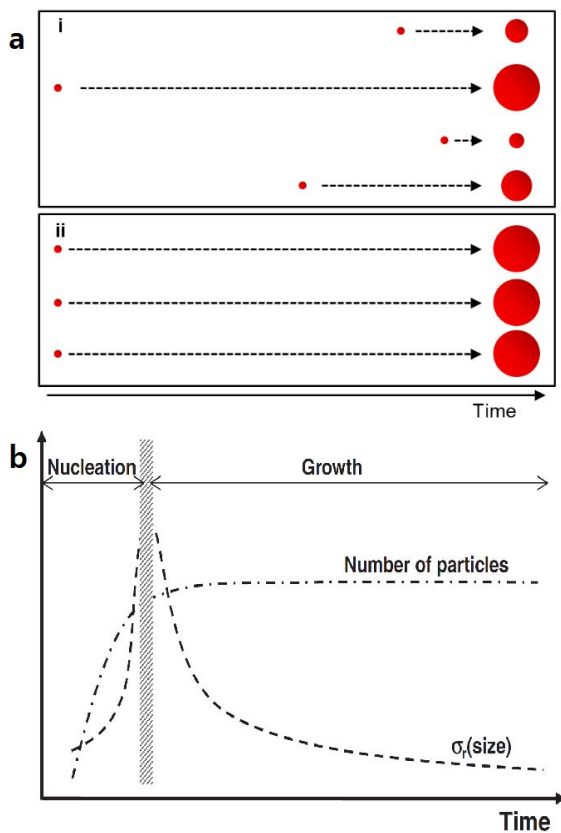


**Figure 1.4** (a) Crystallization reaction systems for two distinctive cases, in which homogeneous nucleation processes occur either randomly (i) or simultaneously (ii). (b) Time evolution of the number of nanoparticles, relative standard deviation of the size distribution ( $\sigma$ ), and size ( $r$ ) of the nanocrystals during nucleation and growth. The thick vertical shaded line represents the point, at which the nucleation process is terminated, thus separating the nucleation and growth steps. The figure is reproduced with permission from Ref. [8c], John Wiley and Sons.

## 1.3 Previous Studies on Copper–Indium–Selenide Semiconductor Nanocrystals

### 1.3.1 Copper–Indium–Selenide Ternary Semiconductors

I–III–VI semiconductor materials are multimetal chalcogenide semiconductors, which usually contain two metals of group I and III elements and a chalcogen from group VI elements. One of the most representative I–III–VI semiconductors is Cu–In–Se. Bulk Cu–In–Se compounds are usually described by the chemical formula  $\text{CuInSe}_2$  and can be modified to produce  $\text{CuIn}_x\text{Ga}_{(1-x)}\text{Se}_2$  ( $x < 1$ ) when In is replaced with Ga.<sup>[5]</sup> The crystallographic structure of  $\alpha$ -CuInSe<sub>2</sub> corresponds to the chalcopyrite crystal structure shown in Fig. 1.5. In this structure, atoms are located at the sites identical to those for the zinc blende structure, while the size of its unit cell is twice as large as that of the zinc blende one.  $\text{Cu}^+$  and  $\text{In}^{3+}$  ions alternatively occupy the cation sites, which are tetrahedrally connected to  $\text{Se}^{2-}$  ions. Cu vacancies are easily formed, and the entire structure can be transformed into its  $\beta$ -phase with a stoichiometry of  $\text{CuIn}_3\text{Se}_5$ , containing ordered Cu defect sites (Fig. 1.5).

Cu–In–Se has a direct band gap of around 1 eV, which is suitable for solar light absorption. In particular, the absorption coefficient for these materials

exceeds  $3 \times 10^4 \text{ cm}^{-1}$  at wavelengths below 1000 nm, indicating that a much thinner Cu–In–Se film is required (in contrast to other semiconductor materials). Furthermore, the band gap can be varied from 1.0 eV to 1.7 eV by forming solid solutions with Cu–Ga–Se species. Hence, these compounds have been actively utilized for fabricating thin film photovoltaics, which can be categorized as the second generation solar cells. A typical structure of the Cu–In–Ga–Se (CIGS) solar cells is shown in Fig. 1.6). The record efficiency achieved for Cu–In–Se solar cells exceeds 20%, which is comparable to that obtained for Si-based devices.<sup>[5f]</sup>

Because of the excellent opto-electronic properties of bulk Cu–In–Se and low toxicity of its constituent elements, Cu–In–Se is promising alternatives to the conventional heavy metal-based QDs. However, the development of synthetic methods for Cu–In–Se colloidal QDs is very challenging since the synthesis of I–III–VI nanocrystals requires a balance of the reactivity of two metallic cations toward an anion precursor, which is more difficult to control (as compared to that for binary systems). Because the reaction between Cu, In, and Se produce various phases (Fig. 1.5c), undesired byproducts can be formed. In the following sections, previous studies on the synthesis and characterization of Cu–In–Se colloidal nanocrystals are reviewed.

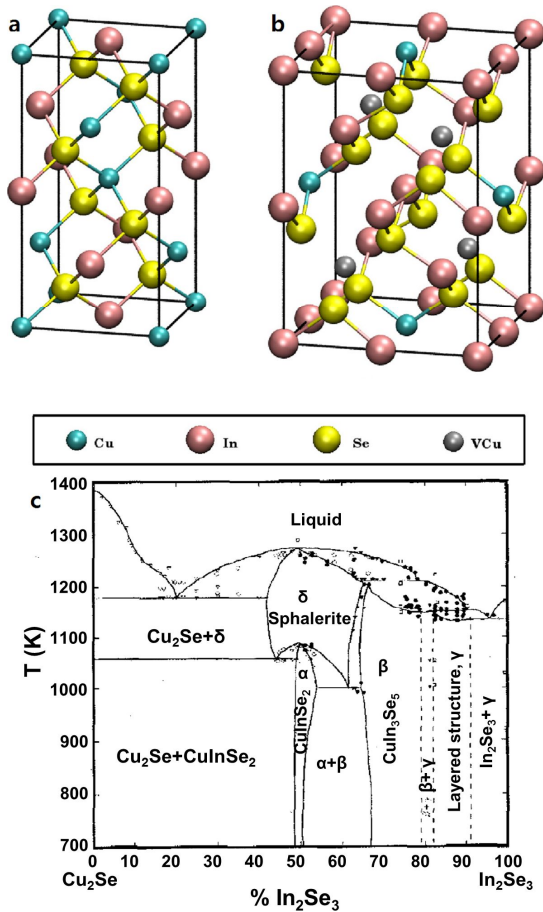


**Figure 1.5** A schematic illustration describing the unit cells of (a)  $\alpha$ -CuInSe<sub>2</sub> (the chalcopyrite structure) and (b)  $\beta$ -CuIn<sub>3</sub>Se<sub>5</sub>.<sup>[5e]</sup> (c) A pseudo-binary In<sub>2</sub>Se<sub>3</sub>-Cu<sub>2</sub>Se equilibrium phase diagram. Panels a and b are reproduced with permission from Ref. [5e], American Chemical Society. Panel c is reproduced with permission from Ref. [5a], IEEE.

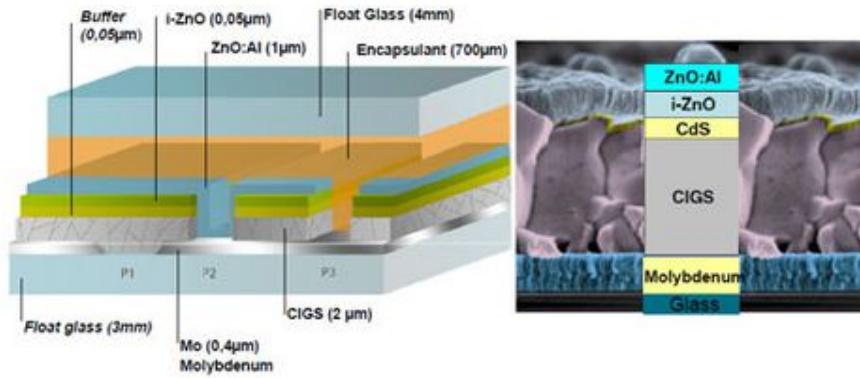


**Figure 1.6** A typical device structure of the Cu–In–Ga–Se (CIGS) thin film solar cells. The figure is reproduced with permission from Ref. [5g], Manz AG.

### **1.3.2. Colloidal Synthesis of Cu–In–Se Semiconductor Nanocrystals**

Cation precursors utilized for the synthesis of Cu–In–Se nanocrystals are usually limited to metal halides because of their high reactivity and high solubility during complexation with organic molecules. Thus, the development of an efficient Cu–In–Se synthesis procedure is closely related to the proper choice of a Se precursor.

In the initial reports on the synthesis of Cu–In–Se nanocrystals, the reaction between metal halides and elemental Se was typically conducted in oleylamine solvents.<sup>[4a,b]</sup> Because the reactivity of the elemental Se in oleylamine is low, this reaction cannot effectively separate the nucleation and growth, which results in the formation of large and non-quantum confined nanocrystals with very broad size distributions. Thus, the produced nanocrystals cannot be considered as QDs and they cannot utilize the benefits originating from the quantum confinement effect. These Cu–In–Se nanocrystals are mainly used as precursors for fabricating thin films with/without a sintering stage, which reduce the production cost of Cu–In–Se thin film solar cells. The resulting photovoltaic performance of a device is very poor, because the grain size of the produced film is very small (as compared to that of the general thin film solar cells).

A successful size-controlled synthesis of Cu–In–Se quantum confined

nanocrystals was reported by the Bawendi group.<sup>[4c]</sup> They used very reactive bis(trimethylsilyl) selenide ((TMS)<sub>2</sub>Se) as a Se precursor to obtain quantum sized Cu–In–Se QDs. The reaction was conducted utilizing a so-called “hot-injection method”, which involved the injection of (TMS)<sub>2</sub>Se into a mixture of metal halides with oleylamine and trioctylphosphine ligands at a temperature of around 300 °C. The obtained products had various compositions ranging from CuIn<sub>1.5</sub>Se<sub>3</sub> to CuIn<sub>5</sub>Se<sub>8</sub> and a band gap spanning over the region between the red and near infrared wavelengths (from 640 nm to 975 nm), as shown in Fig. 1.7. However, Se precursors are very hazardous and difficult to synthesize, and the described method is therefore not applicable for the large-scale synthesis of Cu–In–Se QDs, which is critical for practical applications only tens of milligrams of the final product were obtained from a single batch.

The Dubertret group reported another method for synthesizing Cu–In–Se QDs, which employed selenourea as a selenium precursor.<sup>[4d]</sup> Selenourea is a very reactive reagent containing a resonance-stabilized selenoketone (selone) with  $\pi$ -conjugation between the selenocarbonyl and amino groups (Fig. 1.8a). By heating selenourea in a mixture of CuI and InCl<sub>3</sub> with trioctylphosphine (TOP), oleylamine, and dodecanethiol ligands, the Cu–In–Se QDs were produced. The products cover wavelength from 700 nm to 1100 nm. Selenourea is very sensitive to heat, moisture, and even light and easily

decomposes into red elemental Se<sup>[11a]</sup> or forms diseleno bis(formamidinium) cations.<sup>[11b]</sup> Hence, the described method is also not appropriate for the large-scale synthesis of Cu–In–Se QDs. After the formation of a core/shell structure with ZnS shells, the synthesized QDs were utilized for bio-imaging (Fig. 1.8b,c), which requires a relatively little amount of QDs (as compared to electronic device applications).

More recently, several groups have developed a synthetic method for Cu–In–Se QDs utilizing alkylphosphine selenide as a Se precursor, which is generally used for the synthesis of other conventional QDs. Trioctylphosphine,<sup>[4e]</sup> tributylphosphine,<sup>[4f]</sup> and diphenylphosphine<sup>[4g]</sup> are used for the preparation of Se precursors and ligands with/without thiols, which suppress the growth of QDs. In particular, when diphenylphosphines are employed, QDs can be obtained without the use of thiols or S incorporation, which may possibly lead to the formation of Cu–In–S phases. However, all alkylphosphines are very toxic substances and remain on the product surface as passivating ligands, indicating that the resulting QDs are harmful and cannot be considered good alternatives to the conventional toxic QDs.

As have been mentioned earlier, the synthesis of Cu–In–Se QDs represents a great challenge compared to that of the well-developed conventional QDs. Consequently, the previous studies of their photovoltaic characteristics of

Cu–In–Se QDs were very limited. In the majority of the previously reported works, they were used as non-quantum confined nanocrystals and thus were unable to provide scientific insights for Cu–In–Se-based QD solar cells. The Korgel group reported Cu–In–Se QD thin film solar cells with the glass/Au/Cu–In–Se QD/CdS/ZnO/ITO configuration (Fig. 1.9).<sup>[4g]</sup> However, their photoconversion efficiency was only around 1%. Furthermore, the fabricated device used CdS buffer layers for effective operations, which virtually eliminated the benefits of utilizing heavy-metal free QDs.

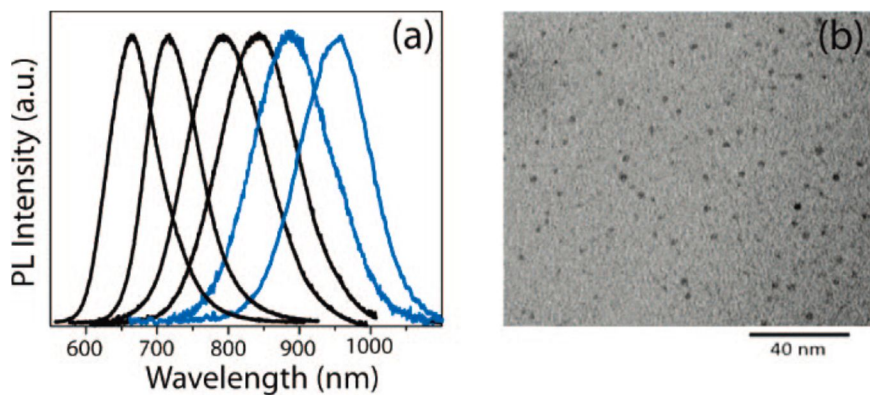


**Figure 1.7** (a) Photoluminescence spectra of  $\text{CuIn}_5\text{Se}_8$  QDs (with mean diameters from 2.0 to 3.5 nm; black) and  $\text{CuIn}_{2.3}\text{Se}_4$  QDs (with mean diameters from 3.0 to 3.5 nm; blue) synthesized from  $(\text{TMS})_2\text{Se}$ . (b) A transmission electron microscopy (TEM) image of  $\text{CuIn}_{2.3}\text{Se}_4$  QDs with a mean diameter of  $3.0 \pm 0.5$  nm. The figure is reproduced with permission from Ref. [4c], American Chemical Society.

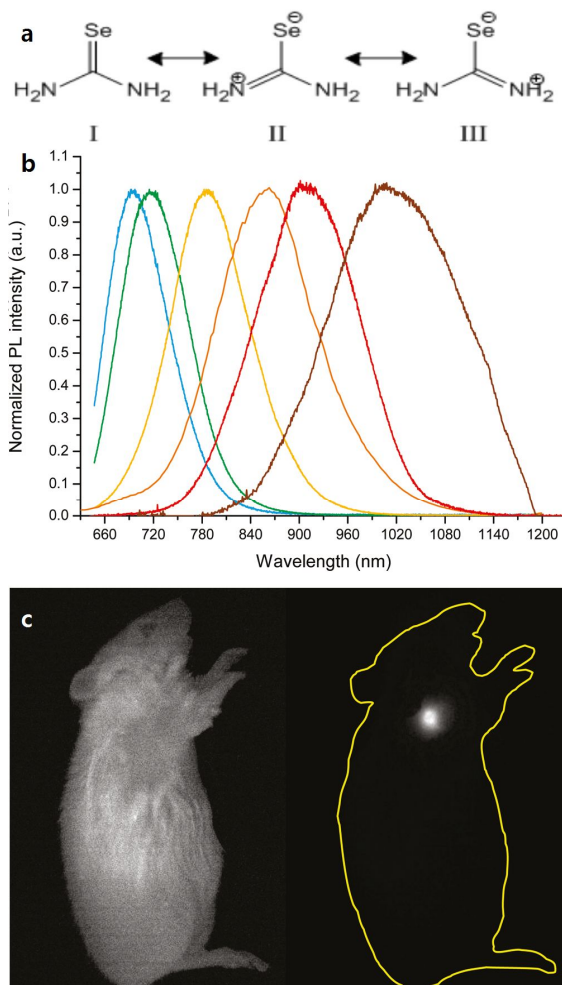


**Figure 1.8** (a) Resonance structures of selenourea. (b) Photoluminescence spectra of  $\text{CuInSe}_2/\text{ZnS}$  QDs fabricated by using selenourea. (c) *In vivo* fluorescence imaging of a mouse before (left) and 4 h after the injection of  $\text{CuInSe}_2/\text{ZnS}$  QDs (right). The figure is reproduced with permission from Ref. [4d], American Chemical Society.

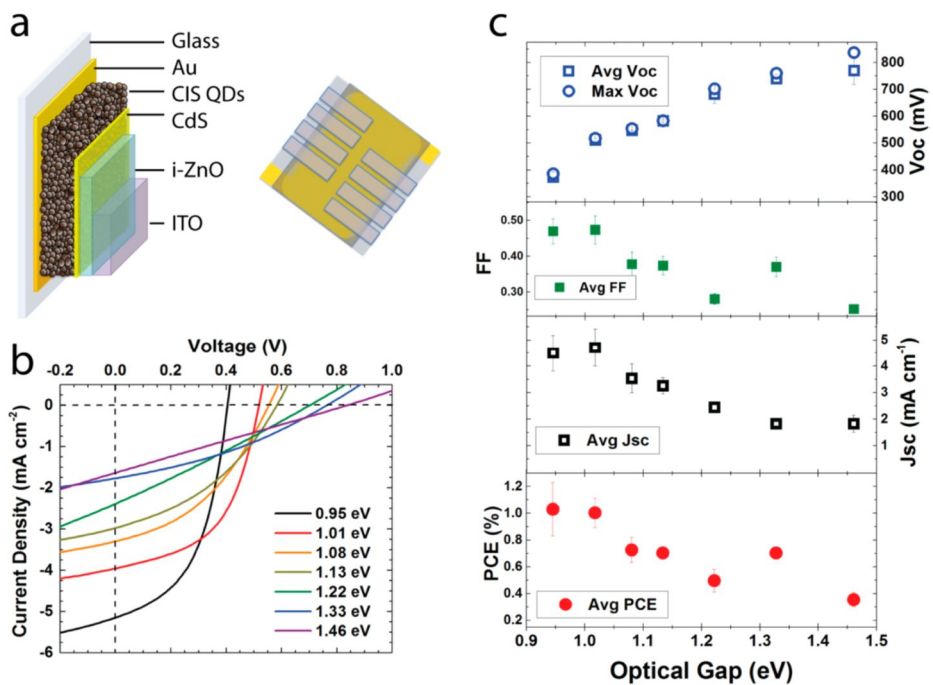


**Figure 1.9** (a) A device structure for Cu–In–Se QD solar cells. Dependences of the (b)  $J$ – $V$  and (c) representative photovoltaic characteristics of Cu–In–Se QD solar cells on the optical band gap. The figure is reproduced with permission from Ref. [4g], American Chemical Society.

## 1.4 Doping of Semiconductor Nanoclusters: Research Background

### 1.4.1 Nanoclusters

#### 1.4.1.1 What is Nanoclusters?

Nanoclusters are aggregates of tens to hundreds of atoms. One important characteristic shared by various kinds of cluster molecules – nanoclusters, including metals,<sup>[12a]</sup> polyoxometalates,<sup>[12b]</sup> and metal chalcogenides,<sup>[12c]</sup> is the presence of the discrete structures consisting of a ‘magic number’ of atoms with extra stability. For bare metal clusters, the stability of these magic clusters is explained in terms of geometric closed shell structure.<sup>[12d-g]</sup> By forming a complete closed shell of close-packed atoms with no vacancies at the surface of symmetric polyhedron shapes (that is, Platonic solids), the clusters reach the maximum structural stability for a certain number of constituting atoms. The next-largest cluster can be constructed by depositing another complete layer of atoms on the surface of the cluster, which leads to a discrete increase in the number of atoms in each subsequent magic cluster. As an example, a homologous series of cuboctahedron clusters (where the number of atoms,  $n$ , in each cluster is written as  $n = 10/3 K^3 - 5 K^2 + 11/3 K - 1$ , where  $K$  is the number of atomic shells) is shown as an example in Fig.

1.10.<sup>[12g]</sup> These structures have been generally observed from clusters of Au and other platinum group metals. It should be noted that although they have symmetric ordered structures, some magic clusters are non-crystalline. Icosahedron and decahedron clusters, for example, consist of highly strained *fcc* subunits, and their five-fold symmetry does not belong to the Bravais lattice system. As a result, further growth of the clusters into crystals requires atomic rearrangements to fulfill the translational symmetry condition.

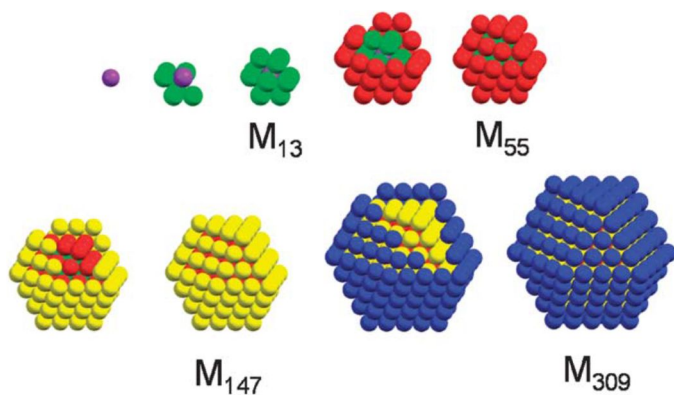


**Figure 1.10** The illustration showing the cuboctahedron full-shell clusters. A central atom (purple) is surrounded by close-packed shells of atoms. One-shell ( $K = 2$ ,  $K$ : number of atomic layers) clusters have 13 atoms and two-shell ( $K = 3$ ) clusters 55 atoms, and so on. The figure is reproduced with permission from Ref. [12g], Royal Society of Chemistry.

### 1.4.1.2 Size-Dependent Characteristics of Nanoclusters

An interesting structural evolution from molecules to crystalline solid was reported<sup>[13a]</sup> for a series of dodecanethiol-passivated Au<sub>n</sub> clusters, synthesized in the range n = 38 ~ 520. By standardizing the ligand effect, which can alter the structure of the clusters,<sup>[13b]</sup> it is possible to monitor the systematic transition of Au<sub>n</sub> clusters from a non-*fcc* to an *fcc* structure as a function of their size (Fig. 1.11a). This structural transition occurs in the size range n = 144 ~ 187. In the same size range, optical absorption spectra show a transition from a molecule-like discrete electronic structure to a bulk-like localized surface plasmon resonance. Consistently, a molecule-like electronic energy transition in Au<sub>n</sub> clusters with n < 144 has been reported.<sup>[13]</sup>

Similarly, CdSe clusters of various sizes and with the same structure as motif of bulk CdSe structure have been synthesized.<sup>[14]</sup> For example, three pyramidal CdSe clusters with a zinc blende structure — [Cd<sub>35</sub>Se<sub>20</sub>(O<sub>2</sub>CPh)<sub>30</sub>(H<sub>2</sub>N-C<sub>4</sub>H<sub>9</sub>)<sub>30</sub>], [Cd<sub>56</sub>Se<sub>35</sub>(O<sub>2</sub>CPh)<sub>42</sub>(H<sub>2</sub>N-C<sub>4</sub>H<sub>9</sub>)<sub>42</sub>], and [Cd<sub>84</sub>Se<sub>56</sub>(O<sub>2</sub>CPh)<sub>56</sub>(H<sub>2</sub>N-C<sub>4</sub>H<sub>9</sub>)<sub>56</sub>] — have been reported recently (FIG. 1.11b).<sup>[12c]</sup> On the other hand, [Cd<sub>32</sub>Se<sub>14</sub>(SePh)<sub>36</sub>(PPh<sub>3</sub>)<sub>4</sub>] clusters have a mixed structure with both zinc blende and wurtzite motifs.<sup>[12c]</sup> When plotted against the cluster size, the optical band gap of these clusters coincides with the extrapolation of the band gap as a function of the size of CdSe nanoparticles

(Fig. 1.11b),<sup>[14a,b,d]</sup> showing that the size-dependent quantum confinement effect is valid for these clusters. Owing to a low density of states at the band edge, a discrete energy structure is observed not only in semiconductor clusters, but also in nanoparticles of a few nanometers, which is in contrast to what is observed in metal clusters. For this reason, semiconductor nanoparticles are also called ‘artificial atoms’.

In the case of metal oxides, many clusters that are prototypical to metal oxide solids were found from polyoxometalate compounds.<sup>[15a-c]</sup> Polyoxometalate clusters usually consist of transition metal cations (M) and oxygen atoms surrounding a heteroatom (X), such as Keggin ( $\text{XM}_{12}\text{O}_{40}$ ),<sup>[15d]</sup> Wells-Dawson ( $\text{X}_2\text{M}_{18}\text{O}_{62}$ ),<sup>[15e]</sup> and Anderson ( $\text{XM}_6\text{O}_{24}$ )<sup>[15f]</sup> clusters.

It is interesting to observe that both the expression ‘super atoms’ for metal clusters, and ‘artificial atoms’ for semiconducting nanoparticles, can have two meanings. These terms were originally introduced because of the similarity between nanoparticles and atoms, in the sense that both have quantized electronic energy states. This analogy was immediately extended to the other defining property of atoms, that is, that they constitute the building units of bulk solids. Although the formation of ‘artificial molecules’ has not yet been fully realized because of the weak quantum exchange coupling between neighboring artificial atoms, the idea of using clusters and nanoparticles as the

building units of solids has contributed to the study of nonclassical crystallization, in which crystal formation proceeds not by addition of individual atoms or ions but by assembly of clusters or small nanoparticles. The role of clusters and nanoparticles as building units in the nucleation and growth process will be discussed in the next two sections.

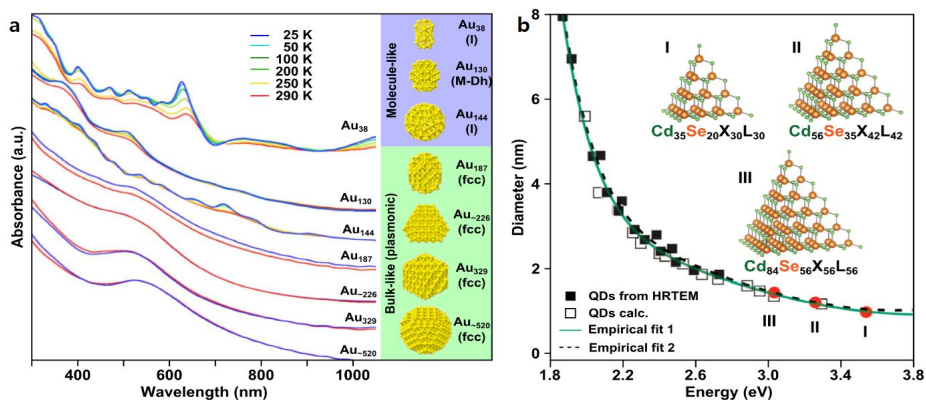


**Figure 1.11** (a) Evolution of optical absorption spectra of Au clusters with various sizes, measured at different temperatures.  $Au_n$  clusters with  $n = 38$ , 130, and 144 show discrete energy states in the spectra and have icosahedral (I) or Marks decahedral (M-Dh) structures, whereas the clusters with  $n = 187$ , ~226, 329, and ~520 have plasmonic resonances originating from their metallic band structure and a face centered cubic (*fcc*) structure. (b) Size dependence of the band gap energy of CdSe nanoparticles and clusters. The structures of the clusters are shown in the inset and their band gap energies are indicated as red dots in the plot. Empirical fit 1 is calculated for data points of both nanoparticles and clusters whereas empirical fit 2 for only nanoparticles. The nanoparticle data and empirical fit 2 are from Ref. [14e] (a.u.: arbitrary units). Panels a is reproduced with permission from Ref. [13a], American Chemical Society. Panel b is reproduced with permission from Ref. [14b], American Chemical Society.

### 1.4.1.3 Nanoclusters during Pre-nucleation Stage

It is well known that nanoclusters with discrete sizes and structures form during the prenucleation period of the synthesis of nanoparticles of various metals,<sup>[16a]</sup> semiconductors,<sup>[16b-d]</sup> and metal oxides<sup>[16e]</sup> (Fig. 1.12). The formation of these nanoclusters reveals the presence of local minima in the energy landscape, which can effectively lower the energy barrier for nucleation, so that it can take place at a level of supersaturation lower than that estimated by classical nucleation theory.<sup>[16f]</sup> Nanoclusters formed during nanoparticle synthesis are usually meta-stable and exist transiently before growing into nanoparticles, making them difficult to characterize. Interestingly, the formation of prenucleation clusters does not always proceed from the smaller to the larger ones. For example, in the early stage of CdSe nanoribbons synthesis, alkylamine-passivated  $(\text{CdSe})_{34}$  clusters are transiently observed before the smaller  $(\text{CdSe})_{13}$  clusters (Fig 1.12c).<sup>[16d]</sup> This example suggests that the energetics of prenucleation clusters is much more complicated than the picture given in the classical nucleation model.

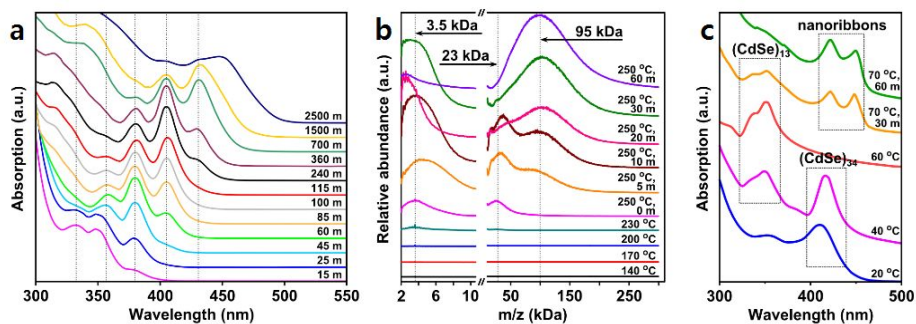


**Figure 1.12** (a) Time dependency of absorption spectra of the reaction mixture during the synthesis of CdSe nanoparticles. Vertical lines indicate absorption peaks corresponding to discrete magic-sized CdSe clusters.<sup>[16b]</sup> (b) Mass spectra of the reaction mixture during the synthesis of iron oxide nanoparticles. Two different mass ranges are selected for clarity. The peaks at 3.5 kDa, 23 kDa, and 95 kDa are attributed to  $\text{Fe}_8(\text{oleate})_{11}$  clusters and to 1.9 nm and 3.3 nm nanoparticles, respectively.<sup>[16e]</sup> (c) Absorption spectra from the reaction mixture during the synthesis of CdSe nanoribbons.<sup>[16d]</sup> The panel a is reproduced with permission from Ref. [16b], John Wiley and Sons. The panel b is reproduced with permission from Ref. [16e], American Chemical Society. The panel c is reproduced with permission from Ref. [16d], Nature Publishing Group.

## **1.4.2 Previous Studies on Nanocrystal Doping**

### **1.4.2.1 Challenges of Nanoscale Doping**

Doping is the process of intentional incorporation of impurities into host materials. This technique has been widely adopted in the modern semiconductor industry, because it provides practical means of controlling host properties. For example, the incorporation of III or V group elements into a Si matrix results in p- or n-type characteristics, which are useful for many applications. Hence, doping of semiconductor nanocrystal has attracted significant interest. In addition to the unique properties of semiconductor nanocrystals resulting from their size and shape, nanocrystal doping provides an additional degree of control over their characteristics, such as electronic, optical, and magnetic properties.<sup>[6,7,17,18]</sup> For example, magnetic impurity-doped semiconductor nanocrystals (so-called diluted magnetic semiconductor nanocrystals) are considered as promising candidates for spintronic applications,<sup>[18]</sup> because their spin states can be easily manipulated on the nanoscale to achieve desirable characteristics such as strong magneto-optical response. These characteristic properties originate from the spin-exchange interactions between the dopants and the charge carriers of the host material.

Because nanoclusters are believed to play a unique role in the synthesis of nanocrystals, doping of nanoclusters may suggest new pathways for the

nanoscale doping process. In addition, the study of doped clusters can facilitate new understandings of the new class of materials between nanocrystals and molecules. However, doping becomes more difficult at smaller sizes of host material particles. For example, the synthesis of  $\text{Mn}^{2+}$ -doped CdSe QDs – one of the most important diluted magnetic semiconductors – is considered almost impossible, although  $\text{Mn}^{2+}$  ions can be incorporated into bulk CdSe at a very high doping concentration of 50%. It is generally believed that impurities can be easily removed from nanocrystals during synthesis due to thermodynamic reasons.<sup>[19a][7]</sup> In this respect, doping of nanoclusters is very challenging. In the following sections, previous studies on the nanocrystal doping are reviewed, and the limitations observed for doping ultra-small sized nanoclusters are discussed.

### 1.4.2.2 Remote Doping by External Charge Carriers

Because of the difficulties observed during the incorporation of impurity atoms into host nanocrystals, initial studies of doped semiconductor nanocrystals were conducted by using an electron transfer approach (so-called “remote doping”). The external charge carriers were transferred to semiconductor nanocrystals. The first successful demonstration of this concept showed that CdSe nanocrystals can exhibit n-type characteristics by adding sodium biphenyl species.<sup>[6a]</sup> As a result, electrons were transferred from the Na biphenyl molecules to the  $1S_e$  electronic energy state of CdSe nanocrystals (see Fig. 1.13a). The injected electrons can be characterized by infrared spectroscopy, because they can be excited to higher energy states of the obtained QDs.

Similarly, the same group reported that the carrier density of QDs can be controlled *via* electrochemistry.<sup>[6b]</sup> The conductivity of the thin films containing n-type CdSe QDs was significantly increased by potassium (K) doping or electrochemical charge injection. The described electrochemical doping method was successfully extended to PbSe QDs.<sup>[6c]</sup> Because of the small energy difference between the hole and electron states of PbSe QDs (around 0.28 eV), the injection of both holes and electrons was possible (it eventually resulted in n-type and p-type ambipolar characteristics).

Using the described “remote doping” approach, a thin film field-effect transistor was fabricated.<sup>[6d]</sup> In this study, PbSe QD film was treated by hydrazine, which passivated its surface by acting not only as a linker reducing interparticle distances, but also as a dopant producing n-type characteristics through electron donations (Fig. 1.13b). When hydrazine is desorbed from the QD film surface, it starts exhibiting p-type characteristics. Despite the realization of the field-effect transistor, the “remote doping” can be only maintained for a short period (less than several hours). Therefore, the incorporation of impurity ions into semiconductor nanocrystals is highly required.

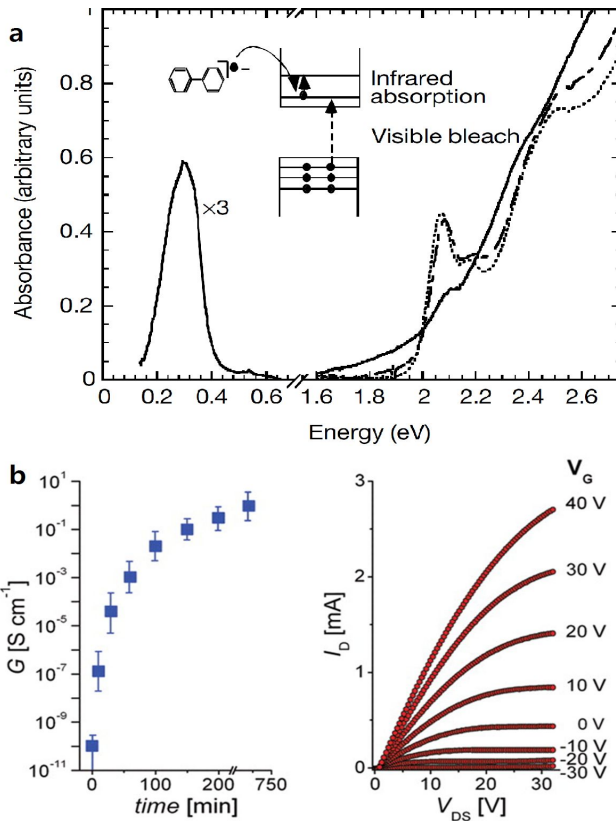


**Figure 1.13** (a) Infrared spectra of CdSe nanocrystals recorded before (dotted line), immediately after (solid line), and 27 h after (dashed line) the addition of sodium biphenyl species. The scheme of n-type doping of CdSe nanocrystals is also shown. (b) Conductivity and gate-voltage response of PbSe nanocrystal thin films after hydrazine treatment. Panel a is reproduced with permission from Ref. [6a], Nature Publishing Group. Panel b is reproduced with permission from Ref. [6d], American Association for the Advancement of Science.

### 1.4.2.3 Growth-Controlled Doping

Significant efforts have been spent to achieve direct incorporation of impurities into host semiconductor nanocrystals. One conventional approach consists of introducing impurity atoms during nanocrystal growth. One of the most representative examples was demonstrated during the synthesis of ZnSe:Mn<sup>2+</sup> nanocrystals by Norris and his coworkers.<sup>[17b]</sup> The obtained ZnSe:Mn<sup>2+</sup> nanocrystals exhibited the high quantum efficiency of 22%, which could not be reached by their bulk counterparts. In addition, they demonstrated a giant Zeeman splitting of 28 meV, corresponding to the value of  $g_{eff}$  of around 475.

Despite the demonstrated success, the utilization of this approach for other II–VI semiconductors was very challenging. In the following studies, Norris and coworkers suggested a mechanism based on the surface adsorption kinetics (Fig. 1.14).<sup>[7a,c,e]</sup> Doping is achieved by binding the impurity ions to the surface of nanocrystals during their growth. In solution, impurity ions usually exist as impurity-surfactant complexes, which should be subsequently dissociated in order to realize surface adsorption (Fig. 1.14b). Thus, the binding strength of the impurity ions to the nanocrystal surface ( $E_{Mn-Surface}^B$ ) should be high enough, exceeding that for the surface ligands to impurity ions ( $E_{Mn-Surfactant}^B$ ) (Fig. 1.14c). This theory can explain the reason why doping of

wurtzite-CdSe is more challenging than zinc-blende ZnSe.  $Mn^{2+}$  ions have very high values of the binding affinity to the surface of zinc-blende (110) facets, making the process of doping zinc-blende nanocrystals relatively easy. It has been successfully applied to  $Mn^{2+}$  doping of zinc blende and wurtzite CdSe nanocrystals by careful selection of surface ligands molecules, using weakly binding hexadecylamine instead of strongly binding trioctylphosphine oxide or trioctylphosphine.

The described method requires delicate synthetic conditions, which limit the scope of reaction parameters. In addition, the growth process is required for the incorporation of impurity ions. Therefore, this technique is difficult to apply to the nanostructures with extremely small sizes, such as nanoclusters.

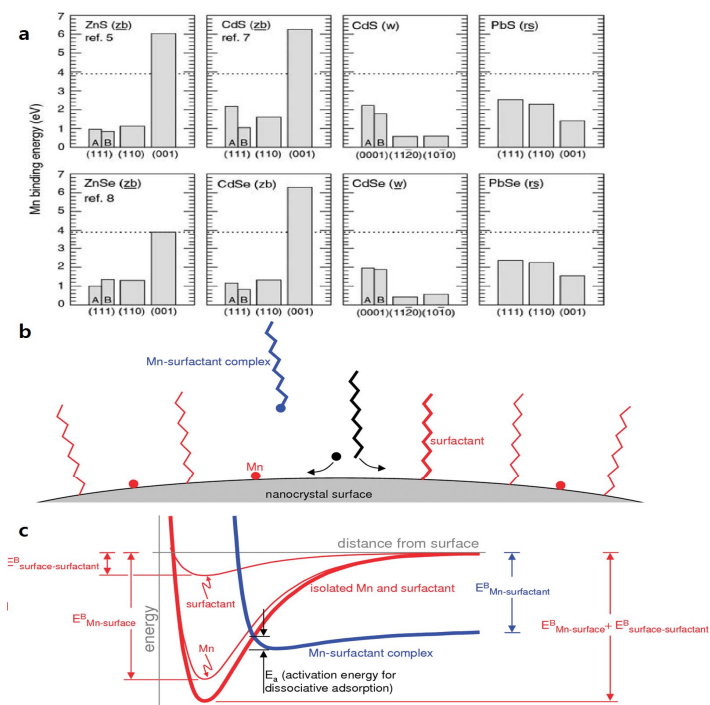


**Figure 1.14** (a) Binding energies of  $\text{Mn}^{2+}$  ions to various semiconductors with different crystal structures (zinc blende (zb), wurtzite (w), and rock-salt (rs) ones). The binding energy of the bulk Mn crystal is plotted as the dotted line. (b) A schematic describing the adsorption of impurities on the nanocrystal surface. (c) A potential energy diagram showing the potential energy of a Mn-surfactant complex (blue) and the total potential energy of a Mn atom and a surfactant molecule bonded to the nanocrystal surface. Panel a is reproduced with permission from Ref. [7a], Nature Publishing Group. Panels b and c are reproduced with permission from Ref. [7e], American Chemical Society.

#### 1.4.2.4 Doping by Diffusion

Because doping during the growth stage requires delicate control of synthetic chemistry, an alternative facile approach was proposed. Instead of the impurity incorporation during nanocrystal growth, the diffusion of impurity ions to the as-synthesized nanocrystals was realized.

A typical example of this approach is shown in Fig. 1.15. MnSe nanocrystals were initially prepared to synthesize MnSe/ZnSe core/shell nanostructures, and the diffusion of  $\text{Mn}^{2+}$  ions from the core to the shell was intentionally induced at high temperature conditions (alternatively, ZnSe/MnSe/ZnSe nanocrystals could be used instead of the MnSe/ZnSe ones). Interestingly,  $\text{Mn}^{2+}$  ions can be incorporated into nanocrystals either with tetrahedral or non-tetrahedral geometry depending on the reaction conditions.<sup>[20]</sup> Recently, this method has been further applied for the synthesis of  $\text{Mn}^{2+}$ -doped CdSe without the formation of heterostructures containing the MnSe phase. It has been demonstrated that the diffusion doping of the as-synthesized nanocrystals with various shapes in solution is possible for  $\text{Mn}^{2+}$  ions (Figs. 1.23b-d).<sup>[20e]</sup>

In order to achieve the effective diffusion of impurities into the host material, this method usually requires high-temperature conditions. In this condition, nanoclusters cannot be stabilized and further grow into larger nanocrystals.

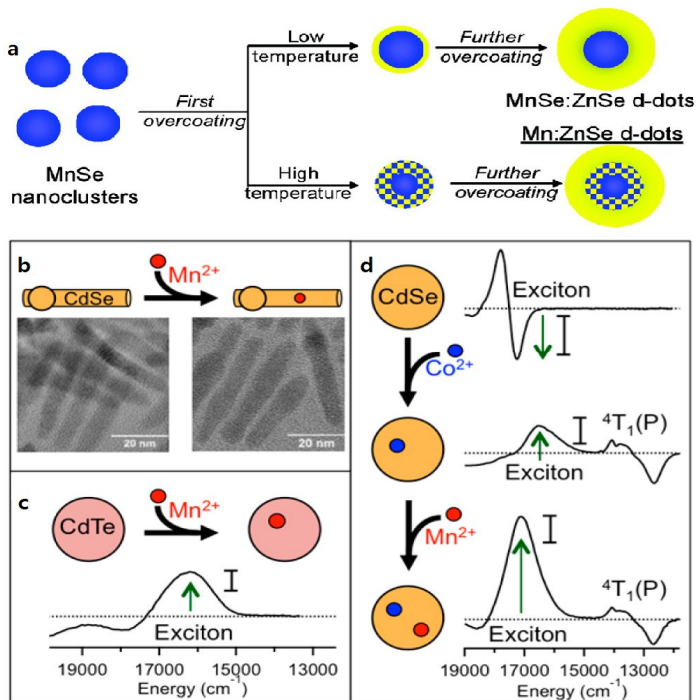


**Figure 1.15** (a) A schematic illustration describing the mechanism of formation of Mn<sup>2+</sup>-doped ZnSe species from MnSe/ZnSe. (b) TEM images showing the wz-CdSe nanorods before and after diffusion doping with Mn<sup>2+</sup> at 300 °C. (c) Magnetic circular dichroism (MCD) spectrum of CdTe nanocrystals obtained after diffusion doping with Mn<sup>2+</sup> ions. (d) A co-doping process of subsequent diffusion doping of zb-CdSe nanocrystals with Co<sup>2+</sup> and Mn<sup>2+</sup> ions. The corresponding MCD spectra are displayed. Panel a is reproduced with permission from Ref. [20b], American Chemical Society. Panels b-d are reproduced with permission from Ref. [20e], American Chemical Society.

#### 1.4.2.5 Doping by a Cation Exchange Reaction

Another representative doping method involves using a cationic exchange reaction. During this reaction, cations in the as-synthesized nanocrystals are replaced by external heteroatoms. The first successful demonstration of the cation exchange reaction in semiconductor nanocrystals was performed by the Alivisatos group.<sup>[21a]</sup> In this study, preformed CdSe nanocrystals with various shapes (including dots, rods, and tetrapods) were converted to Ag<sub>2</sub>Se nanocrystals with similar shapes. Furthermore, this reaction was found to be reversible. In the subsequent study, the same group showed that partial cation exchange could be possible instead of the complete material conversion.<sup>[21b]</sup> The original CdS nanorods were transformed into CdS-Ag<sub>2</sub>S superlattice nanorods, suggesting the possibility of nanocrystal doping via a cation exchange reaction if the degree of cation exchange was controllable.

The first successful attempt of doping *via* cation exchange was demonstrated by the Banin group.<sup>[6e]</sup> Heavily doped InAs nanocrystals exhibit *n*-type or *p*-type characteristics depending on the choice of dopant ions. In the following study conducted by the Norris group, electronic impurity doping was achieved at much lower concentrations.<sup>[6f]</sup> As a result, Ag-doped CdSe nanocrystals were obtained from the as-synthesized CdSe nanocrystals. Between 1 and 13 Cd atoms of each CdSe nanocrystal were replaced with Ag atoms.

Interestingly, the Ag impurities can act as both n-type (interstitial, <10 atoms per nanocrystal) and p-type (substitutional, >10 atoms per nanocrystal) dopants depending on the concentration, thus affecting the properties (*e.g.*, quantum yield) (Fig. 1.16).

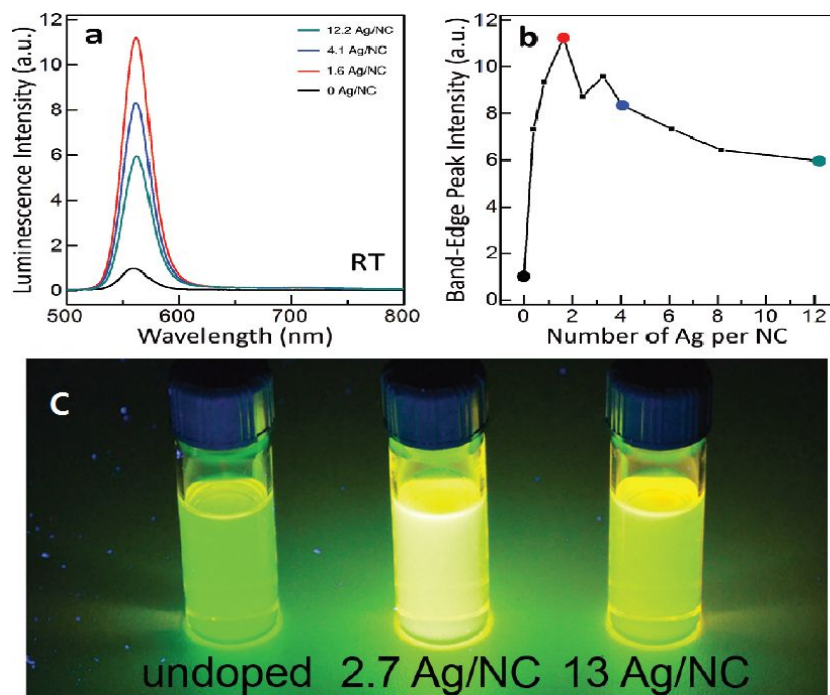


**Figure 1.16** (a) Photoluminescence spectra, (b) relative intensity of the band-edge emission, and (c) photographs of CdSe nanocrystals with different average numbers of Ag ions in a nanocrystal. The figure is reproduced with permission from Ref. [6f], American Chemical Society.

## 1.5 Dissertation Overview

For both fundamental scientific studies and various practical applications, the designed synthesis of multi-element-containing nanomaterials is of key importance. However, the previous works on I–III–VI semiconductor nanocrystals and doped II–VI nanoclusters is still in its initial stage. In this thesis, the synthesis and characterization of ternary selenide semiconductor quantum nanostructures have been performed. The resulting dissertation consists of three parts.

In the first part (Chapter 2), Cu–In–Se QDs, one of the most representative I–III–VI semiconductor nanocrystals, are synthesized via colloidal chemical routes, and their size-dependent properties are investigated. By varying the QD size from 2 nm to 10 nm, their band alignment can be finely optimized for effective light absorption and injection of electrons from the QDs into TiO<sub>2</sub>. The resulting photovoltaic characteristics are significantly affected by the QD size, and the best cells yields conversion efficiency value of 4.30% at a particle size of 4 nm.

The second part (Chapter 3) describes the surface engineering of Cu–In–Se QD–TiO<sub>2</sub> photoelectrodes and the related photovoltaic characteristics of Cu–In–Se QDs. It is found that the charge carrier recombination process can

be effectively suppressed by controlling the thickness of ZnS overlayers on the QD-sensitized photoanodes, resulting in the remarkable conversion efficiency of 8.10% under one sun illumination. Interfacial electron recombination with the electrolyte and non-radiative recombination associated with QDs are significantly reduced by introducing the thick ZnS overlayer, explaining the enhancement in photovoltaic performance.

In the third part (Chapter 4), an alternative doping method (doping of magic-sized clusters) is proposed. The reaction conducted at room temperature results in the formation of  $\text{Mn}^{2+}$ -doped CdSe clusters. The results of the mass spectroscopy analysis reveal that one or two  $\text{Cd}^{2+}$  ions in a  $(\text{CdSe})_{13}$  cluster can be replaced with  $\text{Mn}^{2+}$  ions. Interestingly, such clusters exhibit a semiconductor band structure and display the characteristics of diluted magnetic semiconductors. The clusters show multiple excitonic transitions with different magneto-optical activities, which are related to the fine structure effect. A giant magneto-optical response is observed, corresponding to the effective g-factor of  $81(\pm 8)$  at 4 K.

\*\*Parts of this chapter (section 1.4.1) were published in the article, “Nonclassical Nucleation and Growth of Inorganic Nanoparticles.” (*Nature Reviews Materials* **2016**, *1*, 16034).

## 1.6 References

- [1] (a) Murray, C. B.; Norris, D. J.; Bawendi, M. G. *J. Am. Chem. Soc.* **1993**, *115*, 8706. (b) A. P. Alivisatos *Science* **1996**, *271*, 933. (c) Goesmann, H.; Feldmann, C. *Angew. Chem. Int. Ed.* **2010**, *49*, 1362.
- [2] (a) Peng, X. G.; Manna, L.; Yang, W.; Wickham, J.; Scher, E.; Kadavanich, A.; Alivisatos, A. P. *Nature* **2000**, *404*, 59. (b) Manna, L.; Milliron, D. J.; Meisel, A.; Scher, E. C.; Alivisatos, A. P. *Nat. Mater.* **2003**, *2*, 382. (c) Joo, J.; Son, J. S.; Kwon, S. G.; Yu, J. H.; Hyeon, T. *J. Am. Chem. Soc.* **2006**, *128*, 5632. (d) Ithurria, S.; Tessier, M. D.; Mahler, B.; Lobo, R. P. S. M.; Dubertret, B.; Efros, A. L. *Nat. Mater.* **2011**, *10*, 936.
- [3] (a) Wang, C., Xu, C., Zeng, H. & Sun, S. *Adv. Mater.* **2009**, *21*, 3045. (b) Buck, M. R. & Schaak, R. E. *Angew. Chem. Int. Ed.* **2013**, *52*, 6154. (c) Strasser, P.; Koh, S.; Anniyev, T.; Greeley, J.; More, K.; Yu, C.; Liu, Z.; Kaya, S.; Nordlund, D.; Ogasawara, H.; Toney, M. F.; Nilsson, A. *Nature Chem.* **2010**, *2*, 454. (d) Buck, M. R.; Bondi, J. F.; Schaak, R. E. *Nature Chem.* **2012**, *4*, 37.
- [4] (a) Guo, Q.; Kim, S. J.; Kar, M.; Shafarman, W. N.; Birkmire, R. W.; Stach, E. A.; Agrawal, R.; Hillhouse, H. W. *Nano Lett.* **2008**, *8*, 2982. (b) Panthani, M. G.; Akhavan, V.; Goodfellow, B.; Schmidtke, J. P.; Dunn, L.; Dodabalapur, A.; Barbara, P. F.; Korgel, B. A. *J. Am. Chem. Soc.* **2008**, *130*, 16770. (c) Allen, P.

M.; Bawendi, M. G. *J. Am. Chem. Soc.* **2008**, *130*, 9240. (d) Cassette, E.; Pons, T.; Bouet, C.; Helle, M.; Bezdetsnaya, L.; Marchal, F.; Dubertret, B. *Chem. Mater.* **2010**, *22*, 6117. (e) Zhong, H. Z.; Wang, Z. B.; Bovero, E.; Lu, Z. H.; Van Veggel, F. C. J. M.; Scholes, G. D. *J. Phys. Chem. C* **2011**, *115*, 12396. (f) Panthani, M. G.; Khan, T. A.; Reid, D. K.; Hellebusch, D. J.; Rasch, M. R.; Maynard, J. A.; Korgel, B. A. *Nano Lett.* **2013**, *13*, 4294. (g) Panthani, M. G.; Stolle, C. J.; Reid, D. K.; Rhee, D. J.; Harvey, T. B.; Akhavan, V. A.; Yu, Y. X.; Korgel, B. A. *J. Phys. Chem. Lett.* **2013**, *4*, 2030.

[5] (a) Chang, C. H.; Davydov, A.; Stanbery B. J.; Anderson, T. J. *Proceedings of the Conference Record of the 25th IEEE Photovoltaic Specialists Conference 1996*, May 13-17, Washington DC, 849. (b) Nelson, *The Physics of Solar Cells*, Imperial College Press, London, **2003**, Ch. 8. (c) Jackson, P.; Hariskos, D.; Lotter, E.; Paetel, S.; Wuerz, R.; Menner, R.; Wischmann, W.; M. Powalla, *Prog. Photovoltaics: Res. Appl.* **2011**, *19*, 894. (d) Paszkowicz, W.; Lewandowska, R.; Bacewicz, R. *J. Alloys & Compounds* **2004**, *362*, 241. (e) Ghorbani, E.; Kiss, J.; Mirhosseini, H.; Roma, G.; Schmidt, M.; Windeln, J.; Kühne, T. D.; Felse, C. *J. Phys. Chem. C* **2015**, *119*, 25197. (f) Jackson, P.; Hariskos, D.; Wuerz, R.; Kiowski, O.; Bauer, A.; Friedlmeier, T. M.; Powalla, M. *Phys. Status Solidi RRL*, **2015**, *9*, 28. (g) <http://www.solarserver.com/solar-magazine/solar-energy-system-of-the-month/photovoltaic-production-in-the-cigsfab-integrated->

[factories-provide-competitive-solar-electricity.html](#) (accessed May-27th, 2016.)

[6] (a) Shim, M.; Guyot-Sionnest, P. *Nature* **2000**, *407*, 981. (b) Yu, D.; Wang, C.; Guyot-Sionnest, P. *Science* **2003**, *300*, 1277. (c) Wehrenberg, B. L.; Guyot-Sionnest, P. *J. Am. Chem. Soc.* **2003**, *125*, 7806. (d) Talapin, D. V.; Murray, C. B. *Science* **2005**, *310*, 86. (e) Mocatta, D.; Cohen, G.; Schattner, J.; Millo, O.; Rabani, E.; Banin, U. *Science* **2011**, *332*, 77. (f) Sahu, A.; Kang, M. S.; Kompch, A.; Notthof, C.; Wills, A. W.; Deng, D.; Winterer, M.; Frisbie, C. D.; Norris, D. J. *Nano Lett.* **2012**, *12*, 2587.

[7] (a) Erwin, S. C.; Zu, L.; Haftel, M. I.; Efros, Al. L.; Kennedy, T. A.; Norris, D. J. *Nature* **2005**, *436*, 91. (b) Bryan, J. D.; Gamelin, D. R. *Prog. Inorg. Chem.* **2005**, *54*, 47. (c) Norris, D. J.; Efros, Al. L.; Erwin, S. C. *Science* **2008**, *319*, 1776. (d) Santangelo, S. A.; Hinds, E. A.; Vlaskin, V. A.; Archer, P. I.; Gamelin, D. R. *J. Am. Chem. Soc.* **2007**, *129*, 3973. (e) Du, M.-H.; Erwin, S. C.; Efros, A. L. *Nano Lett.* **2008**, *8*, 2878. (f) Buonsanti, R.; Milliron, D. J. *Chem. Mater.* **2013**, *25*, 1305.

[8] (a) Sugimoto, T. *J. Colloid Interface Sci.* **2007**, *309*, 106. (b) Park, J.; Joo, J.; Kwon, S. G.; Jang, Y.; Hyeon, T. *Angew. Chem. Int. Ed.* **2007**, *46*, 4630. (c) Kwon, S. G.; Hyeon, T. *Small* **2012**, *7*, 2685. (d) Klabunde, K. J. *Nanoscale Materials in Chemistry*, 2nd ed., Wiley-Interscience, New York **2009**. (e) Thanh, N. T. K.; Maclean, N.; Mahiddine, S. *Chem. Rev.* **2014**, *114*, 7610.

[9] (a) LaMer, V. K.; Dinigar, R. H. *J. Am. Chem. Soc.* **1950**, *72*, 4847. (b)

LaMer, V. K.; *Ind. Eng. Chem.* **1952**, *44*, 1270. (c) Sugimoto, T. *Adv. Colloid Interfac. Sci.* **1987**, *28*, 65. (d) Mullin, J. W. *Crystallization*, 4th ed., Butterworth-Heinemann, Oxford **2001**. (e) Sugimoto, T. *Monodispersed Particles*, Elsevier, New York **2001**.

[10] (a) Peng, X.; Wickham, J.; Alivisatos, A. P. *J. Am. Chem. Soc.* **1998**, *120*, 5343. (b) Chen, Y.; Johnson, E.; Peng, X. *J. Am. Chem. Soc.* **2007**, *129*, 10937.

[11] (a) Sax, N. I. *Dangerous Properties of Industrial Materials Report*, Reinhold, New York **1995**. (b) Chiesi, A.; Grossoni, G.; Nardelli, M.; Vidoni, M. *E. Journal of the Chemical Society D: Chemical Communications* **1969**:404b–405.

[12] (a) Schmid, G.; *Chem. Rev.* **1992**, *92*, 1709. (b) Gatteschi, D.; Caneschi, A.; Pardi, L.; Sessoli, R. *Science* **1994**, *265*, 1054. (c) Soloviev, V. N.; Eichhöfer, A.; Fenske, D.; Banin, U. *J. Am. Chem. Soc.* **2001**, *123*, 2354. (d) Martin, T. P. *Phys. Rep.* **1996**, *273*, 199. (e) Marks, L. D. *Rep. Prog. Phys.* **1994**, *57*, 603. (f) Baletto, F.; Ferrando, R. *Rev. Mod. Phys.* **2005**, *77*, 371. (g) Schmid, G. *Chem. Soc. Rev.* **2008**, *37*, 1909.

[13] (a) Negishi, Y.; Nakazaki, T.; Malola, S.; Takano, S.; Niihori, Y.; Kurashige, W.; Yamazoe, S.; Tsukuda, T.; Häkkinen, H. *J. Am. Chem. Soc.* **2015**, *137*, 1206. (b) Cha, S. H.; Kim, J. U.; Kim, K. H.; Lee, J. C. *Chem. Mater.* **2007**, *19*, 6297. (c) Devadas, M. S.; Kim, J.; Sinn, E.; Lee, D.; GoodsonIII, T.; Ramakrishna, G. *J.*

*Phys. Chem. Lett.* **2011**, *2*, 2752. (d) Tian, S.; Li, Y.-Z.; Li, M.-B.; Yuan, J.; Yang, J.; Wu, Z.; Jin, R. *Nature Commun.* **2015**, *6*, 8667. (e) Parker, J. F.; Fields-Zinna, C. A.; Murray, R. W. *Acc. Chem. Res.* **2010**, *43*, 1289.

[14] (a) Soloviev, V. N.; Eichhöfer, A.; Fenske, D.; Banin, U. *J. Am. Chem. Soc.* **2000**, *122*, 2673. (b) Beecher, A. N.; Yang, X.; Palmer, J. H.; LaGrassa, A. L.; Juhas, P.; Billinge, S. J. L.; Owen, J. S. *J. Am. Chem. Soc.* **2014**, *136*, 10645. (c) Kasuya, A.; Sivamohan, R.; Barnakov, Y. A.; Dmitruk, I. M.; Nirasawa T.; Romanyuk, V. R.; Kumar, V.; Mamykin, S. V.; Tohji, K.; Jeyadevan, B.; Shinoda, K.; Kudo, T.; Terasaki, O.; Liu, Z.; Belosludov, R. V.; Sundararajan, V.; Kawazoe, Y. *Nature Mater.* **2004**, *3*, 99. (d) Jasieniak, J.; Smith, L.; Embden, J. v.; Mulvaney, P.; Califano, M. *J. Phys. Chem. C* **2009**, *113*, 19468.

[15] (a) Sadeghi, O.; Zakharov, L. N.; Nyman, M. *Science* **2015**, *347*, 1359. (b) Liu, T.; Diemann, E.; Li, H.; Dress, A. W. M.; Müller, A. *Nature* **2003**, *426*, 59. (c) Long, D.-L.; Tsunashima, R.; Cronin, L. *Angew. Chem. Int. Ed.* **2010**, *49*, 1736. (d) Keggin, J. F. *Nature* **1933**, *131*, 908. (e) Dawson, B. *Acta Cryst.* **1953**, *6*, 113. (f) Anderson, J. S. *Nature* **1937**, *140*, 850.

[16] (a) Lu, Y.; Chen, W. *Chem. Soc. Rev.* **2012**, *41*, 3594. (b) Kudera, S.; Zanella, M.; Giannini, C.; Rizzo, A.; Li, Y.; Gigli, G.; Cingolani, R.; Ciccarella, G.; Spahl, W.; Parak, W. J.; Manna, L. *Adv. Mater.* **2007**, *19*, 548. (c) Evans, C. M.; Guo, L.; Peterson, J. J.; Maccagnano-Zacher, S.; Krauss, T. D. *Nano Lett.* **2008**, *8*,

2896. (d) Yu, J. H.; Liu, X.; Kweon, K. E.; Joo, J.; Park, J.; Ko, K. T.; Lee, D. W.; Shen, S.; Tivakornsasithorn, K.; Son, J. S.; Park, J. H.; Kim, Y. W.; Hwang, G. S.; Dobrowolska, M.; Furdyna, J. K.; Hyeon, T. *Nat. Mater.* **2010**, *9*, 47. (e) Kim, B. H.; Shin, K.; Kwon, S. G.; Jang, Y.; Lee, H.-S.; Lee, H.; Jun, S. W.; Lee, J.; Han, S. Y.; Yim, Y.-H.; Kim, D.-H.; Hyeon T. *J. Am. Chem. Soc.* **2013**, *135*, 2407. (f) Gebauer, D.; Völkel, A.; Cölfen, H. *Science* **2008**, *322*, 1819.

[17] (a) Mikulec, F. V.; Kuno, M.; Bennati, M.; Hall, D. A.; Griffin, R. G.; Bawendi, M. G. *J. Am. Chem. Soc.* **2000**, *122*, 2532. (b) Norris, D. J.; Yao, N.; Charnock, F. T.; Kennedy, T. A. *Nano Lett.* **2001**, *1*, 3. (c) Pradhan, N.; Goorskey, D.; Thessing, J.; Peng, X. *J. Am. Chem. Soc.* **2005**, *127*, 17586. (d) Wang, F.; Han, Y.; Lim, C. S.; Lu, Y.; Wang, J.; Xu, J.; Chen, H.; Zhang, C.; Hong, M.; Liu, X. *Nature* **2010**, *463*, 1061. (f) Whitham, P. J.; Knowles, K. E.; Reid, P. J.; Gamelin, D. R. *Nano Lett.* **2015**, *15*, 4045.

[18] (a) Beaulac, R.; Schneider, L.; Archer, P. I.; Bacher, G.; Gamelin, D. R. *Science* **2009**, *325*, 973. (b) Bussian, D. A.; Crooker, S. A.; Yin, M.; Brynda, M.; Efros, Al. L.; Klimov, V. I. *Nat. Mater.* **2009**, *8*, 35. (c) Fainblat, R.; Frohleiks, J.; Muckel, F.; Yu, J. H.; Yang, J.; Hyeon, T.; Bacher, G. *Nano Lett.* **2012**, *12*, 5311. (d) Ochsenein, S. T.; Feng, Y.; Whitaker, K. M.; Badaeva, E.; Liu, W. K.; Li, X.; Gamelin, D. R. *Nat. Nanotech.* **2009**, *4*, 681. (e) Awschalom, D. D.; Flatté, M. E. *Nat. Phys.* **2007**, *3*, 153. (f) Pandey, A.; Brovelli, S.; Viswanatha,

- R.; Li, L.; Pietryga, J. M.; Klimov, V. I.; Crooker S. A. *Nat. Nanotech.* **2012**, *7*, 792.
- [19] (a) Dalpian, G. M.; Chelikowsky, J. R. *Phys. Rev. Lett.* **2006**, *96*, 226802.
- [20] (a) Pradhan, N.; Goorskey, D.; Thessing, J.; Peng, X. *J. Am. Chem. Soc.* **2005**, *127*, 17586. (b) Pradhan, N.; Peng, X. *J. Am. Chem. Soc.* **2007**, *129*, 3339. (c) Yang, Y.; Chen, O.; Angerhofer, A.; Cao, Y. C. *J. Am. Chem. Soc.* **2006**, *128*, 12428. (d) Yang, Y.; Chen, O.; Angerhofer, A.; Cao, Y. C. *J. Am. Chem. Soc.* **2008**, *130*, 15649. (e) Vlaskin, V. A.; Barrows, C. J.; Erickson, C. S.; Gamelin, D. R. *J. Am. Chem. Soc.* **2013**, *135*, 14380.
- [21] (a) Son, D. H.; Hughes, S. M.; Yin, Y.; Alivisatos, A. P. *Science* **2004**, *306*, 1009. (b) Robinson, R. D.; Sadtler, B.; Demchnko, D. O.; Erdonmez, C. K.; Yang, L.-W.; Alivisatos, A. P. *Science* **2007**, *317*, 355.

# **Chapter 2. Synthesis and Size-Dependent Photovoltaic Characterization of Copper–Indium–Selenide Quantum Dots**

## **2.1 Introduction**

Over the last two decades, tremendous progress has been made in the synthesis of colloidal quantum dots (QDs)<sup>[1]</sup> and in their applications to next-generation photovoltaic (PV) devices.<sup>[2]</sup> Colloidal QDs can be easily solution-processed into a thin film by low-cost fabrication techniques.<sup>[3]</sup> Furthermore, the unique properties of QDs, such as band energy tunability, slow hot electron cooling, and multiple exciton generation effect, suggest the possibility of achieving energy conversion efficiencies exceeding the Shockley-Queisser limit.<sup>[4]</sup> Despite of promising performance of QD solar cells, there are growing concerns about the use of QDs in electronic devices<sup>[5]</sup> regarding the health and environmental issues.<sup>[6]</sup> Most of QDs employed in electronic devices contain toxic heavy-metals such as cadmium or lead. Consequently, development of efficient and heavy-metal-free QD solar cells is critical for their extensive commercial applications, especially for household

appliances. For instance, the European Union's restriction of Hazardous Substances Directive limits the use of the materials composed of heavy-metals in consumer electronic devices.

Copper-indium-selenide (CISe) nanocrystals (NCs) are promising alternatives for applications in QD solar cells because of low toxicity,<sup>[7]</sup> a narrow direct band gap of 1.04 eV, and a high absorption coefficient exceeding  $3 \times 10^4 \text{ cm}^{-1}$  at wavelengths below 1000 nm, which is suitable for the utilization of full solar spectrum. Although there are several reports on the synthesis of CISe NCs<sup>[8]</sup> and their applications to solar cells,<sup>[9]</sup> the tuning of quantum-size-effect of CISe NCs for their applications in PV devices has rarely been studied. Very recently, Korgel and coworkers reported heterojunction solar cells employing CISe QDs with a cadmium sulfide (CdS) layer, exhibiting a low conversion efficiency of  $\sim 1\%$ .<sup>[9g]</sup> In the most of previous studies, the CISe NCs larger than the Bohr diameter were used,<sup>[9a-c]</sup> or NCs were applied in conjunction with sintering processes.<sup>[9d-f]</sup> This high temperature sintering process is very complicated and expensive for CISe, and often leads to the loss of quantum-confinement.<sup>[9d-f,10]</sup> Another chalcopyrite-structured compound, copper-indium-sulfide (CIS), have been employed in QD-sensitized solar cells (QDSCs).<sup>[11]</sup> However, these cells could not absorb light in the near infrared (NIR) region effectively because of the relatively

large band gap of CIS. Furthermore, these CISE and CIS based solar cells required n-type CdS layer, which eliminates the advantage of low toxicity of CISE. In addition, many portion of photocurrent is actually generated by CdS part in these QDSCs.

This chapter presents a new synthetic process to produce NIR-absorbing CISE QDs and their applications to completely heavy-metal-free QDSCs. To the best of our knowledge, these QD solar cells have not been demonstrated previously, mainly because of the difficulty in controlling the energetics of CISE for the effective electron injection into the TiO<sub>2</sub> conduction band (CB). Our facile and scalable method allowed control over the sizes and compositions of the QDs, which are critical parameters for tuning the optoelectronic properties of CISE QDs. The effect of quantum-confinement on the optical and electronic properties of CISE QDs and the resulting PV performances were systematically investigated. Fine quantum-tuning of band alignment in the NIR CISE QDs resulted in highly efficient QDSCs that are free from toxic heavy-metal compounds. At the optimal QD size of ~4 nm, the CISE QDSC exhibited a remarkable conversion efficiency of ~4.30%.

## 2.2 Experimental Section

### 2.2.1 Synthesis of Cu–In–Se Colloidal QDs

The synthesis of CISE ternary QDs was carried out using standard Schlenk techniques under argon (Ar) atmosphere. Oleylammonium selenocarbamate<sup>[12a]</sup> was prepared by bubbling carbon monoxide (CO) gas into 10 mL of oleylamine (Across, approximate C18-content 80–90%) containing selenium powder (0.395 g, 5.0 mmol, Aldrich, 99.99%) under vigorous stirring at 120 °C until the solution became almost transparent. In a typical synthesis, 0.5 mmol of copper (I) iodide (0.095 g, Alfa Aesar, 99.998%), 0.5 mmol of indium (III) iodide (0.248 g, Alfa Aesar, 99.999%), and 15 mL of oleylamine were mixed in a glove box. The reaction mixture was degassed under vacuum for 30 minutes at 120 °C, and then purged with Ar. This solution was then cooled to 70 °C under an Ar atmosphere, and 1.0 mmol of the as-prepared oleylammonium selenocarbamate solution was injected into the solution. The resulting black colloidal solution was heated to 210 °C, and was further aged at that temperature for 20 minutes. The product was precipitated by adding excess ethanol containing trioctylphosphine (Aldrich, 97%), which was required to remove the unreacted selenium precursor. For further characterization and application, the

powder was re-dispersed in dichloromethane or dried to powder. For the synthesis of CISE QDs with different sizes, the aging temperature was varied in the range of 80–270 °C.

### **2.2.2 Characterization of Cu–In–Se Colloidal QDs**

Transmission electron microscopy (TEM) images and scanning TEM images were obtained using a JEOL EM-2010 EX II microscope and JEOL 2100F microscope, respectively. For accuracy, STEM images were used for measuring the size of the smallest QDs. X-ray diffraction (XRD) patterns were obtained with a Rigaku D/Max-3C diffractometer equipped with rotation anode and a Cu K $\alpha$  radiation source ( $\lambda = 0.15418$  nm). The lattice constants were calculated by fitting the XRD patterns to Pearson-VII functions. Inductively coupled plasma-atomic emission spectrometry (ICP-AES) for quantitative and composition analysis was performed on a Shimadzu ICPS-7500. The optical absorption spectra were obtained using CARY 5000E UV-VIS-NIR spectrophotometer. The overall reaction yield was determined by thermogravimetric analysis (TGA) and ICP-AES. To examine the conduction band minimum (CBM) of QDs, cyclic voltammetry (CV) analysis was performed using an electrochemical analyzer (CH Instruments Inc., Austin, TX). A glassy carbon electrode was used as a

working electrode, on which QDs in dichloromethane (concentration  $\sim 5 \text{ mg mL}^{-1}$ ) were drop-casted. Platinum wire and Ag/Ag<sup>+</sup> electrode were used as a counter and reference electrode, respectively. The electrolyte was 0.1 M tetra-n-butylammonium perchlorate (TBAP) in acetonitrile. Before every measurement, the electrolyte was deaerated by nitrogen bubbling for 30 min. The potential range was from 1.2 to  $-1.0 \text{ V}$  versus Ag/Ag<sup>+</sup> with a scan rate of  $50 \text{ mV s}^{-1}$ . The measured potential was calibrated and converted to the values versus a normal hydrogen electrode (NHE) by using the Fc/Fc<sup>+</sup> couple. The CBM was determined from the first reduction peak potential in the CV.<sup>[12b]</sup> The valence band maximum was estimated from the CBM and optical band gap. Exciton binding energy was ignored because it is usually smaller than the precision of CV measurement.<sup>[12c]</sup>

### **2.2.3 Preparation of QD-sensitized working electrodes**

A transparent TiO<sub>2</sub> paste containing nanocrystalline TiO<sub>2</sub> particles with a diameter of 20 nm was prepared as described in the previous report.<sup>[12d]</sup> Briefly, nanocrystalline TiO<sub>2</sub> particles were synthesized by a hydrothermal method, followed by mixing with ethyl cellulose (Aldrich), lauric acid (Fluka) and terpineol (Fluka) The weight ratio of the constituents was as follows: TiO<sub>2</sub>/ethyl cellulose/lauric acid/terpineol = 0.18:0.05:0.02:0.75. A scattering

paste was prepared using TiO<sub>2</sub> particles with size of 500 nm (G2, Showa Denko, Japan). The prepared transparent TiO<sub>2</sub> paste was deposited on fluorine doped tin oxide (FTO) glass (Pilkington, TEC-8, 8 Ω sq<sup>-1</sup>) by the doctor blade technique. Before the deposition, the FTO glass was pretreated with 7.5 wt% Ti(IV) bis(ethyl acetoacetato)-diisopropoxide solution in 1-butanol by spin casting to form a blocking layer. After drying the deposited transparent TiO<sub>2</sub> paste on a hot plate of 130 °C, the opaque TiO<sub>2</sub> paste was subsequently deposited, followed by annealing at 500 °C for 30 minutes. For the direct adsorption of QDs, the annealed TiO<sub>2</sub> electrodes were dipped into the QD dispersion in dichloromethane (99.8%, Aldrich) at room temperature. After adsorption of QDs, the prepared TiO<sub>2</sub>/QD electrodes were rinsed with dichloromethane and dried by nitrogen flow. Finally, the electrodes were passivated with ZnS layer by dipping into 0.1 M Zn(CH<sub>3</sub>COO)<sub>2</sub> (Aldrich) and 0.1 M Na<sub>2</sub>S (Aldrich) aqueous solution for 1 minute, alternately. This treatment was repeated twice, and the electrodes were rinsed with deionized (DI) water after each dipping.

#### **2.2.4 Electrode Assembly**

Cu<sub>2</sub>S counter electrode was prepared by immersing brass foils (Alfa Aesar, 0.25 mm thick) in HCl solution (DAEJUNG, 35–37 wt%) at 80 °C for 20

minutes, followed by rinsing with DI water and drying with nitrogen flow. Onto these substrates, aqueous polysulfide solution comprising of 1 M Na<sub>2</sub>S and 1 M S (99.998%, Aldrich) was dropped to form porous Cu<sub>2</sub>S film on the surface, subsequently rinsed with DI water. The TiO<sub>2</sub>/QD working electrode was assembled with the Cu<sub>2</sub>S counter electrode using hot melt Surlyn with thickness of 60 μm (Dupont 1702). Then, the aqueous polysulfide electrolyte comprising of 1 M Na<sub>2</sub>S and 1 M S was injected into the cells through two small holes pre-drilled at the working electrodes. The active area for each cell was in the range of 0.40 ± 0.03 cm<sup>2</sup>, which was confirmed by a CCD camera (Moticam 1000) and precisely measured by an image analysis program.

### **2.2.6 Photoelectrochemical Measurements**

Standard photocurrent density–voltage (*J–V*) measurements were carried out using a 1600 W Xenon lamp (Yamashita Denso YSS-200A solar simulator) equipped with an AM 1.5 G filter at one sun light intensity (100 mW cm<sup>-2</sup>). Before the measurement, each cell was covered with a black tape mask with an aperture to screen additional illumination through the lateral space.<sup>[12e]</sup> Incident photon-to-current conversion efficiency (IPCE) was measured under short circuit conditions using a 75 W Xenon lamp source

and a grating monochromator. The electrochemical impedance spectra were obtained using a Solartron 1287 potentiostat and a Solartron 1260 frequency-response detector at an open-circuit potential under AM 1.5 G one sun light illumination. The sinusoidal perturbations of 10 mV were applied at frequencies ranging from 1 Hz to 100 kHz. The same measurements were also carried out in the dark state at bias potentials ranging from  $-0.25$  to  $-0.50$  V.

### 2.2.6 Band Energy Calculations

The wave functions for CISE region, which is composed of spherical Bessel and Neumann functions, and for organic ligand region, which is composed of Hankel functions, are obtained from the following boundary conditions, where  $R(r)$  is radial eigenfunction and  $R_0$  is the QD radius.

$$dR_{n=1,\text{CISE}}(R_0) = dR_{n=1,\text{organic}}(R_0)$$

$$\left. \frac{1}{m_{\text{CISE}}^*} \frac{dR_{n=1,\text{CISE}}(r)}{dr} \right|_{r=R_0} = \left. \frac{1}{m_{\text{organic}}^*} \frac{dR_{n=1,\text{organic}}(r)}{dr} \right|_{r=R_0}$$

The effective mass of electron and hole used in this work are 0.09 and 0.76 for  $\text{CuInSe}_2$ ,<sup>[13a]</sup> and 0.16 and 1.1 for  $\text{CuIn}_3\text{Se}_5$  respectively.<sup>[13b]</sup> Effective masses of electron and hole for organic ligand are assumed as 3.03 and 0.3, respectively.<sup>[13c]</sup> Electron affinity and ionization potential are  $-4.48$  eV and  $-$

5.52 eV for  $\text{CuInSe}_2$ ,<sup>[13d]</sup> and  $-1.5$  and  $-11.8$  eV for organic ligand, respectively.<sup>[13e,f]</sup> The conduction- and valence band offsets between  $\text{CuInSe}_2$  and  $\text{CuIn}_3\text{Se}_5$  are 20 and 260 meV, respectively.<sup>[13g]</sup> Exciton Bohr radius was calculated using the same parameters.

## **2.3 Result and Discussion**

### **2.3.1 Synthesis of Cu–In–Se Quantum Dots**

CISe QDs were synthesized by the reaction between metal iodides and oleylammonium selenocarbamate in oleylamine as a coordinating solvent. Notably, oleylammonium selenocarbamate, produced by the addition of a carbonyl group to form an amide bond between selenium and oleylamine, is selected as the selenium precursor. Because of the high basicity of selenocarbamate, the Lewis acid-base reaction between the precursors is so effective that the nucleation of QDs occurred at a very low temperature. This low-temperature nucleation allow control over a wide range of growth temperatures without formation of undesired phases, which is a key factor to control the QD size. When the growth temperature is elevated from 80 °C to 270 °C, the size of the QDs increases from 2.5 nm to 10 nm and the composition changes from  $\text{CuIn}_{2.5}\text{Se}_4$  to  $\text{CuIn}_{1.1}\text{Se}_{2.1}$  simultaneously (Fig. 2.1, Table 2.1). Transmission electron microscopy (TEM) images (Fig. 2.1) of

CISe QDs show the narrow size distribution with standard deviation of 5–10% except the largest-sized ones (Fig. 2.2). This facile heat-up method using commercially available metal precursors and an inexpensive selenocarbamate is highly reproducible and allows for large-scale production, which is very important for the realization of low-cost PV devices. The high solubility of selenium through selenocarbamate formation is also beneficial for large-scale and low-cost nanocrystal synthesis. When the reaction is carried out with 13 times as much as the reagents used for the routine synthesis, as much as 1.3 g of the CISe QDs can be obtained in a single batch with a high yield of ~73%.

The X-ray diffraction (XRD) patterns of the QDs indicate that their crystal structure is identical to the tetragonal chalcopyrite structure (Fig. 2.3). The position of the main peaks match well with the values reported for the bulk chalcopyrite phase (JCPDS #40-1487). The existence of the (211) reflection specifically defines the crystal structure as the tetragonal chalcopyrite structure rather than the sphalerite structure (Fig. 2.4). However, the intensity of the (211) reflection, an indicator of the cation ordering of Cu (I) and In (III), is much lower than that shown in the single crystalline structure of bulk chalcopyrite. Consequently, the CISe QDs produced in this work can be categorized as chalcopyrite structure with ordered vacancies. It is well

known that the ordered vacancies of composition-tunable CISE dramatically affect the optoelectronic properties.<sup>[13g]</sup> Interestingly, although the compositions of the produced QDs are between those of  $\alpha$ -CuInSe<sub>2</sub> and  $\beta$ -CuIn<sub>3</sub>Se<sub>5</sub>, the lattice constant  $c$  obtained from the XRD is larger than those of  $\alpha$ -CuInSe<sub>2</sub> and  $\beta$ -CuIn<sub>3</sub>Se<sub>5</sub>, while the lattice constant  $a$  is in between them (Fig. 2.3b and Table 2.1). Consequently, the resulting tetragonal distortion ( $c/2a$  ratio) is larger than that of  $\alpha$ -CuInSe<sub>2</sub> (1.0) and  $\beta$ -CuIn<sub>3</sub>Se<sub>5</sub> (0.95) (Table 2.1),<sup>[14]</sup> which is more pronounced in the smaller QDs. The anomalous lattice expansion along the  $c$ -axis seems to be due to the disordered vacancies on the surface of the QDs, which induces a localized distortion of the lattice around the vacant sites in a manner different from that caused by the bulk counterpart.<sup>[10c]</sup> When the growth temperature increases, the composition approaches to nearly-stoichiometric CuIn<sub>1.1</sub>Se<sub>2.1</sub> and the tetragonal distortion is gradually released to  $\sim 1.02$ . This result might be due to both the copper vacancy annihilation and lattice strain relaxation by the formation of larger-sized QDs.

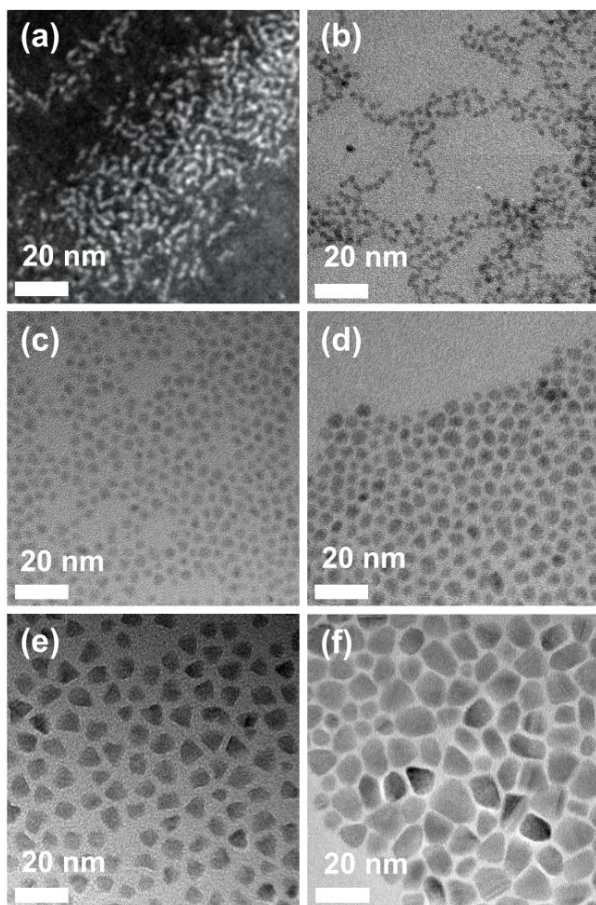


**Figure 2.1** (a) Scanning transmission electron microscope (STEM) image of 2.5 nm CISe QDs, and TEM images of (b) 3 nm, (c) 4 nm, (d) 5 nm, (e) 7 nm, and (f) 10 nm CISe QDs.

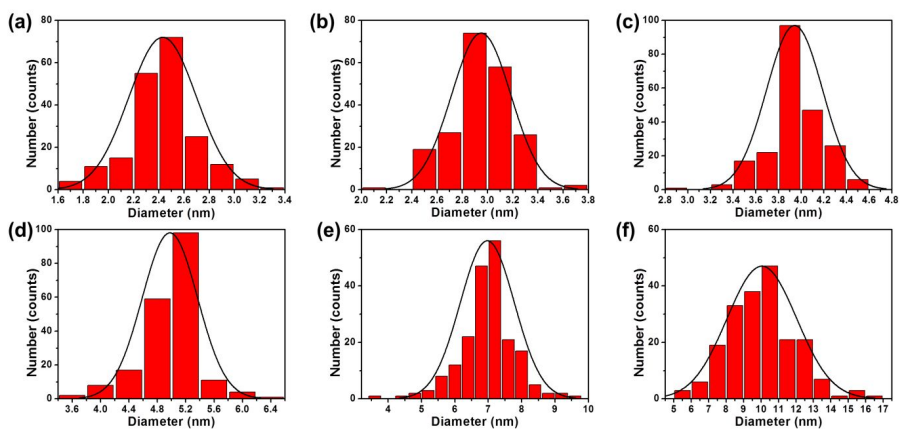


**Figure 2.2** The size distribution histograms of (a) 2.4 nm; (b) 2.9 nm; (c) 3.9 nm; (d) 5.0 nm; (e) 7.0 nm; and (f) 10.0 nm-sized CISE QDs.

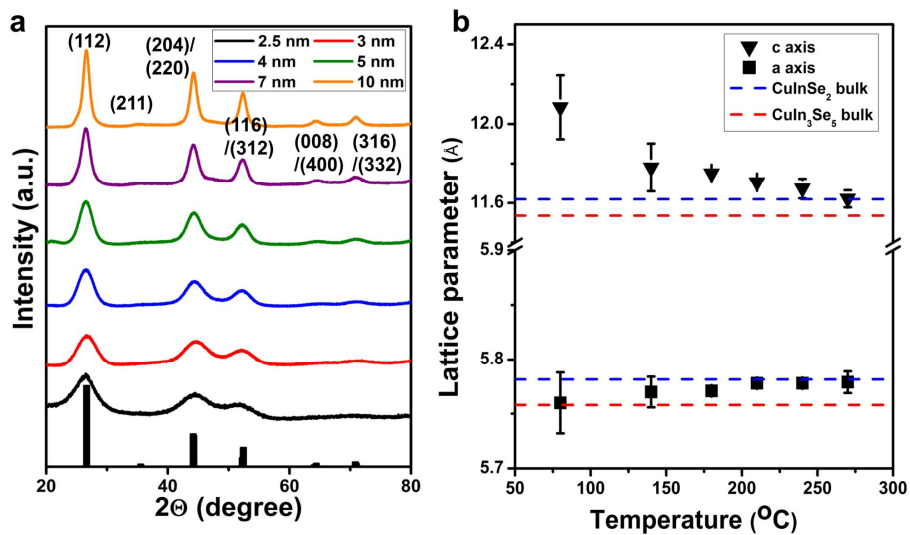


**Figure 2.3** (a) XRD patterns of CISe QDs with tetragonal  $\alpha$ -CuInSe<sub>2</sub> JCPDS #40-1487 shown below (black bar). (b) Lattice parameters of CISe QDs estimated from XRD patterns. The coloured lines represent the lattice parameters of bulk  $\alpha$ -CuInSe<sub>2</sub> (blue) and  $\beta$ -CuIn<sub>3</sub>Se<sub>5</sub> (red).

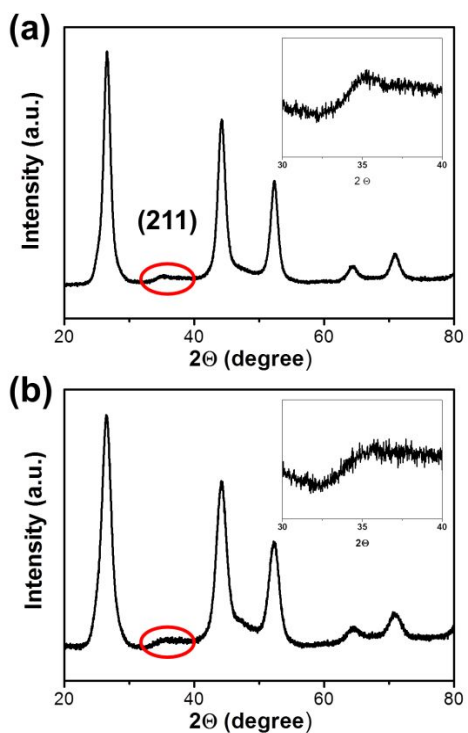


**Figure 2.4** Enlarged XRD patterns of (a) 10 nm- and (b) 7.0 nm-sized CISE QDs. The insets show the existence of (211) reflection, which is a characteristic of chalcopyrite copper indium selenide crystal structure.

**Table 2.1** Characterization of CInSe QDs with various compositions and sizes, obtained from TEM and XRD data.

Growth Temperature [°C]	In/Cu Ratio	Size (size dev.) [nm]	Lattice Constant <i>a</i> [Å]	Lattice Constant <i>c</i> [Å]	Tetragonal Distortion ( <i>c/2a</i> )
80	2.5	2.4 (11.1%)	5.760	12.084	1.049
140	2.1	2.9 (8.0%)	5.770	11.780	1.021
180	1.5	3.9 (6.3%)	5.771	11.750	1.018
210	1.25	5.0 (7.9%)	5.778	11.705	1.013
240	1.2	7.0 (11.7%)	5.778	11.673	1.010
270	1.1	10.0 (19.9%)	5.779	11.621	1.005

### 2.3.2 Band Alignment Engineering of Cu–In–Se QDs

The absorption by the CISE QDs covers the whole visible wavelength range (Fig. 2.5), suggesting the possibility of utilization of the entire solar spectrum for PV device applications. The distinct shoulder in the absorption spectrum is also indicative of the uniform size distribution of the QDs. The band gap can be widely tuned in the NIR region by varying the size and composition of the QDs (Fig. 2.5b) (Please note that calculated excitation Bohr radius is 8.9 nm for  $\text{CuInSe}_2$  and 5.2 nm for  $\text{CuIn}_3\text{Se}_5$ ). The optical band gap is blue shifted from the band gaps of bulk  $\alpha$ - $\text{CuInSe}_2$  (1.04 eV) and  $\beta$ - $\text{CuIn}_3\text{Se}_5$  (1.2 eV) owing to the quantum-confinement effect (Fig. 2.6a). In addition, the calculation using a simple particle in a sphere with a finite potential barrier model<sup>[15]</sup> shows that although the band gap of bulk  $\text{CuIn}_3\text{Se}_5$  is higher than that of bulk  $\text{CuInSe}_2$ , the small effective mass of electrons and holes in  $\text{CuInSe}_2$  crystal allows for more size-dependent band gap and band alignment tunability (Fig. 2.6a and b). These results imply that quantum-confinement effect plays a more significant role in determining the band energy level variation than does composition in this strong quantum-confinement regime.

Complimentary to the optical spectroscopy, cyclic voltammetry (CV) experiments were performed to study the electronic band alignment of CISE QDs of various sizes. It is well known that the band alignment of PV

materials is very important for efficient photo-energy conversion.<sup>[16]</sup> Fig. 2.6b shows the size-dependent band edge alignment of QDs. The conduction band minimum (CBM) of the QDs is taken by the first reduction peak position in the CV (Fig. 2.7),<sup>[12b]</sup> and the valence band maximum (VBM) is determined from the CBM and the optical band gap. The experimentally measured energy alignment of CISE QD is finely controlled with respect to its size and matched well with the theoretical value. Compared to the CBM of TiO<sub>2</sub> (-4.3 eV vs. vacuum),<sup>[16a]</sup> that of bulk CISE or QDs larger than ~5 nm is positioned in the lower electron energy level. Consequently, the injection of photo-generated electrons from CISE to TiO<sub>2</sub> is not thermodynamically favorable in the bulk, which is the main reason why efficient QDSCs employing CISE QDs have not been realized yet. However, with a decrease in the size of the CISE QDs, the CBM shifts toward the vacuum level owing to the quantum-confinement effect. The CBM of the CISE QDs shifted above that of TiO<sub>2</sub>, forming a type II heterojunction unlike the case in the bulk. These results suggest that separation of electrons and holes between QDs and TiO<sub>2</sub> can effectively occur in this relatively strong confinement regime, and the following solar cell results demonstrate this effect.

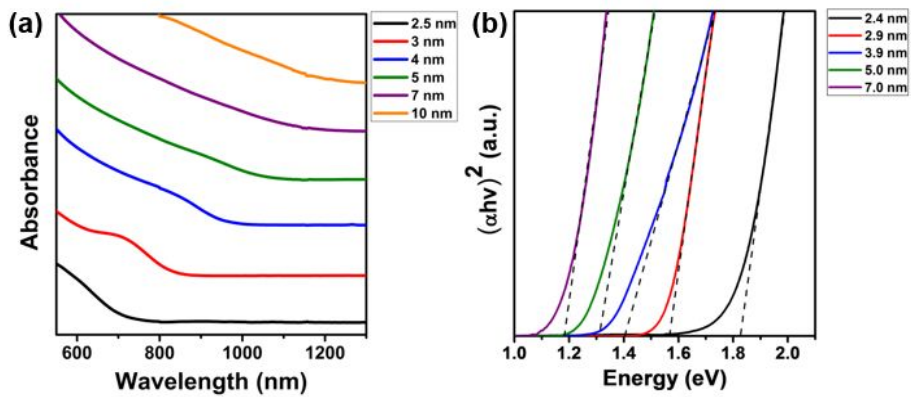


**Figure 2.5** (a) Absorption spectra of the CISe QDs. (b) Plot of  $(\alpha h\nu)^2$  vs. energy from absorption spectrum used to determine the band gap of CISe QDs of various size.

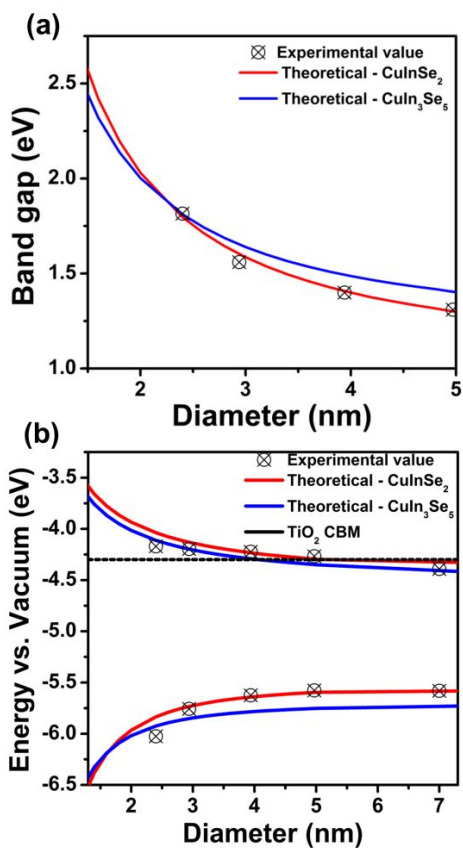


**Figure 2.6** (a) The comparison of the band gaps obtained from the absorption spectra (black dots) with the calculated band gaps (lines). (b) The band edge alignment of CISE QDs obtained from the absorption spectroscopy and cyclic voltammetry (black dots). Experimental values matched well with the theoretical calculation for CuInSe<sub>2</sub> (red line) and CuIn<sub>3</sub>Se<sub>5</sub> (blue line). The black line represents the CBM of TiO<sub>2</sub>.

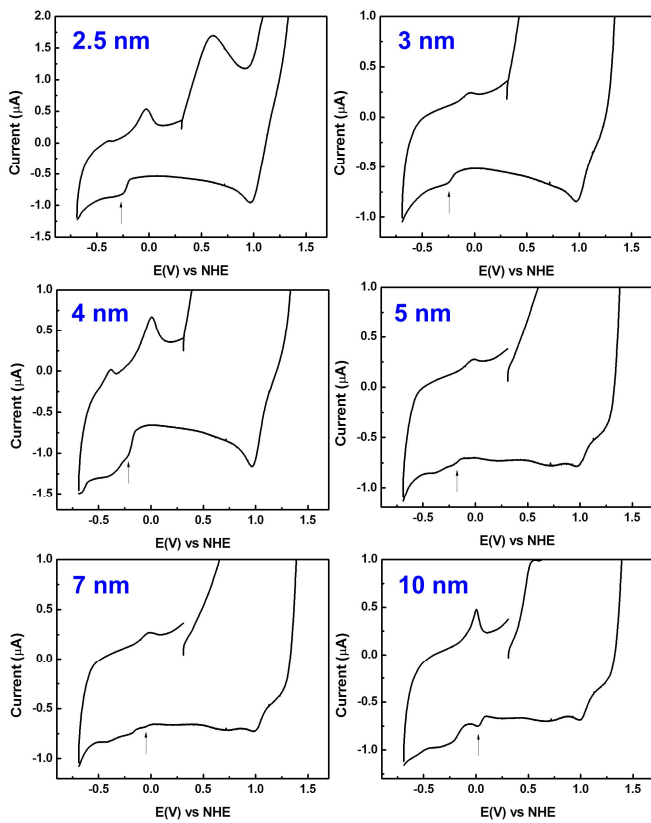


**Figure 2.7** Cyclic voltammograms (CVs) of CISE QDs depending on the QD size.

### 2.3.4 Size-Dependant Photovoltaic Characterization of Cu–In–Se QDs

Finally, we employed the CISe QDs as the photosensitizer in QDSCs. A mesoporous TiO<sub>2</sub> film on FTO glass was used as the electron transport layer and dipped into the diluted solution of QDs in dichloromethane. Even without any post treatment such as ligand exchange or addition of molecular linker, QDs of all sizes adsorb well onto the TiO<sub>2</sub> films (Fig. 2.8). Fig. 2.9a shows the dependence of the IPCE spectra of the QDSCs on the QD size. The absorption range in the IPCE spectra clearly shows the quantum-confinement effect. The QDSC with 2.5 nm QDs exhibits an onset wavelength of 750–800 nm and cannot absorb photons in the NIR region. However, the absorption range is greatly extended even by a small increase in the QD size. QDSCs with 3, 4, and 5 nm QDs exhibit onset wavelengths of about 920, 1080, and 1170 nm, respectively. This extensive control of the light absorption range indicates that the CISe QDs prepared in this study are very promising for the realization of panchromatic solar cells.<sup>[17]</sup> The onset wavelength increases up to about 1200 nm for the 7 and 10 nm QDs. However, the corresponding QDSCs show very low IPCE values, which may be due to unfavourable energetics for electron injection. In addition, the relatively large size of the QDs can lead to the sparse adsorption onto the mesoporous TiO<sub>2</sub> film, resulting in increased electron recombination with the

electrolyte.<sup>[18]</sup> The onset of the IPCE spectrum for each QDSC is red-shifted compared to that expected from the optical band gap of the QD, which indicates the electronic coupling between neighboring QDs in the device.<sup>[9g]</sup>

The photocurrent density–voltage ( $J$ – $V$ ) characteristics of the QDSCs under illumination are shown in Fig. 2.9b, and the results are summarized in Table 2.2. The trends in the short-circuit current ( $J_{sc}$ ) match well with the IPCE data. As mentioned above, larger QDs show a wider range of light absorption; however, they are unfavourable for electron injection into the TiO<sub>2</sub> CB. Due to this trade-off, the performance of QDSCs is optimized with 4 nm QDs, yielding a conversion efficiency of 4.30%. The highest open-circuit voltage ( $V_{oc}$ ) observed for the 4 nm QDs can be attributed to the large amount of injected electrons resulting from the suitable energetics toward light absorption and injection of electrons into the TiO<sub>2</sub> CB. It is noteworthy that the 4 nm QDs exhibited the highest  $J_{sc}$  as well as the highest  $V_{oc}$ , although the energy difference between their CBM and that of TiO<sub>2</sub> is relatively small. In several previous studies of sensitization-type solar cells, PbS QDs or (CH<sub>3</sub>NH<sub>3</sub>)PbI<sub>3</sub> perovskite sensitizers exhibit reasonably high photocurrents and conversion efficiencies in spite of a small driving force (< 0.07 eV) for the electron injection into the TiO<sub>2</sub> CB.<sup>[19]</sup> Considering these previous studies, the energy difference between the 4 nm CISE QDs and TiO<sub>2</sub> in this study

may be sufficient for the effective electron injection.

The amount of injected electrons is compared using the impedance analysis.<sup>[18]</sup> Fig. 2.10 shows Nyquist diagrams of the QDSCs obtained under illumination at  $V_{oc}$ . As shown in the inset, the equivalent circuit model is composed of series resistance ( $R_s$ ), the impedance at the electrolyte/ $Cu_2S$  counter electrode ( $R_{CE}$  and  $CPE_1$ ), and at the electrolyte/ $TiO_2$  electrode ( $R_{ct}$  and  $CPE_2$ ). CPE stands for a “constant phase element,” which represents the interfacial capacitance, often replacing a capacitor in the equivalent circuit for electrodes with roughness.<sup>[18d]</sup> From  $CPE_2$ , the chemical capacitance ( $C_{\mu}$ ) of the  $TiO_2$  electrode can be obtained. The parameters fitted by ZView software are listed in Table 2.3. In addition, we also measured the impedance spectra in the dark state at bias potentials ranging from  $-0.25$  to  $-0.50$  V. The evaluated  $R_{ct}$ ,  $C_{\mu}$ , and electron lifetime ( $\tau_n$ ) values are plotted as functions of bias potentials in Fig. 2.11. The  $\tau_n$  values are obtained by the product of  $R_{ct}$  and  $C_{\mu}$ .<sup>[18a,d]</sup> It is well known that the densely adsorbed QDs on surface of  $TiO_2$  can reduce the electron recombination with the electrolyte.<sup>[18a]</sup> Accordingly, the coating density of the QDs on the  $TiO_2$  electrode affects the  $R_{ct}$  significantly. In this aspect, the larger QDs are unfavourable for dense coating on the surface of  $TiO_2$  electrode, which would lead to the lower  $R_{ct}$ . However, we find that the QDs with too small sizes exhibited relatively

unstable colloidal dispersion, which are unfavourable for dense coating as well. As a result, in the dark state, the medium-sized QDs (4 and 5 nm) showed highest  $R_{ct}$  (Fig. 2.11a). On the other hand,  $C_{\mu}$  values as functions of bias potentials are similar for all sizes of QDs, and do not show a noticeable trend according to the size of QDs, as shown in Fig. 2.11b. This implied that the size of QDs did not affect greatly the  $\text{TiO}_2$  CB potential.<sup>[18a,d]</sup> Consequently, the trends in  $\tau_n$  are similar to those in  $R_{ct}$ , as shown in Fig. 2.11c.

Under illumination, the trends in  $C_{\mu}$  are in good agreement with  $V_{oc}$  depending on the QD size, as listed in Table 2.2 and 2.3. The  $C_{\mu}$  stands for the degree of electron accumulation in the  $\text{TiO}_2$  film,<sup>[18c]</sup> and the size of QDs cannot affect the  $\text{TiO}_2$  CB potential as already confirmed by the impedance analysis in dark state. Therefore, it can be interpreted that the trends in  $C_{\mu}$  and  $V_{oc}$  resulted from the amount of injected electrons depending on the QD size. In addition, the larger  $R_{ct}$  and  $\tau_n$  of the small QDs (2.5–5 nm) compared to those of the larger QDs (7 and 10 nm) at the same bias potentials may reduce the recombination loss of injected electrons, contributing to the higher  $V_{oc}$ . In brief, both the amount of injected electrons and the electron recombination rate determine the trends in  $V_{oc}$ .

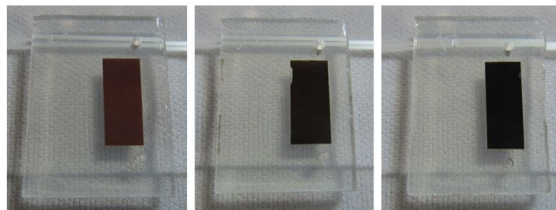
The best conversion efficiency of 4.30% observed in this study is

remarkable. To the best of our knowledge, the current conversion efficiency of 4.30% is the highest among heavy-metal-free QD solar cells, regardless of the device type (June, 2013). The PV performances of the CISE QDSC can be further enhanced by surface treatment of QDs,<sup>[9c,20a,b]</sup> combination with other kinds of QDs<sup>[11b]</sup> or organic dyes,<sup>[20c-e]</sup> or optimizing mesoporous semiconductor layers.<sup>[20f]</sup>

**[Bare TiO<sub>2</sub> film]**



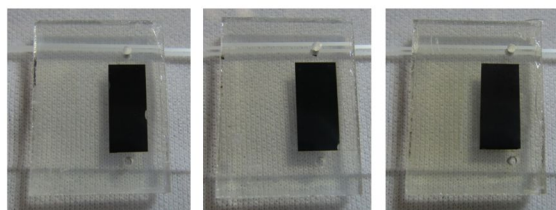
**[CISe QD-sensitized TiO<sub>2</sub> film]**



**2.5 nm**

**3 nm**

**4 nm**



**5 nm**

**7 nm**

**10 nm**

**Figure 2.8** Optical images showing the illumination side of the TiO<sub>2</sub>/QD films on FTO glasses depending on the QD size.

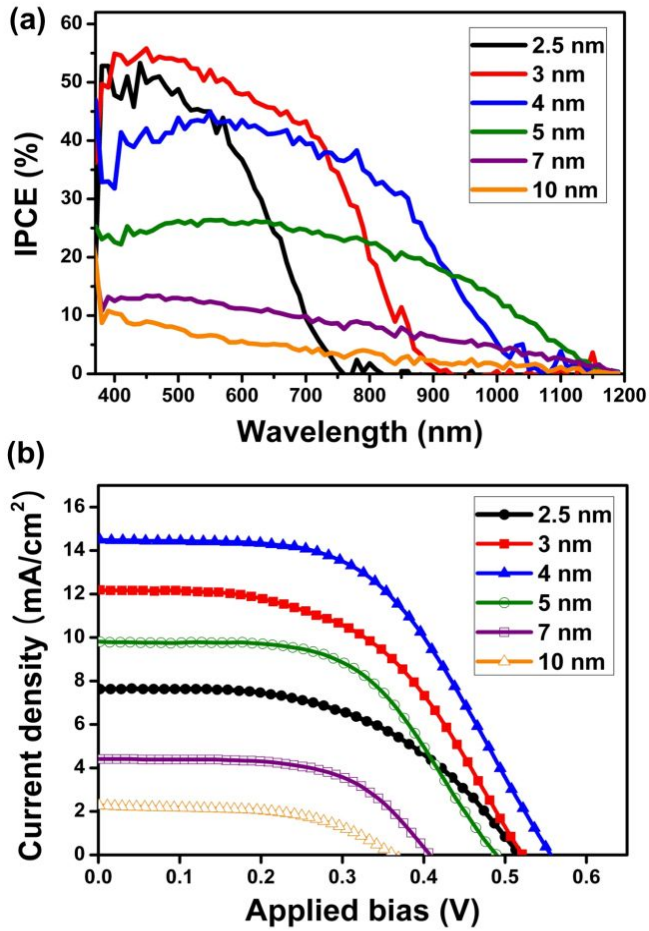


**Figure 2.9** (a) IPCE spectra and (b)  $J-V$  characteristics under illumination (one sun light intensity with AM 1.5 G filter) of the CISE QDSCs with various-sized QDs.

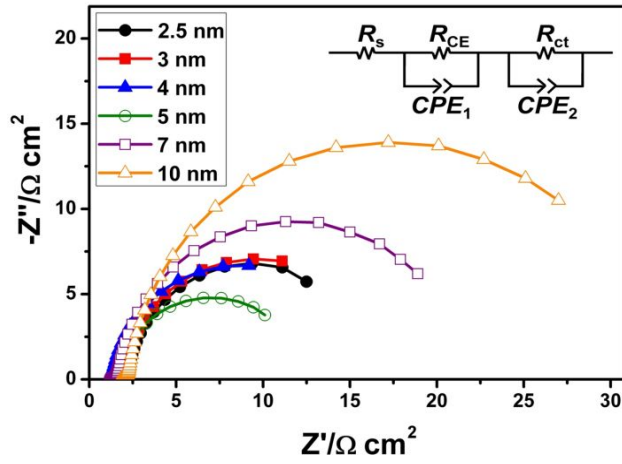


**Figure 2.10** Impedance spectra under illumination at  $V_{oc}$  (one sun light intensity with AM 1.5 G filter) of the CISE QDSCs with various-sized QDs. The inset shows the equivalent circuit model.

**Table 2.2** Summary of photovoltaic characteristics.

QD Size [nm]	Active Area [cm <sup>2</sup> ]	$V_{oc}$ [V]	$J_{sc}$ [mA cm <sup>-2</sup> ]	Fill Factor [%]	PCE [%]
2.5	0.37	0.52	7.64	52	2.07
3	0.37	0.52	12.18	52	3.29
4	0.39	0.56	14.48	53	4.30
5	0.42	0.49	9.81	56	2.69
7	0.40	0.41	4.41	60	1.08
10	0.39	0.36	2.28	54	0.44

**Table 2.3** Summary of impedance parameters under illumination.

QD Size [nm]	$R_{ct}$ [ $\Omega \text{ cm}^2$ ]	$C_{\mu}$ [mF $\text{cm}^{-2}$ ]
2.5	14.91	8.48
3	15.07	9.34
4	14.52	11.10
5	10.55	7.74
7	20.88	3.33
10	30.62	2.51

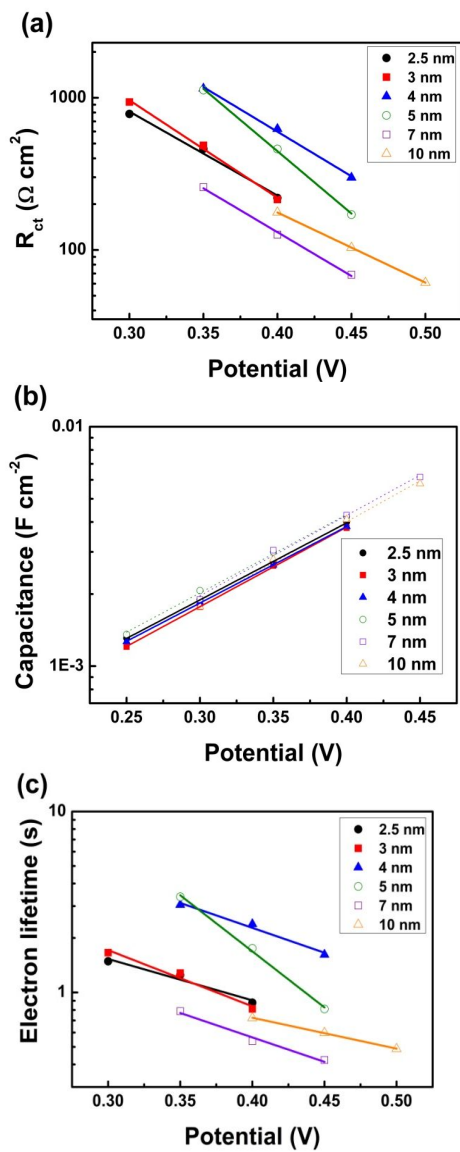


**Figure 2.11** (a) Recombination resistance, (b) chemical capacitance, and (c) electron lifetime of the CISE QDSCs with various-sized QDs, evaluated from the impedance spectra in the dark state.

## 2.4 Conclusion

In this study, heavy-metal-free QDSCs, which exhibit a conversion efficiency up to ~4.3%, are developed based on NIR-energy-band-engineered CISE QDs. Even without the introduction of any kind of heavy metals, CISE QDs enable the fabrication of efficient solar cells with performances comparable to that of the QD solar cells based on toxic cadmium and/or lead chalcogenides. Our new synthetic method produces composition and size-controlled CISE QDs with a narrow size distribution. Furthermore, the current synthetic procedure can be readily applied to the large-scale production of CISE QDs with high reaction yield, which is beneficial for low-cost PV applications. Depending on the QD size, the band energy alignment and light absorption range of the CISE QDSCs are finely tuned in the quantum-confinement regime. The best PV performance is achieved for 4 nm-sized CISE QDs, by optimizing the energetics of the QDs toward effective light absorption and injection of electrons. Our results show that CISE QDs are promising materials for the fabrication of efficient and ecofriendly next-generation solar cells.

\*\*Parts of this chapter were published in the article, “Copper–Indium–Selenide Quantum Dot-Sensitized Solar Cells.” (*Physical Chemistry Chemical Physics* **2013**, *15*, 20517).

## 2.5 References

- [1] (a) Murray, C. B.; Norris, D. J.; Bawendi, M. G. *J. Am. Chem. Soc.* **1993**, *115*, 8706. (b) *Nanocrystal Quantum Dots*, ed. Klimov, V. I. CRC Press, Boca Raton, 2nd edn, 2010.
- [2] (a) Kamat, P. V. *J. Phys. Chem. C* **2008**, *112*, 18737. (b) Zhang, Q.; Uchaker, E.; Candelariaza, S. L.; Cao, G. *Chem. Soc. Rev.* **2013**, *42*, 3127 (c) Nozik, A. J.; Beard, M. C.; Luther, J. M.; Law, M.; Ellingson, R. J.; Johnson, J. C. *Chem. Rev.* **2010**, *110*, 6873.
- [3] (a) Ginger, D. S.; Greenham, N. C. *J. Appl. Phys.* **2000**, *87*, 1361. (b) Huynh, W. U.; Dittmer, J. J.; Alivisatos, A. P. *Science* **2002**, *295*, 2425. (c) Law, M.; Luther, J. M.; Song, Q.; Beard, M. C.; Nozik, A. J. *ACS Nano*, **2008**, *2*, 271. (d) Talapin, D. V.; Shevchenko, E. V.; Bodnarchuk, M. I.; Chen, J.; Ye, X.; Murray, C. B. *Nature* **2009**, *461*, 892. (e) Talapin, D. V.; Lee, J.-S.; Kovalenko, M. V.; Shevchenko, E. V. *Chem. Rev.* **2010**, *110*, 389.
- [4] (a) Ellingson, R. J.; Beard, M. C.; Johnson, J. C.; Yu, P.; Micic, O. I.; Nozik, A. J.; Shabaev, A.; Efros, A. L. *Nano Lett.* **2005**, *5*, 865. (b) Pandey, A.; Guyot-Sionnest, P. *Science* **2008**, *322*, 929. (c) Tisdale, W. A.; Williams, K. J.; Timp, B. A.; Norris, D. J.; Aydil, E. S.; Zhu, X.-Y. *Science* **2010**, *328*, 1543. (d) McGuire, J. A.; Joo, J.; Pietryga, J. M.; Schaller, R. D.; Klimov, V. I. *Acc. Chem. Res.*,

**2008**, *41*, 1810. (e) Sambur, J. B.; Novet, T.; Parkinson, B. A. *Science* **2010**, *330*, 63. (f) Semonin, O. E.; Luther, J. M.; Choi, S.; Chen, H.-Y.; Gao, J.; Nozik, A. J.; Beard, M. C. *Science*, **2011**, *334*, 1530.

[5] (a) Zhang, Y.; Xie, C.; Su, H.; Liu, J.; Pickering, S.; Wang, Y.; Yu, W. W.; Wang, J.; Wang, Y.; Hahn, J.; Dellas, N.; Mohny, S. E.; Xu, J. *Nano Lett.* **2011**, *11*, 329. (b) Yang, X.; Zhao, D.; Leck, K. S.; Tan, S. T.; Tang, Y. X.; Zhao, J.; Demir, H. V.; Sun, X. W. *Adv. Mater.* **2012**, *24*, 4180. (c) Shirasaki, Y.; Supran, G. J.; Bawendi, M. G.; Bulović, V. *Nat. Photon.* **2013**, *7*, 13.

[6] (a) Derfus, A. M.; Chan, W. C. W.; Bhatia, S. N. *Nano Lett.* **2004**, *4*, 11. (b) Lewinski, N.; Colvin, V.; Drezek, R. *Small* **2008**, *4*, 26. (c) Yu, J. H.; Kwon, S.-H.; Petrášek, Z.; Park, O. K.; Jun, S. W.; Shin, K.; Choi, M.; Park, Y. I.; Park, K.; Na, H. B.; Lee, N.; Lee, D. W.; Kim, J. H.; Schwille, P.; Hyeon, T. *Nat. Mater.* **2013**, *12*, 359.

[7] (a) Xie, R.; Rutherford, M.; Peng, X. *J. Am. Chem. Soc.* **2009**, *131*, 5691. (b) Pons, T.; Pic, E.; Lequeux, N.; Cassette, E.; Bezdetnaya, L.; Guillemin, F.; Marchal, F.; Dubertret, B.; *ACS Nano* **2010**, *4*, 2531. (c) Cassette, E.; Pons, T.; Bouet, C.; Helle, M.; Bezdetnaya, L.; Marchal, F.; Dubertret, B. *Chem. Mater.* **2010**, *22*, 6117.

[8] (a) Tang, J.; Hinds, S.; Kelley, S. O.; Sargent, E. H. *Chem. Mater.* **2008**, *20*, 6906. (b) Allen, P. M.; Bawendi, M. G. *J. Am. Chem. Soc.* **2008**, *130*, 9240. (c)

Koo, B.; Patel, R. N.; Korgel, B. A. *J. Am. Chem. Soc.* **2009**, *131*, 3134. (d) Reifsnyder, D. C.; Ye, X.; Gordon, T. R.; Song, C.; Murray, C. B. *ACS Nano* **2013**, *7*, 4307.

[9] (a) Panthani, M. G.; Akhavan, V.; Goodfellow, B.; Schmidtke, J. P.; Dunn, L.; Dodabalapur, A.; Barbara, P. F.; Korgel, B. A. *J. Am. Chem. Soc.* **2008**, *130*, 16770. (b) Akhavan, V. A.; Goodfellow, B. W.; Panthani, M. G.; Reid, D. K.; Hellebusch, D. J.; Adachi, T.; Korgel, B. A. *Energy Environ. Sci.* **2010**, *3*, 1600. (c) Stolle, C. J.; Panthani, M. G.; Harvey, T. B.; Akhavan, V. A.; Korgel, B. A. *ACS Appl. Mater. Interfaces* **2012**, *4*, 2757. (d) Guo, Q.; Kim, S. J.; Kar, M.; Shafarman, W. N.; Birkmire, R. W.; Stach, E. A.; Agrawal, R.; Hillhouse, H. W. *Nano Lett.* **2008**, *8*, 2982. (e) Chang, S.-H.; Chiang, M.-Y.; Chiang, C.-C.; Yuan, F.-W.; Chen, C.-Y.; Chiu, B.-C.; Kao, T.-L.; Lai, C.-H.; Tuan, H.-Y. *Energy Environ. Sci.* **2011**, *4*, 4929. (f) Jeong, S.; Lee, B.-S.; Ahn, S.; Yoon, K.; Seo, Y.-H.; Choi, Y.; Ryu, B.-H. *Energy Environ. Sci.* **2012**, *5*, 7539. [g] Panthani, M. G.; Stolle, C. J.; Reid, D. K.; Rhee, D. J.; Harvey, T. B.; Akhavan, V. A.; Yu, Y.; Korgel, B. A. *J. Phys. Chem. Lett.*, **2013**, *4*, 2030.

[10] (a) Guo, Q.; Ford, G. M.; Yang, W.-C.; Walker, B. C.; Stach, E. A.; Hillhouse, H. W.; Agrawal, R.; *J. Am. Chem. Soc.* **2010**, *132*, 17384. (b) Jasieniak, J.; MacDonald, B. I.; Watkins, S. E.; Mulvaney, P. *Nano Lett.* **2011**,

11, 2856. (c) MacDonald, B. I.; Martucci, A.; Rubanov, S.; Watkins, S. E.; Mulvaney, P.; Jasieniak, J. J. *ACS Nano* **2012**, *6*, 5995.

[11] (a) Li, T.-L.; Teng, H. *J. Mater. Chem.* **2010**, *20*, 3656. (b) Li, T.-L.; Lee, Y.-L.; Teng, H. *Energy Environ. Sci.* **2012**, *5*, 5315. (c) Santra, P. K.; Nair, P. V.; Thomas, K. G.; Kamat, P. V. *J. Phys. Chem. Lett.* **2013**, *4*, 722. (d) McDaniel, H.; Fuke, N.; Pietryga, J. M.; Klimov, V. I. *J. Phys. Chem. Lett.* **2013**, *4*, 355.

[12] (a) Joo, J.; Son, J. S.; Kwon, S. G.; Yu, J. H.; Hyeon, T. *J. Am. Chem. Soc.* **2006**, *128*, 5632. (b) Choi, J. J.; Lim, Y. F.; Santiago-Berrios, M. B.; Oh, M.; Abruña, H. D.; Wise, F. W.; Hanrath, T. *Nano Lett.* **2009**, *9*, 3749. (c) Hyun, B. R.; Zhong, Y.; Bartnik, A. C.; Sun, L.; Abruña, H. D.; Wise, F. W.; Goodreau, J. D.; Matthews, J. R.; Leslie, T. M.; Borrelli, N. F. *ACS Nano* **2008**, *2*, 2206. (d) Koo, H.-J.; Yoo, P. B.; Yoo, K.; Kim, K.; Park, N.-G.; *Inorg. Chim. Acta* **2008**, *361*, 677. (e) H. J. Snaith, *Energy Environ. Sci.* **2012**, *5*, 6513.

[13] (a) Gadzhiev, T. M.; Babaev, A. A.; Gadzhieva, R. M.; Magomedova, D. K.; Khokhlachev, P. P.; *Inorg. Mater.* **2008**, *44*, 1295. (b) Marin, G.; Wasim, S. M.; Rincón, C.; Pérez, G. S.; Power, C.; Mora, A. E.; *J. Appl. Phys.* **1998**, *83*, 3364. (c) McDermott, S.; George, C. B.; Fagas, G.; Greer, J. C.; Ratner, M. A. *J. Phys. Chem. C* **2009**, *113*, 744. (d) Raffaele, R. P.; Forsell, H.; Potdevin, T.; Friedfeld, R.; Mantovani, J. G.; Bailey, S. G.; Hubbard, S. M.; Gordon, E. M.; Hepp, A. F. *Solar Energy Materials & Solar Cells* **1999**, *57*, 167. (e) Meunier, M.; Quirke,

- N.; Binesti, D.; Simulat., Mol. **1999**, *23*, 109. (f) Puzat, F.; Richard, J.; Millié, P. *Mol. Phys.* **1972**, *24*, 1039. (g) Zhang, S. B.; Wei, S.-H.; Zunger, A.; Katayama-Yoshida, H. *Phys. Rev. B* **1998**, *57*, 9642.
- [14] Paszkowicz, W.; Lewandowska, R.; Bacewicz, R.; *J. Alloys & Compounds* **2004**, *362*, 241.
- [15] Schooss, D.; Mews, A.; Eychmüller, A.; Weller, H. *Phys. Rev. B* **1994**, *49*, 17072.
- [16] (a) Grätzel, M. *Nature* **2001**, *414*, 338. (b) Asbury, J. B.; Anderson, N. A.; Hao, E.; Ai, X.; Lian, T. *J. Phys. Chem. B* **2003**, *107*, 7376. (c) Kooops, S. E.; O'Regan, B. C.; Barnes, P. R. F.; Durrant, J. R. *J. Am. Chem. Soc.* **2009**, *131*, 4808.
- [17] (a) K. Lee, S. W. Park, M. J. Ko, K. Kim and N.-G. Park, *Nat. Mater.*, 2009, **8**, 665. (b) S. Ito, I. M. Dharmadasa, G. J. Tolan, J. S. Roberts, G. Hill, H. Miura, J.-H. Yum, P. Pechy, P. Liska, P. Comte and M. Grätzel, *Solar Energy*, 2011, **85**, 1220. (c) P. K. Santra, P. V. Kamat, *J. Am. Chem. Soc.*, 2013, **135**, 877.
- [18] (a) F. Fabregat-Santiago, G. Garcia-Belmonte, I. Mora-Seró and J. Bisquert, *J. Phys. Chem. Chem. Phys.* **2011**, *13*, 9083. (b) Longo, C. ; Nogueira, A. F.; De Paoli, M.-A.; Cachet, H. *J. Phys. Chem. B* **2002**, *106*, 5925. (c) Fabregat-Santiago, F.; Bisquert, J.; Palomares, E.; Otero, L.; Kuang, D.; Zakeeruddin, S.

M.; Grätzel, M. *J. Phys. Chem. C* **2007**, *111*, 6550. (d) Kim, J.-Y.; Kim, J. Y.; Lee, D.-K.; Kim, B. S.; Kim, H.; Ko, M. J. *J. Phys. Chem. C* **2012**, *116*, 22759.

[19] (a) Lee, J.-W.; Son, D.-Y.; Ahn, T. K.; Shin, H.-W.; Kim, I. Y.; Hwang, S.-J.; Ko, M. J.; Sul, S.; Han, H.; Park, N.-G. *Sci Rep.*, **2013**, *3*, 1050. (b) Kim, H.-S.; Lee, C.-R.; Im, J.-H.; Lee, K.-B.; Moehl, T.; Marchioro, A.; Moon, S.-J.; Humphry-Baker, R.; Yum, J.-H.; Moser, J. E.; Grätzel, M.; Park, N.-G. *Sci Rep.*, **2012**, *2*, 591.

[20] (a) Liu, Y.; Gibbs, M.; Puthussery, J.; Gaik, S.; Ihly, R.; Hillhouse, H. W.; Law, M. *Nano Lett.* **2010**, *10*, 1960. (b) Lee, J.-S.; Kovalenko, M. V.; Hyang, J.; Chung, D. S.; Talapin, D. V. *Nat. Nanotechnol.* **2011**, *6*, 348. (c) Choi, H.; Santra, P. K.; Kamat, P. V. *ACS Nano* **2012**, *6*, 5718. (d) Cai, N.; Moon, S.-J.; Cevey-Ha, L.; Moehl, T.; Humphry-Baker, R.; Wang, P.; Zakeeruddin, S. M.; Grätzel, M. *Nano Lett.* **2011**, *11*, 1452. (e) Bai, Y.; Zhang, J.; Zhou, D.; Wang, Y.; Zhang, M.; Wang, P. *J. Am. Chem. Soc.* **2011**, *133*, 11442. (f) Crossland, E. J. W.; Noel, N.; Sivaram, V.; Leijtens, T.; Alexander-Webber, J. A.; Snaith, H. J. *Nature* **2013**, *495*, 215.

# **Chapter 3. Improved Photovoltaic Characteristics of Copper–Indium–Selenide Quantum Dots by Suppressing Carrier Recombination *via* Surface Engineering**

## **3.1 Introduction**

In recent years, the synthesis of colloidal quantum dots (QDs)<sup>[1]</sup> and their potential applications in third-generation photovoltaic devices<sup>[2,3]</sup> have received significant attention due to their unique optoelectronic properties, such as their band gap tunability, high absorption coefficient, slow hot electron cooling, and potential for multiple exciton generation.<sup>[4]</sup> Furthermore, colloidal QDs can be easily solution-processed, allowing for inexpensive device fabrication.<sup>[5]</sup> These properties have led to the recent development of highly efficient QD solar cells, including depleted heterojunction solar cells using PbS QDs<sup>[3e]</sup> and QD-sensitized solar cells (QDSCs) using CdSe<sub>x</sub>Te<sub>1-x</sub>,<sup>[2c]</sup> achieving the conversion efficiencies of 9.2 and 8.55%, respectively. However, these devices, like many others, contain toxic elements such as cadmium<sup>[2]</sup> or lead,<sup>[3]</sup> which may limit commercial

applications, particularly for portable devices.

Environmentally friendly Cu–In–S and Cu–In–Se (CISE) QDs have been under development as alternatives to these toxic materials.<sup>[4d,e,6]</sup> The Korgel group developed heterojunction solar cells employing CuInSe<sub>2</sub> QDs containing a CdS buffer layer.<sup>[6b-d]</sup> Meanwhile, the Klimov group reported QDSCs utilizing CuInSe<sub>x</sub>S<sub>2-x</sub> QDs subjected to partial Cd<sup>2+</sup> cation exchange; these devices yielded a conversion efficiency of 5.5%.<sup>[6e]</sup> In addition, the Zhong group reported heavy metal-free QDSCs based on CuInS<sub>2</sub><sup>[6f]</sup> and CuInSe<sub>2</sub><sup>[6g]</sup> QDs; these devices exhibited reasonable conversion efficiencies of 7.04 and 6.79%, respectively. However, there is still a huge gap between the performance of these QDSCs and that of conventional cadmium- and lead-chalcogenide QD based devices, which might be due to the lack of understandings on the control of the charge carriers in these I–III–VI QDs.

In this chapter, we demonstrate that the photovoltaic performance of CISE QD-sensitized solar cells (QDSCs) can be greatly enhanced simply by optimizing the thickness of ZnS overlayers on the QD-sensitized TiO<sub>2</sub> electrodes. In general, these kind of photoanodic overlayers are deposited by 2–4 cycles of a successive ionic layer adsorption and reaction (SILAR) process.<sup>[2c,6e-g,7]</sup> However, in this study, we reveal that much thicker ZnS overlayers compared to the conventional one are required to sufficiently

suppress the carrier recombination and optimize performance in CISE QDSCs. The physical and chemical nature of the overlayers is determined and its influence on the optical, energetic, and kinetic characteristics of the photoanode is investigated, in particular, by focusing on the interfacial and non-radiative recombination in the QDSCs. Due to a combination of both the low optical band gap of CISE QDs that allows for effective light absorption over a broad range of wavelength as well as the reduced carrier recombination by the controlled ZnS overlayers, a remarkable conversion efficiency of 8.10% can be obtained under one sun illumination, which is a record for heavy metal-free QD solar cells at the current (Oct., 2015).

## 3.2 Experimental Section

### 3.2.1 Synthesis of 4 nm sized Cu–In–Se QDs

CISE QDs with an average size of 4 nm were synthesized in this study. Standard Schlenk techniques under an argon atmosphere were used for all steps. In a typical synthesis, 0.5 mmol of copper (I) iodide (Alfa Aesar, 99.998%) and 0.5 mmol of indium (III) iodide (Alfa Aesar, 99.999%) were mixed into 15.0 mL of oleylamine (Acros, approximate C18 content 80–90%). The mixture was heated under vacuum at 120 °C to form metal-amine complexes. Simultaneously, 5.0 mmol of selenium (Aldrich, 99.99%), 10.0 mL of oleylamine, and carbon monoxide gas were mixed to form oleylammonium selencabamate. Then, 1.0 mmol of oleylammonium selencabamate was injected to the metal-amine solution at 70 °C. The reaction mixture rapidly turned black, suggesting the generation of QDs. The solution was heated to 180 °C and was left to react for 20 min. The product was purified using solvent/non-solvent systems with subsequent centrifugation. Excess ethanol containing trioctylphosphine (Aldrich, 97%) was added as the non-solvent. For further characterization and device fabrication, the products were dispersed in anhydrous dichloromethane (Aldrich,  $\geq 99.8\%$ ), or else used as powders.

### 3.2.2 Preparation of QD-sensitized working electrodes

TiO<sub>2</sub> nanoparticles with a size of 20 nm were initially synthesized, as described in a previous report.<sup>[8a]</sup> This process involved hydrolyzing titanium isopropoxide (97%, Aldrich) with acetic acid, followed by autoclaving at 230 °C for 12 h. The prepared TiO<sub>2</sub> nanoparticles were dissolved in ethanol, after which ethyl cellulose (Aldrich), lauric acid (Fluka), and terpineol (Fluka) were added and mixed. The ethanol was subsequently removed using a rotary evaporator, yielding a viscous paste with a TiO<sub>2</sub>/terpineol/ethyl cellulose/lauric acid weight ratio of 0.18:0.75:0.05:0.02. In addition, a scattering paste was prepared using TiO<sub>2</sub> particles with a size of 500 nm (G2, Showa Denko, Japan) following the same procedure as for the 20 nm nanoparticles. Before the pastes were deposited, fluorine doped tin oxide (FTO) glass (TEC-8, Pilkington, 8 Ω/sq) was pretreated with 7.5 wt% Ti(IV) bis(ethyl acetoacetato)-diisopropoxide solution in 1-butanol by spin coating, followed by annealing at 500 °C for 10 min to yield a dense TiO<sub>2</sub> layer. After that, the previously prepared 20 nm TiO<sub>2</sub> paste was deposited on the pretreated FTO by the doctor blade technique, followed by drying at 130 °C for 5 min. The scattering paste was subsequently deposited, followed by annealing at 500 °C for 30 min. The annealed TiO<sub>2</sub> electrodes were then

placed in the CISE QD dispersion for direct QD adsorption.<sup>[8b]</sup> After 48 h, the TiO<sub>2</sub>/QD electrodes were rinsed with dichloromethane and dried by nitrogen flow. Finally, they were coated with a ZnS overlayer by SILAR. This consisted of dipping them first into 0.05 M Zn(NO<sub>3</sub>)<sub>2</sub>·6H<sub>2</sub>O (Aldrich) ethanol solution and the 0.05 M Na<sub>2</sub>S (Aldrich) in methanol/H<sub>2</sub>O (v:v = 1:1) solution for 1 min each. After each dipping, the electrodes were rinsed with deionized water and dried by nitrogen flow. This SILAR process was repeated 3–10 times.

### **3.2.3 Electrode Assembly**

The Cu<sub>2</sub>S counter electrode was prepared by dipping brass foil (Alfa Aesar, 0.25 mm thick) into HCl solution (Daejung, 35–37%) at 80 °C for 30 min. The etched brass foil was rinsed with DI water and dried under nitrogen flow, after which an aqueous polysulfide solution of 1 M Na<sub>2</sub>S and 1 M S (99.998%, Aldrich) was dropped onto it to form a Cu<sub>2</sub>S film on the surface. The TiO<sub>2</sub>/QD working electrode was assembled with the Cu<sub>2</sub>S counter electrode using hot melt Surlyn (Dupont 1702, 60 μm thick). Then, spare parts of both working and counter electrodes were coated by conductive silver paste for good electrical contacts with external circuits. A drop of polysulfide electrolyte comprising 1 M Na<sub>2</sub>S and 1 M S in pure DI water was

injected into the assembled cells through two small predrilled holes at the working electrode. The active area for each cell was in the range of  $0.25 \pm 0.04 \text{ cm}^2$ , which was confirmed using a CCD camera (Moticam 1000) with an image analysis program.

### 3.2.4 Characterization

TEM images were taken by a JEOL 2100F electron microscope. Elemental mapping of the QDs-TiO<sub>2</sub> composites was carried out using high-angle annular dark-field scanning TEM (HAADF-STEM) with an EDS detector. QD composition was determined by inductively coupled plasma-atomic emission spectrometry. The absorption spectra were measured by a CARY 5000E spectrophotometer. XPS was conducted using a Thermo Fisher Scientific Sigma Probe. The composition at the electrode cross-sections was confirmed by EPMA (JEOL JXA-8500F). Standard  $J-V$  measurements were carried out using a class AAB solar simulator (Yamashita Denso YYS-200A) equipped with a 1600 W xenon lamp and an AM 1.5 G filter at a power of  $100 \text{ mW/cm}^2$  with a scan rate of 50 mV/s. During the  $J-V$  measurements, a black mask with an aperture covered the solar cells in order to prevent additional illumination.<sup>[8c]</sup> Incident photon to current conversion efficiency was measured under short circuit conditions as a function of wavelength (10

nm spectral resolution) using a 75 W xenon lamp source and a grating monochromator (PV Measurements). Electrochemical impedance analysis was performed using a Solartron 1287 potentiostat and a Solartron 1260 frequency-response detector in the absence of light and at bias potentials ranging from  $-0.30$  to  $-0.55$  V. Fluorescence emission decay data were obtained by a time-correlated single-photon-counting module in an FLS 980 spectrometer (Edinburgh Instruments, UK) at the emission maximum ( $\sim 850$  nm). A pulsed diode laser (EPL-635, 634.2 nm, 10 MHz repetition, pulse width 88.9 ps) was used as an excitation source. The luminescence was spectrally dispersed in a monochromator ( $600 \text{ gr mm}^{-1}$ ) and detected with a near infrared photomultiplier. The time-correlated single-photon-counting system provided a time window from 10 ns to 100 ns with 8,192 data channels.

### **3.2.4 Comparison Experiments with PbS/CdS QDSCs**

For the comparison with CISE QDSCs, PbS/CdS co-sensitized QDSCs were prepared by a conventional SILAR method according to the previous papers.<sup>[8d,e]</sup> PbS QDs were firstly deposited on the mesoporous  $\text{TiO}_2$  film, by dipping into 0.02 M  $\text{Pb}(\text{NO}_3)_2$  (Aldrich) methanol solution for 1 min, followed by dipping into 0.02 M  $\text{Na}_2\text{S}$  (Aldrich) in methanol/deionized (DI)

water (1:1, v/v) solution for 1 min. After each dipping, the electrode was thoroughly washed with methanol, and this cycle was repeated three times. Subsequently, for the deposition of CdS QDs, the PbS-sensitized TiO<sub>2</sub> electrode was dipped into 0.5 M Cd(NO<sub>3</sub>)<sub>2</sub>·4H<sub>2</sub>O (Aldrich) ethanol solution for 5 min, washed with ethanol. Following this, the electrode was dipped into 0.5 M Na<sub>2</sub>S aqueous solution for 5 min, thoroughly washed with DI water. This cycle was also repeated three times. Finally, the ZnS overlayer was deposited on the PbS/CdS-sensitized TiO<sub>2</sub> electrode by the same SILAR process used for the CISE-QDSCs.

## 3.3 Result and Discussion

### 3.3.1 Working Electrodes with Controlled ZnS Overlayers

In this study, uniform 4 nm sized CISE QDs with a tetragonal chalcopyrite crystal structure and a composition of  $\text{CuIn}_{1.5}\text{Se}_3$  were prepared (Fig. 3.1) by the method in the chapter 2. The absorption spectrum of QD solution (Fig. 3.1c) covers the whole visible light and even the near-infrared (NIR) region, suggesting efficient utilization of the entire solar spectrum. The optical band gap energy ( $E_g$ ) of the QDs is about 1.36 eV, as determined by the extrapolated plot of  $(\alpha h\nu)^2$  vs.  $h\nu$  from the absorption spectrum (the inset of Fig. 3.1c), where  $\alpha$  is the absorption coefficient and  $h\nu$  is the photon energy.<sup>[9]</sup>

For sensitization, the mesoporous  $\text{TiO}_2$  films deposited on FTO glasses were dipped into the CISE QD dispersion in dichloromethane. Subsequently, the surface of QD-sensitized  $\text{TiO}_2$  films was treated with a standard ZnS SILAR process, in order to suppress the electron recombination between the photoanode and the redox couple in the electrolytes.<sup>[2c,7a,b]</sup> Firstly, a control sample was prepared by repeating the ZnS SILAR cycles for 3 times according to the conventional method.<sup>[2c,6e-g,7]</sup> In addition, the number of

SILAR cycles was increased for 6-10 times to study the resulting photovoltaic properties.

Before examining the effects of the thick ZnS overlayers in detail, we first confirm that it is evenly distributed over the surface of CISE-sensitized TiO<sub>2</sub>. Fig. 3.2a shows transmission electron microscopy (TEM) image of the sample with 7 SILAR cycles. Consistent coating is observed with an overall thickness of 1.5–2 nm, which is similar to the thickness of 7 monolayers of ZnS. Fig. 3.2b compares this sample to the control, showing the Ti, Zn, and S K-edge energy-dispersive X-ray spectroscopy (EDS) maps of both. In each case, Zn and S are distributed homogeneously, indicating uniform coating. In addition, uniformity over the cross-section of the film, meanwhile, was examined by an electron probe microanalyzer (EPMA). The CISE QDs are homogeneously adsorbed throughout, as demonstrated by the Cu, In, and Se EPMA images shown in Fig. 3.3. In addition, the Zn and S EPMA images of the electrodes in Fig. 3.4 show a dependence on the number of SILAR cycles. The TiO<sub>2</sub> electrodes are clearly composed of a 13 μm-thick transparent layer (with 20 nm sized TiO<sub>2</sub> nanoparticles) and a 5 μm-thick scattering layer (with 500 nm sized TiO<sub>2</sub> particles). The Zn and S content are particularly high at about 1.5 μm near the interface between the transparent and scattering layer. However, aside from this layer, the Zn and S contents are

distributed uniformly throughout the cross-section in both cases, with more of these elements present after 7 cycles.

We used X-ray photoelectron spectroscopy (XPS) to quantitatively compare the amount of deposited ZnS. Figure 3.5a shows the XPS spectra of CISE-sensitized TiO<sub>2</sub> over the entire scan range for multiple SILAR cycles. Zn, S, Ti, O, and In are observed in the samples after SILAR treatments, indicating successful coating of the ZnS overlayers. Meanwhile, Fig. 3.5b,c shows the high-resolution Zn 2p and S 2p peaks, respectively. In addition, the binding energy (BE) values and the corresponding peak area of the Zn 2p peaks for the samples subjected to 3 and 7 SILAR cycles are listed in Table 3.1. The measured BEs of Zn 2p<sub>3/2</sub> and 2p<sub>1/2</sub> are 1022.0 and 1045.1 eV, respectively, for both samples, values which correspond to the Zn-S bond.<sup>[10]</sup> Additionally, the Zn 2p peak area ratio between the 3 and 7 cycles is about 1:2. Assuming that the ZnS overlayers are coated conformally and the detection limit of XPS is greater than the thickness of ZnS overlayers, it can be roughly estimated that the thickness of overlayers prepared by 7 SILAR cycles is about 2 times greater than that of the control sample.

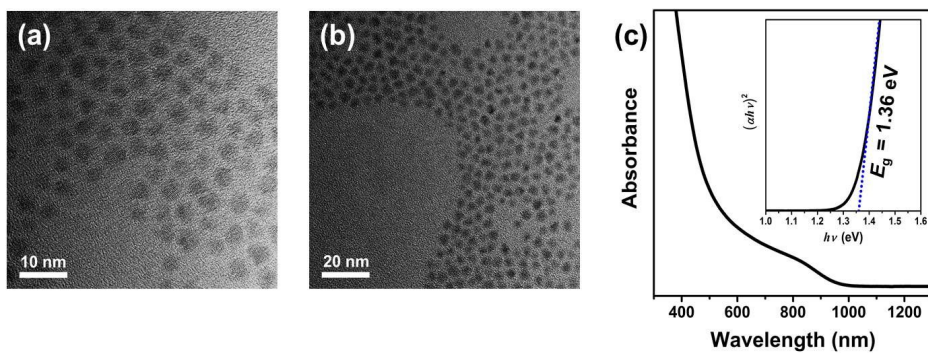


**Figure 3.1** (a,b) TEM images and (c) absorption spectrum of 4 nm CISe QDs dispersed in dichloromethane. The inset of (c) shows the extrapolated plot of  $(\alpha h\nu)^2$  vs.  $h\nu$  obtained from the absorption spectrum and used to obtain the CISe QD band gap.

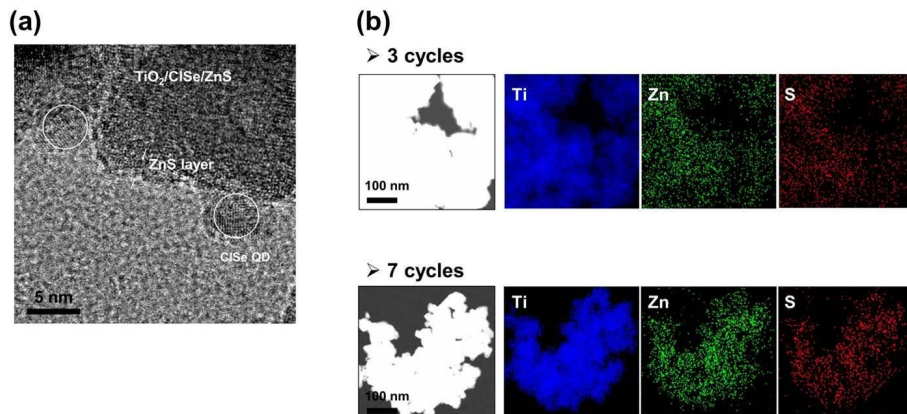


**Figure 3.2** (a) TEM image of CISE-sensitized  $\text{TiO}_2$  after 7 ZnS SILAR cycles. (b) HAADF-STEM images and Ti, Zn, and S EDS maps of CISE-sensitized  $\text{TiO}_2$  with 3 and 7 ZnS SILAR cycles.

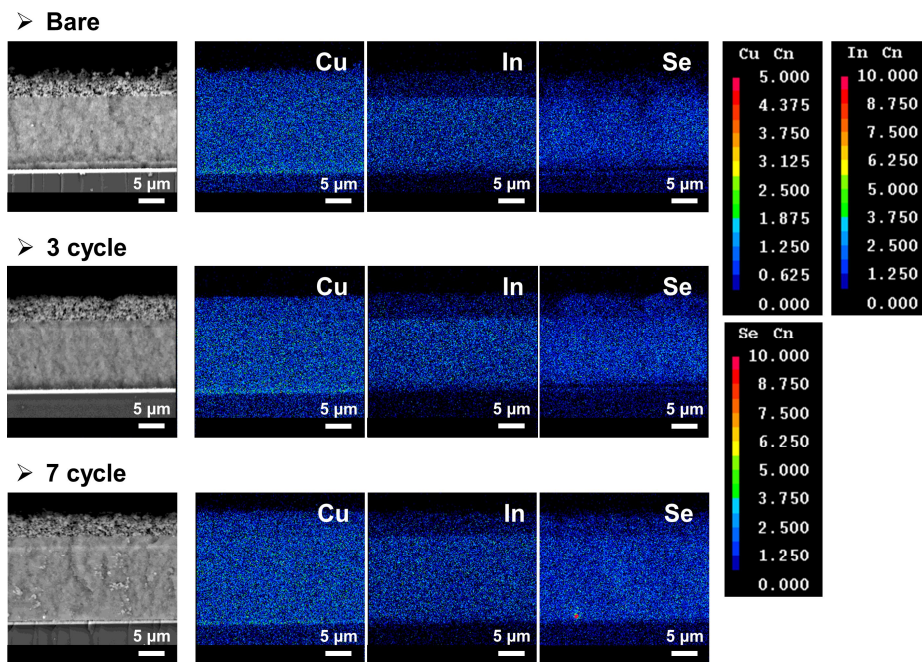


**Figure 3.3** Cu, In, and Se EPMA images of CISE-sensitized TiO<sub>2</sub> electrodes with respect to the number of ZnS SILAR cycles.

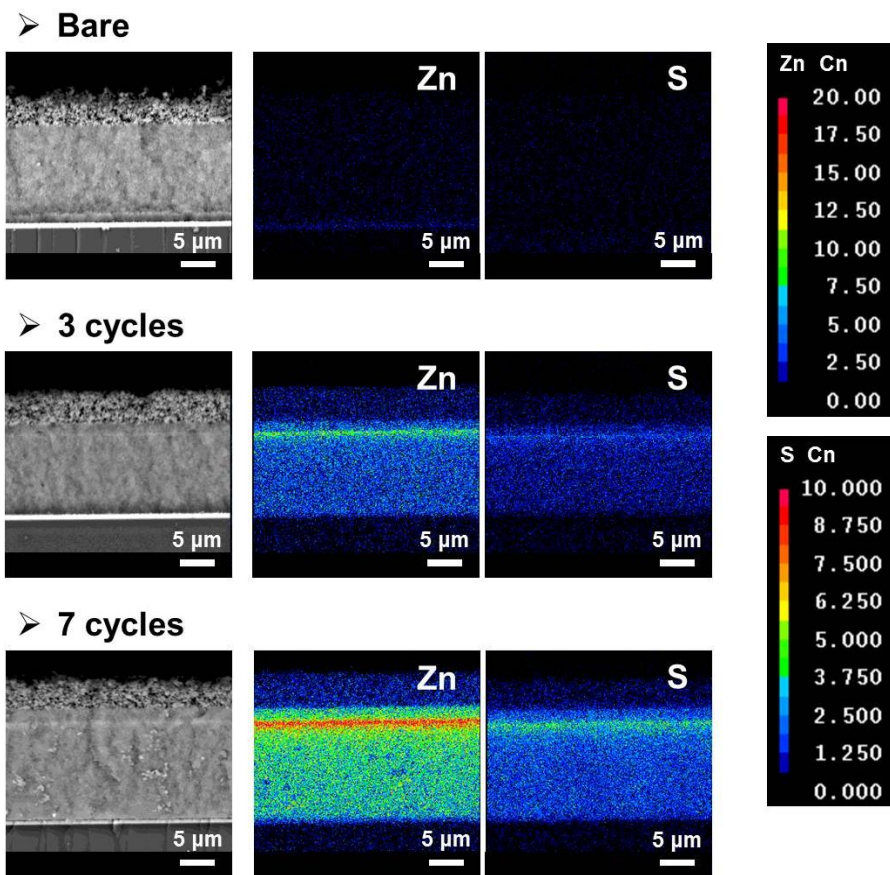


**Figure 3.4** Zn and S EPMA images of the CISE-sensitized  $\text{TiO}_2$  electrodes with respect to the number of ZnS SILAR cycles.

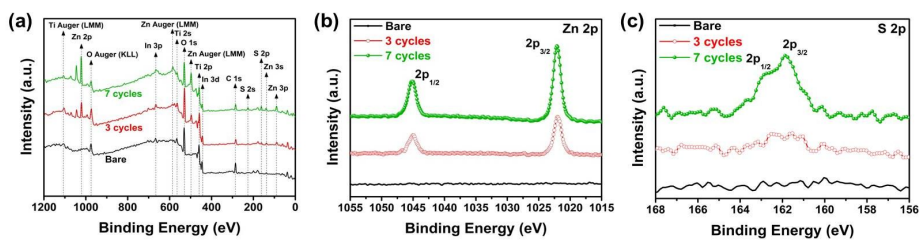


**Figure 3.5** XPS spectra of the CISE-sensitized  $\text{TiO}_2$  electrodes with respect to the number of ZnS SILAR cycles: (a) survey scan and high resolution scans of the (b) Zn 2p and (c) S 2p regions.

**Table 3.1** BE values and peak areas obtained from XPS analysis of the CISE-sensitized TiO<sub>2</sub> electrodes treated with 3 and 7 ZnS SILAR cycles.

ZnS cycles	2p <sub>3/2</sub>		2p <sub>1/2</sub>	
	BE (eV)	Peak area (a.u.)	BE (eV)	Peak area (a.u.)
3 cycles	1022.0	2765	1045.1	1367
7 cycles	1022.0	5604	1045.1	2793
<i>Peak area ratio (3 cycles : 7 cycles)</i>		<i>1 : 2.03</i>	<i>1 : 2.04</i>	

### 3.3.2 Photovoltaic Characterization of Surface Engineered Working Electrodes

The photocurrent density–voltage ( $J$ – $V$ ) of the QDSCs with respect to the number of SILAR cycles is shown in Figure 3.6a, with results summarized in Table 3.2. All values in Table 3.2 are averaged from three different cells for each condition, with the exception of the champion cell, while the complete data set is available in Table 3.3. Notably, all photovoltaic parameters are greatly enhanced after 3 SILAR cycles, with a conversion efficiency roughly 2.3 times greater than the untreated sample. This effect is even more pronounced as the number of cycles increases further; the positive effects reach a maximum of 7 cycles, yielding an enhancement of conversion efficiency of about 40% over the control sample (*i.e.*, 3 cycles).

These results imply that much thicker ZnS overlayers are required for optimal performance when compared to others, more conventional QDSCs.<sup>[2c,6e-g,7]</sup> However, exceeding 7 cycles again decreased conversion efficiency, with an overall decrease in performance with respect to the control sample after 10 cycles. The  $J$ – $V$  curve for this trial suggests that the mesopores in the TiO<sub>2</sub> electrode are partially blocked, limiting diffusion of the redox couple in the polysulfide electrolyte.<sup>[11]</sup> This, along with poor regeneration of the oxidized QDs by the redox couple for the thick

overlayers, likely accounts for this decreased performance following additional SILAR treatment. As shown in Fig. 3.7 and Table 3.4, the sample with 10 SILAR cycles exhibits considerable  $J-V$  hysteresis with respect to the scan direction, despite the sufficiently slow scan rate of 50 mV/s. On the other hand, for the samples with 3 and 7 SILAR cycles,  $J-V$  curve is nearly not influenced by the scan direction. The anomalous hysteresis for the sample with 10 SILAR cycles indicates the imbalance between the electron and hole fluxes,<sup>[11c]</sup> which is an evidence for the poor regeneration of the oxidized QDs by the redox couple resulting from the limiting diffusion of the electrolyte and the thick ZnS overlayers.

Fig. 3.6b shows the external quantum efficiency (EQE,  $\eta_Q$ ) spectra of the QDSCs as a function of wavelength. In addition, the integrated  $J_{SC}$  calculated from the EQE spectra with publicly available data for AM 1.5 G solar irradiation<sup>[12]</sup> is shown in Fig. 3.8. The integrated  $J_{SC}$  and the observed trend are in good agreement with the previously discussed  $J_{SC}$  values measured in the  $J-V$  curves. The QDSCs treated with 7 SILAR cycles exhibited the highest  $\eta_Q$  values and the broadest spectrum, with coverage including the NIR region due to the low optical band-gap of the CISE QDs. The  $E_g$  of the CISE QDs adsorbed onto the  $TiO_2$  surface can be estimated from the EQE spectrum through the relationships  $ah\nu \propto (h\nu - E_g)^{1/2}$  and  $\alpha \propto \ln(1 - \eta_Q)$ .<sup>[13]</sup>

Linear extrapolation of  $[hv \times \ln(1 - \eta_Q)]^2$  vs.  $hv$  yields  $E_g$  values of 1.30, 1.24, and 1.22 eV for the bare sample and those coated with 3 and 7 SILAR cycles, respectively (Fig. 3.6c). Compared to the CISE QDs dispersed in dichloromethane, the  $E_g$  is reduced by 0.06 eV for the QDs adsorbed onto the  $TiO_2$  surface without the ZnS overlayers, attributed to the electronic coupling between neighboring QDs in the device.<sup>[6d]</sup> The transmittance data of CISE-sensitized  $TiO_2$  films exhibit the same trend as shown in Fig. 3.9. Additional reductions by the ZnS overlayers are consistent with previous reports for core-shell colloids,<sup>[14]</sup> and can be ascribed to a reduction in confinement due to the strain effect and a delocalization of the electronic wavefunctions. These decreases in  $E_g$  at least partly account for the enhanced  $J_{SC}$  and  $\eta_Q$  values.

A conversion efficiency of 8.10% can be achieved for the best device in this study. This is the highest value for a heavy metal-free QD solar cell ever reported (Oct., 2015), to the best of our knowledge, and is in fact comparable to the best conversion efficiency ever observed for QDSCs.<sup>[2c]</sup> Again, this effect is likely due to a combination of both the low optical band gap that allows for effective light absorption over a broad range of wavelengths as well as and the optimized surface passivation of the ZnS overlayers.

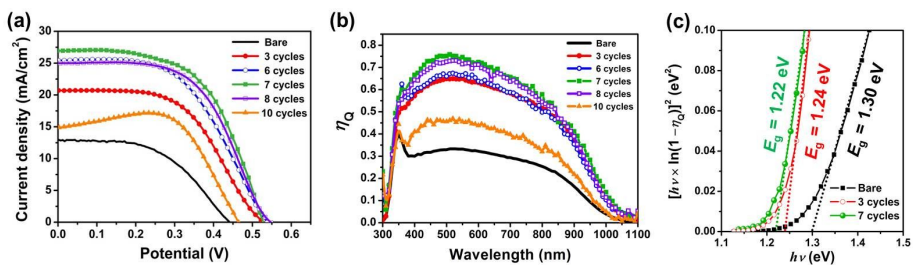


**Figure 3.6** (a)  $J$ - $V$  characteristics under illumination (one sun light intensity with AM 1.5G filter, measured under reverse scan condition) and (b) EQE values ( $\eta_Q$ ) for CISE QDSCs with respect to the number of ZnS SILAR cycles. (c) Extrapolated plot of  $[h\nu \times \ln(1 - \eta_Q)]^2$  vs.  $h\nu$  from the EQE spectrum, used to obtain the optical band gap of the CISE QDs.

**Table 3.2** Summarized  $J-V$  characteristics of the CISE QDSCs with respect to the number of ZnS SILAR cycles

ZnS cycles	$J_{sc}$ <sup>a</sup> (mA/cm <sup>2</sup> )	$V_{oc}$ <sup>a</sup> (mV)	$FF$ <sup>a</sup>	$\eta$ <sup>a</sup> (%)
Bare <sup>b</sup>	11.62	428	0.49	2.44 ± 0.47
3 cycles <sup>b</sup>	22.04	512	0.50	5.64 ± 0.18
6 cycles <sup>b</sup>	23.98	528	0.55	6.96 ± 0.17
7 cycles <sup>b</sup>	26.69	538	0.55	7.90 ± 0.05
8 cycles <sup>b</sup>	25.53	539	0.55	7.57 ± 0.09
10 cycles <sup>b,c</sup>	14.63	438	0.66	4.23 ± 0.61
Champion cell (7 cycles)	26.93	528	0.57	8.10

<sup>a</sup>Measured under reverse scan condition with a scan rate of 50 mV/s.

<sup>b</sup>All parameters were averaged from three different devices.

<sup>c</sup>These cells exhibited considerable hysteresis with respect to the forward and reverse scan directions as shown in Fig. 3.7.

**Table 3.3**  $J$ - $V$  characteristics of the CISE QDSCs.

ZnS cycles	$J_{sc}$ (mA/cm <sup>2</sup> )	$V_{oc}$ (mV)	$FF$	$\eta$ (%)
<b>Bare-1</b>	11.59	429	0.47	2.34
<b>Bare-2</b>	12.91	442	0.51	2.91
<b>Bare-3</b>	10.37	413	0.49	2.10
<b>3 cycles-1</b>	22.92	487	0.50	5.58
<b>3 cycles-2</b>	20.71	530	0.53	5.82
<b>3 cycles-3</b>	22.50	520	0.48	5.62
<b>6 cycles-1</b>	21.84	518	0.60	6.79
<b>6 cycles-2</b>	25.40	537	0.52	7.09
<b>6 cycles-3</b>	24.70	530	0.53	6.94
<b>7 cycles-1</b>	26.93	528	0.57	8.10
<b>7 cycles-2</b>	26.38	542	0.55	7.86
<b>7 cycles-3</b>	26.77	543	0.54	7.85
<b>8 cycles-1</b>	25.00	547	0.56	7.66
<b>8 cycles-2</b>	25.13	521	0.58	7.59
<b>8 cycles-3</b>	26.45	548	0.52	7.54
<b>10 cycles-1</b>	15.10	425	0.67	4.30
<b>10 cycles-2</b>	14.87	464	0.70	4.83
<b>10 cycles-3</b>	13.93	426	0.61	3.62

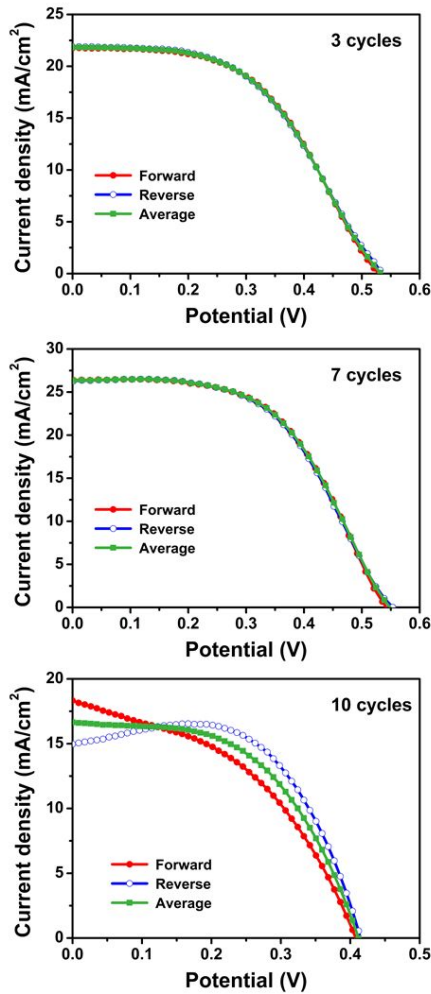


**Figure 3.7** Hysteresis of the  $J-V$  characteristics under illumination (one sun light intensity with AM 1.5G filter) measured in forward (from short circuit to open circuit) and reverse (from open circuit to short circuit) scan direction with a scan rate of 50 mV/s, depending on the number of ZnS SILAR treatment cycles.

**Table 3.4** Summarized  $J$ - $V$  characteristics of the CISE QDSCs with respect to the scan direction

ZnS cycles	Scan direction	$J_{sc}$ (mA/cm <sup>2</sup> )	$V_{oc}$ (mV)	$FF$	$\eta$ (%)
<b>3 cycles</b>	Forward	21.77	529	0.51	5.87
	Reverse	21.89	533	0.50	5.83
	Average	21.83	533	0.50	5.82
<b>7 cycles</b>	Forward	26.31	546	0.54	7.76
	Reverse	26.25	553	0.54	7.84
	Average	26.24	550	0.54	7.79
<b>10 cycles</b>	Forward	18.33	409	0.44	3.30
	Reverse	14.97	416	0.65	4.05
	Average	16.65	412	0.53	3.64

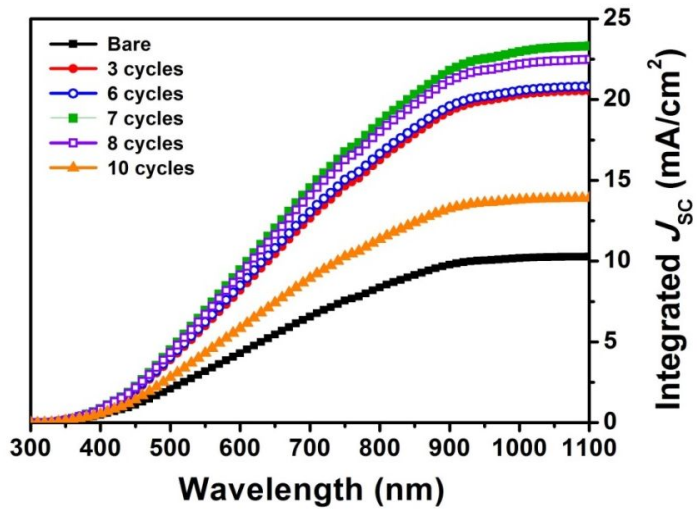


**Figure 3.8** Calculated current density ( $J_{sc}$ ) by integrating the EQE spectra with an AM 1.5 G spectrum.

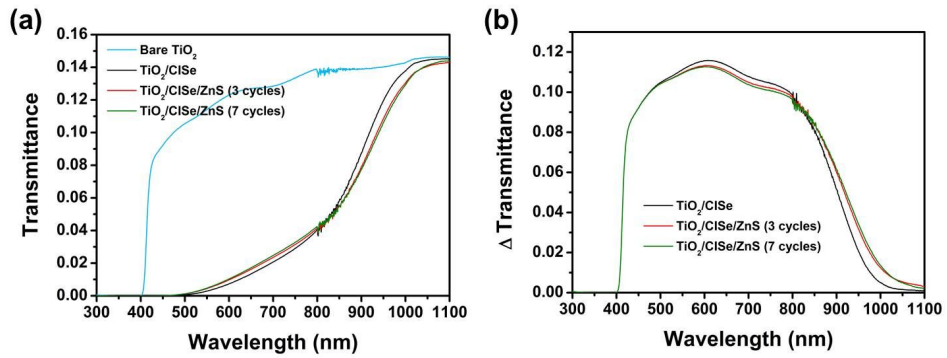


**Figure 3.9** (a) Transmittance spectra of bare and CISE-sensitized TiO<sub>2</sub> films with respect to the number of ZnS SILAR cycles. (b) Transmittance difference between bare TiO<sub>2</sub> film and CISE-sensitized TiO<sub>2</sub> films with respect to the number of ZnS SILAR cycles. Transmittance measurements were performed using an integrating sphere to account for scattering.

### 3.3.3 Control of Carrier Recombination

The influence of thick ZnS overlayers on energetic and kinetic characteristics of the produced electrodes was investigated through electrochemical impedance analysis in a dark state at bias potentials from  $-0.30$  to  $-0.55$  V. The inset of Fig. 3.10a shows the equivalent-circuit model utilized for the fitting of the obtained impedance spectra; the model exhibits a series resistance ( $R_s$ ), followed by impedance at the polysulfide electrolyte/Cu<sub>2</sub>S counter electrode ( $R_{CE}$  and  $CPE_1$ ) and at the polysulfide electrolyte/CISE-sensitized TiO<sub>2</sub> electrode ( $R_{ct}$  and  $CPE_2$ ).<sup>[15]</sup> The  $CPE$  refers to a “constant phase element”, which stands for the interfacial capacitance of rough electrodes.<sup>[15c,d]</sup> Thus the chemical capacitance ( $C_\mu$ ) of the electrodes can be evaluated from  $CPE_2$ . The fitting parameters  $C_\mu$  and interfacial charge transfer resistance ( $R_{ct}$ ) are plotted in Fig. 3.10 as a function of bias potential. As shown in Fig. 3.10a, the electrodes with ZnS overlayers exhibit higher  $C_\mu$  values than the bare electrode at the same bias potential, meaning that the conduction band (CB) potential of the electrode becomes more positive.<sup>[15b,c]</sup> However, the actual number of SILAR cycles seems to make little difference. The different trend for the 10 cycles may be related to the partially blocked pore structure, as shown in the  $J-V$  curve. These results imply that thicker overlayers do not affect the energetics of the photoanode.

A positive shift in the CB potential of the photoanode generally leads to a decrease in the  $V_{OC}$  of the resulting solar cells. However, the  $V_{OC}$  in the  $J-V$  characteristics increases after the overlayers are added. In addition, this effect increases with overlayer thickness, even though the CB potential of the photoanode is not affected. This is therefore likely the result of other factors, such as the flux of injected electrons and changes in electron recombination between the photoanode and the redox couple in the polysulfide electrolyte.<sup>[15e]</sup> Indeed,  $R_{ct}$  clearly increases with the number of SILAR cycles up to a maximum of 7, as shown in Fig. 3.10b, indicating reduced electron recombination rate. Apparently, the thick ZnS overlayers do not affect the energetics of the system, but do enhance the kinetics, which accounts for the improved efficiency compared to the control sample.

Non-radiative losses associated with QDs can also lead to excited photoelectron recombination.<sup>[6e,7b]</sup> We used time decay photoluminescence (PL) to understand the carrier dynamics in the  $TiO_2$ -CISE QDs system; spectra are shown in Fig. 3.11, while the results of the fitting analysis of the decay curves are summarized in Table 3.5. The fitting analysis is carried out using eq 1, which is based on multi-exponential decay behavior, while the average lifetimes ( $\langle\tau\rangle$ ) are determined using eq 2.

$$F(t) = a_1 e^{-t/\tau_1} + a_2 e^{-t/\tau_2} + a_3 e^{-t/\tau_3} \quad (1)$$

$$\langle \tau \rangle = \sum (a_i \tau_i^2) / \sum (a_i \tau_i) \quad (2)$$

There is no self-degradation of the samples during the measurements. Compared to free CISE QDs, all QDs adsorbed on the TiO<sub>2</sub> exhibit significant quenching of emission regardless of the presence of the ZnS overlayers. The carrier lifetime of the QDs-TiO<sub>2</sub> is reduced to about 0.1 ns, whereas that of free QDs is 54.7 ns. The long-lived component, with a  $\tau$  value of 58.2 ns, can be neglected because of its low contribution. These results can be attributed to effective electron injection from excited QD into TiO<sub>2</sub>.<sup>[16a]</sup>

The effect of the ZnS overlayers is clearly observed in decay analysis. Compared to the bare QDs-TiO<sub>2</sub>, the carrier lifetime increases to 1.59 and 2.43 ns for QDs-TiO<sub>2</sub> with 3 and 7 SILAR cycles, respectively. In general, non-radiative carrier recombination in trap sites and electron injection from QDs to TiO<sub>2</sub> both reduce carrier lifetimes. These two contributions are not clearly separated in optical spectroscopy due to the ultrafast time scale of both phenomena. However, because it has been known that the electron injection rate from excited QDs to TiO<sub>2</sub> is not affected by the ZnS overlayers,<sup>[2c]</sup> the increased carrier lifetime can be regarded as changes in

non-radiative recombination of QDs. Since many non-radiative recombination pathways including defect transitions and Auger recombination of trions can contribute to carrier kinetics, the exact specification of the transition is difficult. However, regardless of the type of pathways, the suppression of non-radiative recombination with the thick overlayers is clear in our experimental data. Therefore, the thick overlayers in this study suppress not only interfacial electron recombination with the electrolyte, but non-radiative recombination associated with QDs as well. These two contributions lead to the realization of highly efficient CISE QDSCs.

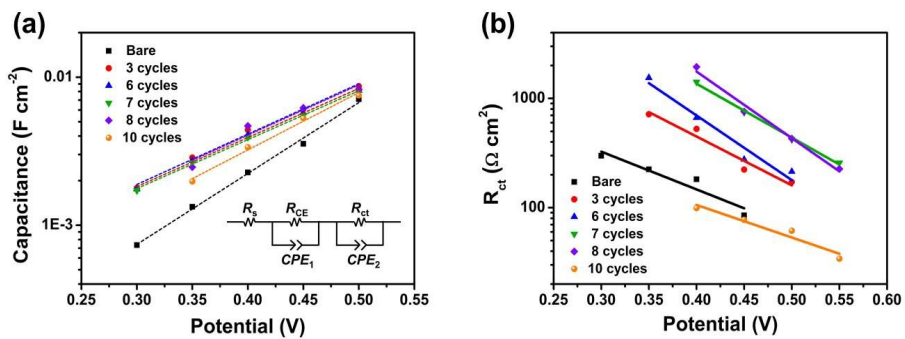


**Figure 3.10** (a) Chemical capacitance and (b) recombination resistance of the CISE-sensitized TiO<sub>2</sub> electrodes with respect to the number of ZnS SILAR cycles, evaluated from impedance spectra taken in the dark state. The inset of (a) shows the equivalent circuit model.

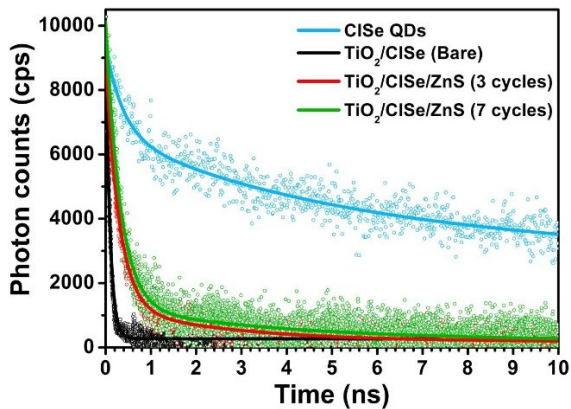


**Figure 3.11** Time decay PL spectra of CISE QDs dispersed in dichloromethane and CISE-sensitized  $\text{TiO}_2$  electrodes with respect to the number of ZnS SILAR cycles. Each experimental decay data (dots) is overlapped with the corresponding fitting curve (lines).

**Table 3.5** PL decay analysis of free CISE QDs, CISE QDs adsorbed on TiO<sub>2</sub> electrodes, and the adsorbed samples with 3 and 7 ZnS SILAR cycles<sup>a</sup>

	CISE QDs	CISE-TiO <sub>2</sub>	CISE-TiO <sub>2</sub> + ZnS (3 cycles)	CISE-TiO <sub>2</sub> + ZnS (7 cycles)
$a_1$	0.29	1.00	0.88	0.89
$\tau_1$ (ns)	0.38	0.09	0.29	0.32
$a_2$	0.32	- <sup>c</sup>	0.12	0.11
$\tau_2$ (ns)	4.53	-	2.61	3.85
$a_3$	0.39	-	-	-
$\tau_3$ (ns)	58.24	-	-	-
$\langle \tau \rangle$ (ns) <sup>b</sup>	54.74	0.09	1.59	2.43
R <sup>2</sup>	0.91	0.94	0.94	0.87

<sup>a</sup>The fitting analysis was carried out using the decay model:

$$F(t) = a_1 e^{-t/\tau_1} + a_2 e^{-t/\tau_2} + a_3 e^{-t/\tau_3}$$

<sup>b</sup>The average lifetimes were determined based on the equation:

$$\langle \tau \rangle = \frac{\sum(a_i \tau_i^2)}{\sum(a_i \tau_i)}$$

<sup>c</sup>The symbol “-” indicates “not available values” because of their low contributions.

### 3.3.4 Comparison Study with Conventional Pb/Cd-based QDSCs

In order to determine whether thick ZnS overlayers can have similar effects on other QDSCs, we fabricated PbS/CdS co-sensitized QD solar cells by the conventional SILAR method.<sup>[8d,e]</sup> The  $J-V$  characteristics of the PbS/CdS QDSCs with respect to ZnS SILAR cycles are shown in Fig. 3.12, while the results are summarized in Table 3.6. As listed, conversion efficiency decreases as the number of cycles increase from 3 to 7, meaning that the effects of thick ZnS overlayers are not applicable for this type of QDSC. In general, interfacial recombination with the electrolyte is dependent on the degree of surface passivation of the TiO<sub>2</sub> electrode. Therefore, the magnitude of QD loading and the QD deposition method<sup>[16b]</sup> can both strongly affect the interfacial recombination rate.<sup>[6a]</sup> In addition, the non-radiative recombination rate depends on the kinds of QDs and their surface states.<sup>[6e,7b]</sup> Overall, this means that it is necessary to investigate and optimize the kind and degree of surface modification for the photoanodes of each solar cell with respect to the type of QD employed.

It has been known that CISE QDs have unique electronic properties compared to other conventional QDs. For example, the Korgel group reported that heterojunction solar cells employing CISE QDs show a large difference in energy between the absorption edge observed in their EQE

spectra and the absorption spectra of CISE QD dispersions due to the significant electronic coupling between neighboring QDs, <sup>[6d]</sup> which is consistent with our results. In addition, the Klimov group found that the films of as-synthesized  $\text{CuInSe}_x\text{S}_{2-x}$  QDs show fairly good p-type charge transport and a strong gating effect despite the presence of bulky native ligands, which are characteristic features compared to other conventional QDs.<sup>[17]</sup> They claimed that the observed charge transport is due to intra-gap surface states of CISE QDs. These unique electronic properties of CISE QDs including strong electronic coupling with neighboring materials and good conductivity may be advantageous for effective electron injection into the  $\text{TiO}_2$  electrode in QDSCs. However, at the same time, these properties may imply that the surface of CISE QDs could act as recombination centers for severe back-charge transfer to the redox species in the electrolyte. As a result, compared to conventional QDs, it may be particularly important to suppress the carrier recombination at the CISE QD surfaces by the much thicker overlayers for their applications in sensitization-type solar cells.

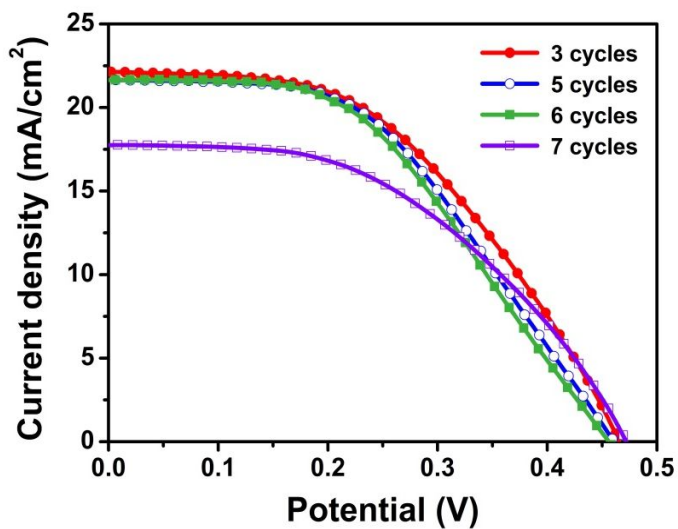


**Figure 3.12**  $J$ - $V$  characteristics under illumination (one sun light intensity with AM 1.5G filter) of the PbS/CdS QDSCs with respect to the number of ZnS SILAR cycles.

**Table 3.6** Summarized  $J$ - $V$  characteristics of the PbS/CdS QDSCs with respect to the number of ZnS SILAR cycles.<sup>a</sup>

ZnS cycles	$J_{sc}$ (mA/cm <sup>2</sup> )	$V_{oc}$ (mV)	$FF$	$\eta$ (%)
<b>3 cycles</b>	21.18	455	0.49	4.72 ± 0.13
<b>5 cycles</b>	21.61	458	0.48	4.75 ± 0.09
<b>6 cycles</b>	21.72	458	0.45	4.48 ± 0.09
<b>7 cycles</b>	17.17	468	0.47	3.78 ± 0.37

<sup>a</sup>All parameters were averaged from three different devices.

### 3.4 Conclusion

In this study, we develop a highly efficient heavy metal-free QDSC using CISE QD-sensitized TiO<sub>2</sub> with precisely controlled ZnS overlayers. The conversion efficiency of the produced QDSC is enhanced by about 40% when the thickness of the overlayer is increased to twice that of a conventional one. The impedance and PL decay data reveals that interfacial electron recombination with the electrolyte and non-radiative recombination associated with QDs are significantly reduced by introducing the thick ZnS overlayer, explaining the significant enhancement in photovoltaic performance. This yields a remarkable conversion efficiency of 8.10% under one sun illumination, a record for heavy metal-free QD solar cells at the current (Oct., 2015). However, these effects can not be transferred to other types of QDSCs; the decreased performance of a tested PbS/CdS co-sensitized QD solar cell indicates the need to determine optimized surface modifications for individual QD solar cell systems. The results exhibit a great advancement in technology, and facilitate important insight into the development of highly efficient heavy-metal-free QD solar cells.

\*\*Parts of this chapter were published in the article, “Highly Efficient Copper-Indium-Selenide Quantum Dot Solar Cells: Suppression of Carrier

Recombination by Controlled ZnS Overlayers.” *ACS Nano* **2015**, *9*, 11286.

### 3.5 References

- [1] (a) Murray, C. B.; Norris, D. J.; Bawendi, M. G. *J. Am. Chem. Soc.* **1993**, *115*, 8706. (b) Peng, X.; Manna, L.; Yang, W.; Wickham, J.; Scher, E.; Kadavanich, A.; Alivisatos, A. P. *Nature* **2000**, *404*, 59. (c) Rogach, A. L.; Eychmüller, A.; Hickey, S. G.; Kershaw, S. V. *Small* **2007**, *3*, 536. (d) Manna, L.; Milliron, D. J.; Meisel, A.; Scher, E. C.; Alivisatos, A. P. *Nat. Mater.* **2003**, *2*, 382. (e) Singh, A.; Singh, A.; Ciston, H.; Bustillo, K.; Nordlund, D.; Milliron, D. *J. Am. Chem. Soc.* **2015**, *137*, 6464.
- [2] (a) Robel, I.; Subramanian, V.; Kuno, M.; Kamat, P. V. *J. Am. Chem. Soc.* **2006**, *128*, 2385. (b) Lee, H.; Wang, M.; Chen, P.; Gamelin, D. R.; Zakeeruddin, S. M.; Grätzel, M.; Nazeeruddin, M. K. *Nano Lett.* **2009**, *9*, 4221. (c) Zhao, K.; Pan, Z.; Mora-Seró, I.; Cánovas, E.; Wang, H.; Song, Y.; Gong, X.; Wang, J.; Bonn, M.; Bisquert, J.; Zhong, X. *J. Am. Chem. Soc.* **2015**, *137*, 5602. (d) Kongkanand, A.; Tvrđy, K.; Takechi, K.; Kuno, M.; Kamat, P. V. *J. Am. Chem. Soc.* **2008**, *130*, 4007. (e) Yun, H. J.; Paik, T.; Edley, M. E.; Baxter, J. B.; Murray, C. B. *ACS Appl. Mater. Interfaces* **2014**, *6*, 3721. (f) Panthani, M. G.; Kurley, J. M.; Crisp, R. W.; Dietz, T. C.; Ezzyat, T.; Luther, J. M.; Talapin, D. V. *Nano Lett.* **2014**, *14*, 670. (g)

MacDonald, B. I.; Martucci, A.; Rubanov, S.; Watkins, S. E.; Mulvaney, P.; Jasieniak, J. J. *ACS Nano* **2012**, *6*, 5995.

[3] (a) Lee, J.-W.; Son, D.-Y.; Ahn, T. K.; Shin, H.-W.; Kim, I. Y.; Hwang, S.-J.; Ko, M. J.; Sul, S.; Han, H.; Park, N.-G. *Sci. Rep.* **2013**, *3*, 1050. (b) McDonald, S. A.; Konstantatos, G.; Zhang, S.; Cyr, P. W.; Klem, E. J. D.; Levina, L.; Sargent, E. H. *Nat. Mater.* **2005**, *4*, 138. (c) Chuang, C.-H. M.; Brown, P. R.; Bulovic, V.; Bawendi, M. G. *Nat. Mater.* **2014**, *13*, 796. (d) Chuang, C.-H. M.; Maurano, A.; Brandt, R. E.; Hwang, G. W.; Jean, J.; Buonassisi, T.; Bulovic, V.; Bawendi, M. G. *Nano. Lett.* **2015**, *15*, 3286. (e) Labelle, A. J.; Thon, S. M.; Masala, S.; Adachi, M. M.; Dong, H.; Farahani, M.; Ip, A. H.; Fratilocchi, Sargent, E. H. *Nano Lett.* **2015**, *15*, 1101. (f) Lee, J.-W.; Hong, J.-D.; Park, N.-G. *Chem. Comm.* **2013**, *49*, 6448.

[4] (a) Nozik, A. J.; Beard, M. C.; Luther, J. M.; Law, M.; Ellingson, R. J.; Johnson, J. C. *Chem. Rev.* **2010**, *110*, 6873. (b) Semonin, O. E.; Luther, J. M.; Choi, S.; Chen, H.-Y.; Gao, J.; Nozik, A. J.; Beard, M. C. *Science*, **2011**, *334*, 1530. (c) Nair, G.; Chang, L.-Y.; Geyer, S. M.; Bawendi, M. G. *Nano Lett.* **2011**, *11*, 2145. (d) Stolle, C. J.; Harvey, T. B.; Pernik, D. R.; Hibbert, J. I.; Du, J.; Rhee, D. J.; Akhavan, V. A.; Schaller, R. D.;

- Korgel, B. A. *J. Phys. Chem. Lett.* **2014**, *5*, 304. (e) Stolle, C. J.; Schaller, R. D.; Korgel, B. A. *J. Phys. Chem. Lett.* **2014**, *5*, 3169.
- [5] (a) Murray, C. B.; Kagan, C. R.; Bawendi, M. G. *Science* **1995**, *270*, 1335. (b) Huynh, W. U.; Dittmer, J. J.; Alivisatos, A. P. *Science* **2002**, *295*, 2425. (c) Talapin, D. V.; Murray, C. B. *Science* **2005**, *310*, 86. (d) Talapin, D. V.; Lee, J.-S.; Kovalenko, M. V.; Shevchenko, E. V. *Chem. Rev.* **2010**, *110*, 389. (e) Choi, M. K.; Yang, J.; Kang, K.; Kim, D. C.; Choi, C.; Park, C.; Kim, S. J.; Chae, S. I.; Kim, T.-H.; Kim, J. H.; Hyeon, T.; Kim, D.-H. *Nat. Commun.* **2015**, *6*, 7149.
- [6] (a) Yang, J.; Kim, J.-Y.; Yu, J. H.; Ahn, T.-Y.; Lee, H.; Choi, T.-S.; Kim, Y.-W.; Joo, J.; Ko, M. J.; Hyeon, T. *Phys. Chem. Chem. Phys.* **2013**, *15*, 20517. (b) Panthani, M. G.; Akhavan, V.; Goodfellow, B.; Schmidtke, J. P.; Dunn, L.; Dodabalapur, A.; Barbara, P. F.; Korgel, B. A. *J. Am. Chem. Soc.* **2008**, *130*, 16770. (c) Akhavan, V. A.; Goodfellow, B. W.; Panthani, M. G.; Reid, D. K.; Hellebusch, D. J.; Adachi, T.; Korgel, B. A. **2010**, *3*, 1600. (d) Panthani, M. G.; Stolle, C. J.; Reid, D. K.; Rhee, D. J.; Harvey, T. B.; Akhavan, V. A.; Yu, Y.; Korgel, B. A. *J. Phys. Chem. Lett.* **2013**, *4*, 2030. (e) McDaniel, H.; Fuke, N.; Makarov, N. S.; Pietryga, J. M.; Klimov, V. I. *Nat. Commun.* **2013**, *4*, 2887. (f) Pan, Z.; Mora-Seró, I.; Shen, Q.; Zhang, H.; Li, Y.; Zhao, K.; Wang, J.; Zhong, X.; Bisquert, J. J.

*Am. Chem. Soc.* **2014**, *136*, 9203. (g) Li, W.; Pan, Z.; Zhong, X. *J. Mater.*

*Chem. A* **2015**, *3*, 1649.

- [7] (a) Guijarro, N.; Campiña, J. M.; Shen, Q.; Toyoda, T.; Lana-Villarreal, T.; Gómez, R. *Phys. Chem. Chem. Phys.* **2011**, *13*, 12024. (b) Shen, Q.; Kobayashi, J.; Diguna, L. J.; Toyoda, T. *J. Appl. Phys.* **2008**, *103*, 084304. (c) Santra, P. K.; Kamat, P. V. *J. Am. Chem. Soc.* **2012**, *134*, 2508.
- [8] (a) Koo, H.-J.; Yoo, P. B.; Yoo, K.; Kim, K.; Park, N.-G. *Inorg. Chim. Acta* **2008**, *361*, 677. (b) Giménez, S.; Mora-Seró, I.; Macor, L.; Guijarro, N.; Lana-Villarreal, T.; Gómez, R.; Diguna, L. J.; Shen, Q.; Toyoda, T.; Bisquert, J. *Nanotechnology* **2009**, *20*, 295204. (c) Ito, S.; Nazeeruddin, M. K.; Liska, P.; Comte, P.; Charvet, R.; Péchy, P.; Jirousek, M.; Kay, A.; Zakeeruddin, S. M.; Grätzel, M. *Prog. Photovoltaics* **2006**, *14*, 589. (d) Zhou, N.; Chen, G.; Zhang, X.; Cheng, L.; Luo, Y.; Li, D.; Meng, Q. *Electrochem. Commun.* **2012**, *20*, 97. (e) Braga, A.; Giménez, S.; Concina, I.; Vomiero, A.; Mora-Seró, I. *J. Phys. Chem. Lett.* **2011**, *2*, 454.
- [9] (a) Tauc, J. *Amorphous and Liquid Semiconductor*; Plenum Press; New York, 1974. (b) David, E. A.; Mott, N. F. *Philos. Mag.* **1970**, *22*, 903.
- [10] (a) Ollinger, M.; Craciun, V.; Singh, R. K. *Appl. Phys. Lett.* **2002**, *80*, 1927. (b) Xu, J. F.; Ji, W.; Lin, J. Y.; Tang, S. H.; Du, Y. W. *Appl. Phys. A* **1998**, *66*, 639.

- [11] (a) Tsao, H. N.; Comte, P.; Yi, C.; Grätzel, M. *ChemPhysChem* **2012**, *13*, 2976. (b) Yoon, I.-N.; Song, H.-K.; Won, J.; Kang, Y. S. *J. Phys. Chem. C* **2014**, *118*, 3918. (c) Heo, J. H.; Han, H. J.; Kim, D.; Ahn, T. K.; Im, S. H. *Energy Environ. Sci.* **2015**, *8*, 1602.
- [12] <http://rredc.nrel.gov/solar/spectra/aml.5> (accessed September 23th 2015)
- [13] (a) Hegedus, S. S.; Shafarman, W. N. *Prog. Photovoltaics* **2004**, *12*, 155. (b) Lim, Y. S.; Jeong, J.; Kim, J. Y.; Ko, M. J.; Kim, H.; Kim, B.; Jeong, U.; Lee, D.-K. *J. Phys. Chem. C* **2013**, *117*, 11930. (c) Hwang, K.-J.; Jeong, Y.; Park, D.-W. *Appl. Phys. Lett.* **2015**, *106*, 143502.
- [14] (a) Yang, P.; Ando, M.; Taguchi, T.; Murase, N. *J. Phys. Chem. C* **2011**, *115*, 14455. (b) Yang, S.; Prendergast, D.; Neaton, J. B. *Nano Lett.* **2010**, *10*, 3156. (c) Dabbousi, B. O.; Rodriguez-Viejo, J.; Mikulec, F. V.; Heine, J. R.; Mattoussi, H.; Ober, R.; Jensen, K. F.; Bawendi, M. G. *J. Phys. Chem. B* **1997**, *101*, 9463.
- [15] (a) Fabrgat-Santiago, F.; Garcia-Belmonte, G.; Mora-Seró, I.; Bisquert, J. *J. Phys. Chem. Chem. Phys.* **2011**, *13*, 9083. (b) Lee, M.-W.; Kim, J.-Y.; Son, H. J.; Kim, J. Y.; Kim, B.; Kim, H.; Lee, D.-K.; Kim, K.; Lee, D.-H.; Ko, M. J. *Sci. Rep.* **2015**, *5*, 7711. (c) Kim, J.-Y.; Kim, J. Y.; Lee, D.-K.; Kim, B.; Kim, H.; Ko, M. J. *J. Phys. Chem. C* **2012**, *116*, 22759. (d) Longo, C.; Nogueira, A. F.; Paoli, M. A. D.; Cachet, H. *J. Phys. Chem. B*

**2002**, *106*, 5925. (e) Boschloo, G.; Hagfeldt, A. *Acc. Chem. Res.* **2009**, *42*, 1819.

[16] (a) Bang, J. H.; Kamat, P. V. *ACS Nano*, **2009**, *3*, 1467. (b) Rühle, S.; Shalom, M.; Zaban, A. *ChemPhysChem* **2010**, *11*, 2290.

[17] Draguta, S.; McDaniel, H.; Klimov, V. I. *Adv. Mater.* **2015**, *27*, 1701.

# **Chapter 4. Synthesis and Characterization of Mn<sup>2+</sup>-doped CdSe Clusters: The Smallest Doped Semiconductor**

## **4.1 Introduction**

For the last decades, the synthesis of semiconductor nanocrystals (NCs) have been rapidly developed from controlling the size<sup>[1]</sup> and shape<sup>[2]</sup> to designing various multicomponent heterostructures for synergetic combination of the quantum confinement effect with the traditional semiconductor technology such as heterojunction and doping. In particular, doping semiconductor NCs with magnetic transition metals have attracted substantial interests to obtain diluted magnetic semiconductor (DMS) NCs. Spin exchange interaction between the dopants and the charge carriers of the host in these NCs leads to unique correlated electronic and magnetic properties such as giant magneto-optical response. So far synthesis of various kinds of doped semiconductor NCs have been reported.<sup>[3-6]</sup> Despite the progress on the doping of semiconductor NCs, the study of doped semiconductor NCs is limited to NCs larger than 2 nm. Typically, doping of

NCs is known to be induced by the adsorption of impurities on the surface of growing NCs.<sup>[6]</sup> Because this process requires the preformed NCs of certain sizes for adsorption of the dopant, there is almost no chance for the dopants to be incorporated into the very small-sized NCs. Thus, it is an open question whether doping of sub-nanometer sized semiconductor is feasible at all.

In this chapter, we report on the synthesis and characterization of  $\text{Mn}^{2+}$ -doped CdSe clusters. It has been known that magic-sized CdSe clusters are formed transiently before the nucleation and growth of CdSe NCs.<sup>[7]</sup> By adjusting the reaction conditions, we successfully obtained single-sized CdSe clusters doped with  $\text{Mn}^{2+}$  with 99% yield. Mass spectrum reveals that molecular formula of these clusters is  $\text{Cd}_{13-x}\text{Mn}_x\text{Se}_{13}$  ( $x = 1, 2$ ), corresponding to the doping concentration of 7.7 and 15.4% for  $x = 1$  and 2, respectively. Although the clusters have very small size, they have the semiconductor band structure, which highlights them as the smallest doped semiconductors. These clusters show multiple excitonic transitions with different magneto-optical activities, which might correspond to the fine structure states. Magneto-optically active states exhibit magneto-optical responses up to 128 K and huge  $g$ -factor of  $81(\pm 8)$  at 4 K. This work demonstrates that sub-nanometer sized doped clusters can be obtained, which

represents magnetically doped semiconductors in extremely strong confinement regime.

## 4.2 Experimental Sections

### 4.2.1 Synthesis of Mn<sup>2+</sup>-doped CdSe Clusters

The method is modified from that of CdSe quantum nanoribbons.<sup>[2c,d]</sup> All reactions were conducted under argon (Ar) atmosphere using standard Schlenk technique. In a typical synthesis, a solution containing MCl<sub>2</sub>(*n*-octylamine)<sub>2</sub> complexes (M = Cd, Mn) was prepared by heating 10 mL of *n*-octylamine (99%, Sigma-Aldrich) containing 1.5 mmol (0.275 g) of CdCl<sub>2</sub> (anhydrous, 99.999%, Sigma-Aldrich) and 0.15 mmol (0.018 g) of MnCl<sub>2</sub> (anhydrous, 99.999%, Sigma-Aldrich) at 120 °C for 2 h. Octylammonium selenocarbamate was prepared by bubbling CO gas into 5 mL of *n*-octylamine containing 4.5 mmol (0.355 g) of Se powder (99.99%, Sigma-Aldrich) for 1 h at room temperature. The as-prepared octylammonium selenocarbamate solution was injected into the metal precursor solution at room temperature. For the complete conversion of the precursor to the clusters, the reaction is required to be conducted more than 40 h. The products were precipitated by adding ethanol containing trioctylphosphine followed by washing several times with ethanol. The other amines can also be used as the ligands to control

the reaction kinetics. For example, when we used propylamine instead of octylamine, the reaction time for the complete conversion was decreased to less than 3 h. The current method can be easily scaled-up by simply using a large amount of the precursors.

Short-chain amine passivated clusters are not well-dispersible because of their 2D self-assembled super-structure, which prevent precise measurement of optical and magneto-optical properties. Thus, surface modification of the clusters was performed to improve dispersibility of the clusters. In the typical process, 0.1 mmol of the as-synthesized octylamine-stabilized clusters were mixed with 10 mL of oleylamine, and subsequently ultra-sonication was performed for 2 h. Then, the products were precipitated by adding ethanol and then re-dispersed in nonpolar solvents such as toluene and chloroform.

#### **4.2.2 Basic Characterization**

The average doping concentration and stoichiometry of the clusters were characterized by inductively coupled plasma-atomic emission spectrometry (ICP-AES, Shimadzu ICPS-7500). The reaction yield was determined by combining thermogravimetric analysis (TGA) and ICP-AES. The optical absorption spectra were obtained using CARY 5000E UV-VIS-NIR spectrophotometer. Photoluminescence (PL), photoluminescence excitation

(PLE) and time resolved decay spectra were measured by FLS 980 spectrometer (Edinburgh Instruments). For PL and PLE, the clusters were excited with a steady-state Xenon lamp, and the emitted photons were detected by single photon counting photomultiplier. For the decay kinetics, the clusters were excited with a pulsed Xenon flash-lamp, and the emitted photons were detected by a micro-channel plate photomultiplier tube (MCP-PMT). Low temperature absorption data of the undoped clusters were measured by a Shimadzu UV-2550 spectrometer, while for low temperature PL measurements the undoped clusters were placed in a closed-cycle cryostat from Oxford instruments (Cryomech PT403/CP830) and excited with the 325 nm line (cw) of a Helium-Cadmium laser. The PL spectra were collected with a monochromator (Horiba iHR320) and a nitrogen cooled CCD (Horiba, Symphony II).

#### **4.2.3 Control Experiment for Formation Mechanism**

Undoped CdSe clusters were synthesised using the same procedure using CdCl<sub>2</sub> as a sole metal precursor. Mn precursor solution was prepared by heating 5 ml of *n*-octylamine containing 0.75 mmol (0.094 g) of MnCl<sub>2</sub> at 120 °C for 2 hours. 1 ml of the Mn precursor solution was injected to the solution of the as-synthesized undoped (CdSe)<sub>13</sub> clusters with or without

additional Se precursor, and the resulting reaction mixture was kept at room temperature for several hours. The products were precipitated by adding ethanol containing trioctylphosphine followed by washing several times with ethanol.

#### 4.2.4 LDI-TOF MS Analysis

LDI-TOF MS is one of the powerful tools for investigating small-sized NCs.<sup>[7k,1]</sup> LDI-TOF MS was performed on a Voyager-DE<sup>TM</sup> STR Biospectrometry Workstation (Applied Biosystems Inc.). We performed experiments in a negative ion mode without adding any matrix. Mass calibration was performed using protein standards. We found that surface passivating amines are detached by laser and halide ion could be used as an efficient ionization source instead of the matrix. For effective ionization, we measured MS of unpurified clusters containing a trace amount of halide ions. When we used iodine instead of chlorine, the  $m/z$  value of the base peak increased to the theoretical mass of  $[(\text{CdSe})_{13}+\text{I}]^-$  (Fig. S1), showing that the mass difference was owing to the halide ion, which was used as the ionization source. Desorption and ionization of the clusters were achieved by absorbing pulsed  $\text{N}_2$  laser (337 nm, 3 ns pulses). The spectra were measured with the laser between 40% and 70% of the full power. Theoretical isotope

distribution was calculated by the software, mMass 4.5.<sup>[8]</sup> When we calculated the isotopic patterns, FWHM (full width at half maximum) of each peak was set as 0.6.

#### **4.2.5 Magnetic Circular Dichroism Measurements**

Magnetic circular dichroism (MCD) spectra were obtained using a self-made setup. To minimize the light scatterings, oleylamine capped clusters were used for the measurements. The excitation source is a 75 W Xenon lamp followed by a monochromator (LOT Oriel, 1200 grooves/mm grating, blazed at 350 nm). The modulation of the light between right and left circular polarization at a frequency of 50 kHz was realized using a combination of a linear polarizer and a photoelastic modulator. The sample was cooled by helium vapour in a Janis ST-300 cryostat placed between two poles of an electromagnet in Faraday geometry, allowing the variation of the applied magnetic field up to 1.6 T. A photomultiplier (model R928, Hamamatsu) detects both, the DC and AC components of the transmitted light, which are proportional to  $T(\sigma^+) + T(\sigma^-)$  and  $T(\sigma^+) - T(\sigma^-)$ , respectively. The measurement of the DC (AC) component is realized using a multimeter (HP 34401A) and a lock-in amplifier (Signal Recovery 7225 DSP).

## 4.3 Result and Discussion

### 4.3.1 Synthesis of Mn<sup>2+</sup>-doped CdSe Clusters

The synthesis of Mn<sup>2+</sup>-doped CdSe clusters is performed by adding selenocarbamate to a solution containing CdCl<sub>2</sub> and MnCl<sub>2</sub> in octylamine, which leads to the formation of octylamine capped CdSe clusters via Lewis acid-base reaction between the metal halide-amine complex and the selenium precursor.<sup>[2c,d]</sup> Further reaction to form CdSe NCs from the clusters is suppressed by lowering the reaction temperature to 25 °C. By changing the coordinating ligands, we can control the reaction kinetics or the dispersibility of the clusters. Our method is very simple and reliable so that it can be easily scaled up to obtain more than a hundred grams from a single batch reaction in nearly quantitative yield (~99%, the inset of Fig. 4.1a).

The CdSe clusters obtained were analysed by laser desorption/ionization time of flight (LDI-TOF) mass spectrometry (MS) and the result is shown in Fig. 4.1. The measurement was conducted in negative ion mode, the samples were ionized by Cl<sup>-</sup>. The three main peaks in the mass spectrum are unambiguously assigned to Cd<sub>13</sub>Se<sub>13</sub>, Cd<sub>12</sub>MnSe<sub>13</sub>, and Cd<sub>11</sub>Mn<sub>2</sub>Se<sub>13</sub> (Fig. 1b). Other clusters such as (CdSe)<sub>34</sub> or (CdSe)<sub>19</sub> are not detected,<sup>[7f,g]</sup> confirming the high purity of the products. When no Mn precursor is added to the

reaction solution, the clusters synthesized show only  $\text{Cd}_{13}\text{Se}_{13}$  peak in the mass spectrum (Fig. 4.2). As a result, MS data confirm that our samples are  $(\text{CdSe})_{13}$  clusters with one or two  $\text{Cd}^{2+}$  replaced with  $\text{Mn}^{2+}$  ( $\text{Cd}_{13-x}\text{Mn}_x\text{Se}_{13}$  ( $x = 1, 2$ )). Although there are only two kinds of  $\text{Mn}^{2+}$ -doped clusters with exact doping concentrations (7.7% and 15.4%), the *average* doping concentration ( $x_{\text{Mn}}$ ) of the product from each synthesis is continuously increased from 0% to 10% with the amount of the Mn precursor in the solution (Fig. 4.3). This indicates that the molar ratio of  $\text{Cd}_{13}\text{Se}_{13}$ ,  $\text{Cd}_{12}\text{MnSe}_{13}$ , and  $\text{Cd}_{11}\text{Mn}_2\text{Se}_{13}$  clusters in the product is dependent on  $[\text{Mn}^{2+}]$  in the reaction solution.

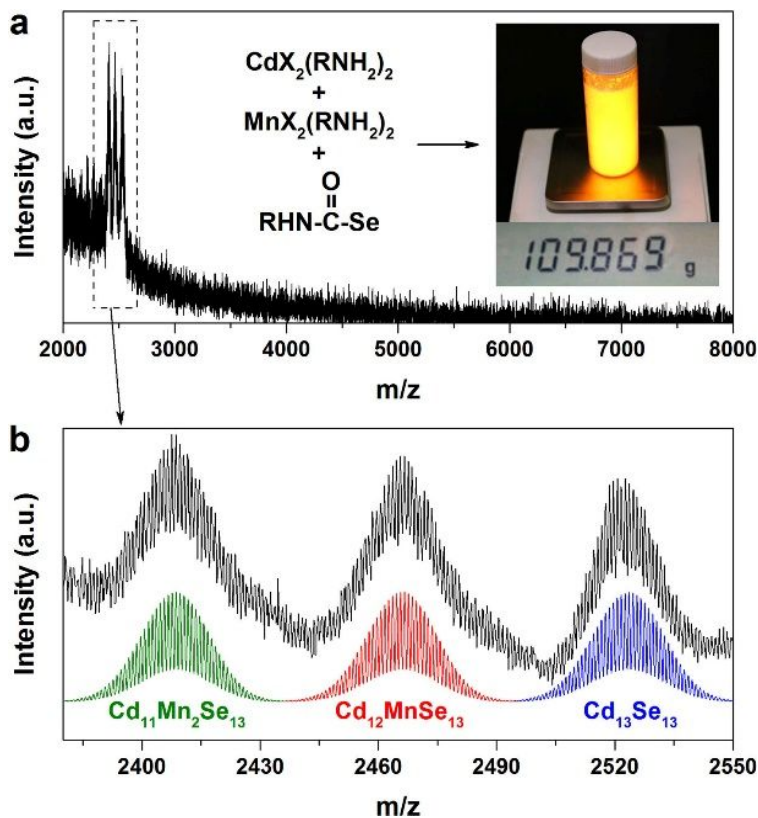


**Figure 4.1** (a) Mass spectrum of  $\text{Mn}^{2+}$ -doped CdSe clusters ionized with  $\text{Cl}^-$  ( $x_{\text{Mn}} = 7\%$ ). The inset shows the amount of the product from a single batch large-scale synthesis. (b) High resolution mass spectrum of the main peaks indicated with the dashed box in panel a. Below the measured data, calculated isotopic distributions of  $\text{Cd}_{13}\text{Se}_{13}$  (blue),  $\text{Cd}_{12}\text{MnSe}_{13}$  (red), and  $\text{Cd}_{11}\text{Mn}_2\text{Se}_{13}$  (green) are shown for comparison.

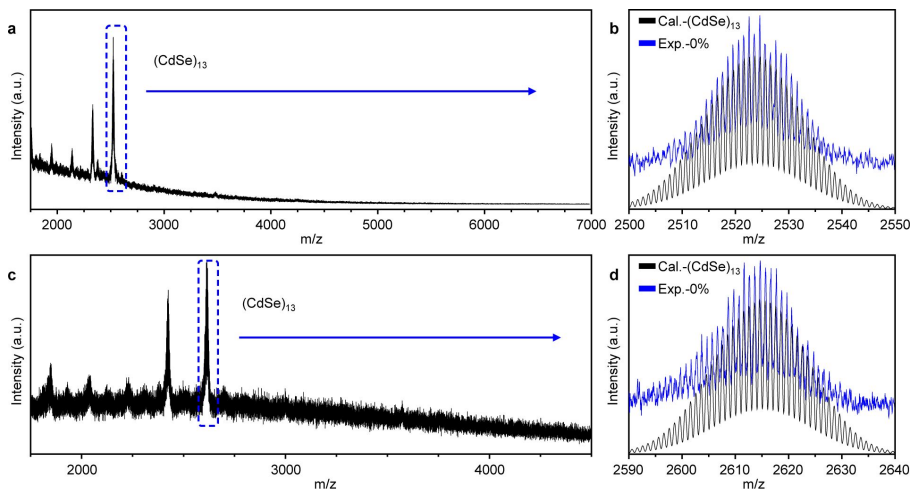


**Figure 4.2** (a) Mass spectrum of undoped CdSe clusters ionized by Cl<sup>-</sup>. (b) The expansion around the main peak in panel a (blue rectangle) in isotopic resolution. For comparison, the experimental data (blue line) are shown with the calculated isotopic distribution (black line). Peaks from other CdSe clusters, such as (CdSe)<sub>34</sub> or (CdSe)<sub>19</sub> are not observed. Minor peaks result from the fragmentation by laser. (c) Mass spectrum of undoped CdSe clusters ionized by I<sup>-</sup>. (d) The expansion around the main peak in panel c (blue rectangle) in isotopic resolution. For comparison, the experimental data (blue line) are shown with the calculated isotopic distribution (black line). Minor peaks result from the fragmentation by laser.

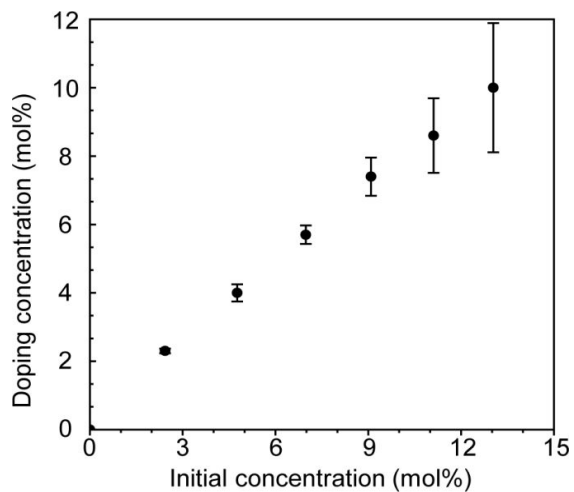


**Figure 4.3** Average doping concentrations of the clusters determined by inductively coupled plasma-atomic emission spectrometry. Molar concentrations of  $\text{Mn}^{2+}$  in  $\text{Mn}^{2+}$ -doped clusters are marked as dots according to the initial molar concentrations of  $\text{MnCl}_2$ .

### 4.3.2 Optical Characterization

The electronic energy structure of the clusters was investigated by optical spectroscopy. In Fig. 4.4a, absorption spectrum shows band edge excitonic transitions around 350 nm (3.54 eV), which is significantly blue-shifted from the band gap of bulk CdSe (1.75 eV) due to the strong quantum confinement. The absorption signal for the wavelength between 350 and 500 nm is influenced by scattering processes, which can be minimized by ligand exchange with long-chain unsaturated amines. In the photoluminescence (PL) spectrum, the band edge emission at 365 nm observed from undoped (CdSe)<sub>13</sub> clusters (Fig. 4.5) is suppressed. Instead, an intense emission around 600 nm is observed, which is attributed to the internal (<sup>4</sup>T<sub>1</sub>-<sup>6</sup>A<sub>1</sub>) Mn<sup>2+</sup> transition. Photoluminescence excitation (PLE) spectrum of this emission exhibits nearly the same transitions as the absorption spectrum, confirming the energy transfer from the host semiconductor band states to Mn<sup>2+</sup> states. These data prove that Mn<sup>2+</sup> is sitting in a Cd<sup>2+</sup> site with tetrahedral site symmetry of the hosts.<sup>[9]</sup> The shift between the maxima of PLE and absorption spectra can be attributed to different fine structure states contributing to each signal, as discussed below using magneto-optical studies. Interestingly, temperature-dependent shift of the absorption edge of the clusters is well fitted with Varshni's law (Fig. 4.4b).<sup>[9c]</sup> This suggests that

these clusters have the semiconductor band structure in spite of their extremely small size, which highlights them as the smallest doped inorganic semiconductor reported so far.

As the average doping concentration is increased from 0% to 10%, the absorption peak position is shifted by  $\sim 43$  meV, which is another evidence of doping that affects the band structure of the host (Fig. 4.4c).<sup>[9b]</sup> In addition, as the doping concentration increases, the lifetime of internal ( ${}^4T_1-{}^6A_1$ )  $Mn^{2+}$  transition rapidly decreases (Fig. 4.4d).<sup>[9b,c]</sup> For the clusters with the intermediate doping concentration of 7%, the decay curve fits well to a double exponential with  $\tau_1 = 23$   $\mu$ sec and  $\tau_2 = 143$   $\mu$ sec. On the other hand, for 10% doped clusters, single exponential decay with  $\tau = 19$   $\mu$ sec gives the best fit (Fig. 4.6). This result suggests that  $Cd_{12}MnSe_{13}$  and  $Cd_{11}Mn_2Se_{13}$  have slow ( $>100$   $\mu$ sec) and fast ( $<50$   $\mu$ sec) decay rates, respectively, and that the statistical distribution of each species in an ensemble is changed according to the average doping concentration. The shortening of the decay time with increasing  $Mn^{2+}$ -concentration might indicate a partial lifting of the spin selection rules in exchange coupled  $Mn^{2+}$  pairs.<sup>[9c]</sup> Moreover, the lattice distortion caused by doping possibly increases non-radiative losses. This is supported by the trend that the quantum yield (QY) decreases with

increasing average doping concentration: QY = 10%, 8%, and 6% for  $x_{\text{Mn}}$  = 4%, 7%, and 10%, respectively.

Simple control experiment using optical spectroscopy as monitoring tools gives some clues on how doping proceeds. When we added the manganese precursor solution into the as-synthesised  $(\text{CdSe})_{13}$  dispersion, no doped clusters were detected in the optical spectrum (Fig. 4.5b), suggesting that  $(\text{CdSe})_{13}$  clusters are not subject to doping via either a cation exchange mechanism<sup>[3d,e]</sup> or a general growth-controlled process<sup>[6]</sup>.

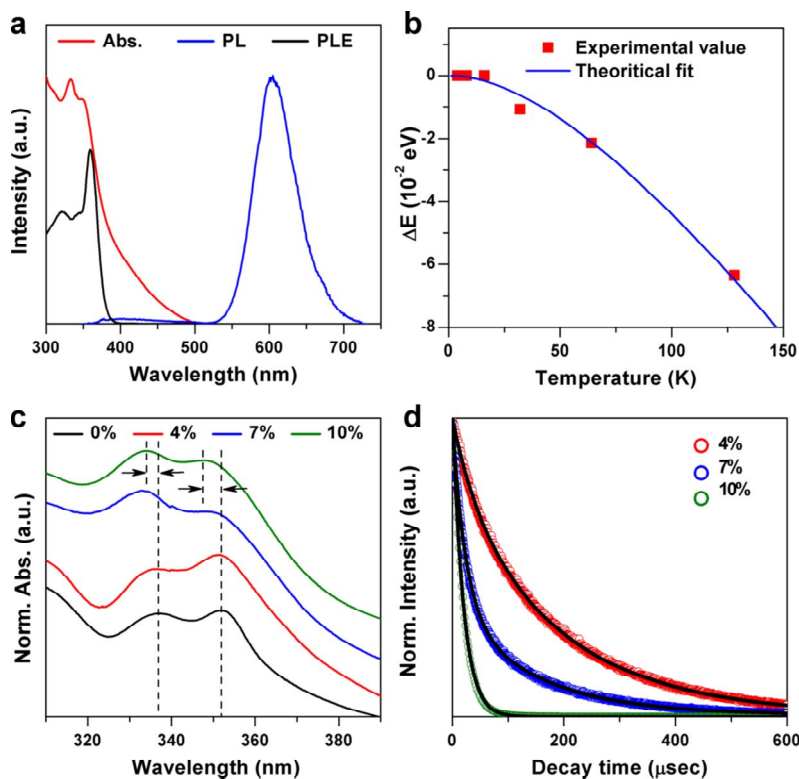


**Figure 4.4** (a) Spectra of absorption, photoluminescence, and photoluminescence excitation (detected at 600 nm) from as-synthesized (*n*-octylamine capped) clusters ( $x_{\text{Mn}} = 7\%$ ). (b) Energy shift of the absorption edge as a function of temperature. The theoretical fitting curve is calculated by using the Varshni law with the parameters  $\alpha = 11 \times 10^{-4} \text{ eV K}^{-1}$  and  $\beta = 150 \text{ K}$ . (c) Absorption spectra of the clusters. (d) Time-resolved luminescence decay at 600 nm. Each data is overlapped with the fitting curves (black).

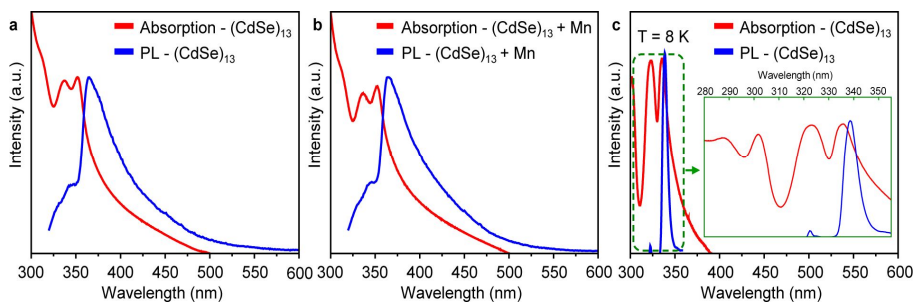


**Figure 4.5** Optical properties of the undoped clusters. (a-b) Room temperature absorption (red) and photoluminescence (PL) (blue) spectra of the undoped clusters (a) and the product from the reaction of as-synthesized undoped (CdSe)<sub>13</sub> clusters and Mn precursor (b). These two sets of absorption and PL spectra are nearly identical, showing that Mn<sup>2+</sup> cannot be doped into the as-synthesized (CdSe)<sub>13</sub> clusters. (c) Low temperature (8 K) absorption (red) and PL spectra (blue) of undoped (CdSe)<sub>13</sub>. The area in the green box is magnified in the inset. The undoped clusters show very sharp band-edge excitonic transition. In contrast, small nanoparticles with crystal disorder generally show very broad optical transitions.<sup>[10]</sup> A small peak at ~323 nm in the PL is caused by the excitation source.

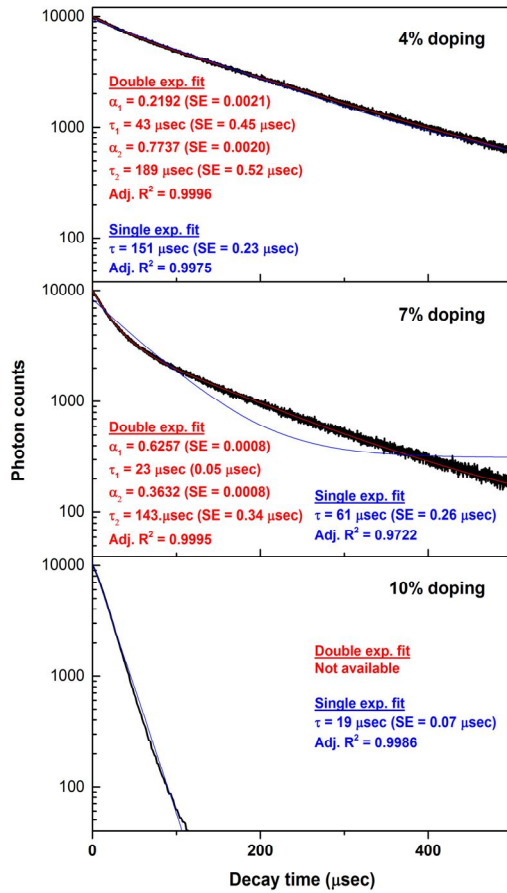


**Figure 4.6** Time-resolved photoluminescence decay data from Fig. 2d (black) and their double exponential (red) and single exponential (blue) fit curves. The fit equations are  $I = I_0[\alpha_1 \exp(-t/\tau_1) + \alpha_2 \exp(-t/\tau_2)]$  for double exponential and  $I = I_0 \exp(-t/\tau)$  for single exponential. For 10% doping data, a double exponential fit does not converge.

### 4.3.3 Magneto-Optical Property

It is of fundamental interest whether these doped clusters can exhibit characteristics of magnetically doped semiconductors.<sup>[2d,5]</sup> A pronounced magnetic circular dichroism (MCD) signal is observed (Fig. 4.7). This indicates a strong coupling between the charge carriers of the host material and the substitutional  $\text{Mn}^{2+}$ -dopants,<sup>[4b]</sup> proving the membership of this material to the family of DMS nanostructures. In our experiments the ground state in the absorption process (zero exciton) is a non-degenerate spin zero state<sup>[1a,5b]</sup> and does not split in a magnetic field. Therefore, the resulting MCD signal is determined by the A term of the MCD signal and thus proportional to the first derivative of the absorbance. For that reason, the zero-crossing of the MCD spectrum should be located at the same energy as the absorption maximum. Indeed, this is usually observed for DMS.<sup>[4,5]</sup> Surprisingly, a different result is found in this work (Fig. 4.7a). The number of zero-crossings suggests that the measured MCD signals consist of three different magneto-optically active transitions. Because of the mismatch between the energy positions of the MCD zero-crossings and the absorption maxima, there should be at least two magneto-optically inactive transitions.

Indeed, we can resolve multiple excitonic transitions in the absorption spectrum (Fig. 4.7a). Following the theoretical study of Efros *et al.*,<sup>[1a]</sup> the

eight-fold degenerated band-edge energy level is expected to split into five sublevels – labelled by “new” quantum numbers  $\pm 2$ ,  $\pm 1^L$ ,  $0^L$ ,  $\pm 1^U$ , and  $0^U$ . The magneto-optically active peaks at 3.60 eV and at 3.79 eV might be related to the  $\pm 1^L$  and  $\pm 1^U$  states, respectively (violet lines in Fig. 4.7a). The magneto-optically inactive transitions at 3.70 eV and 3.86 eV might involve  $0^{L/U}$  states, which do not split under an external magnetic field (black dashed lines in Fig. 4.7a). The low energy contribution to the absorption signal at  $\sim 3.4$  eV is possibly correlated to the  $\pm 2$  state. Its contribution to the MCD signal, however, can be neglected, because of the selection rules and the low oscillator strength of this optically passive state. The optical transition around 4.1 eV involves upper excited states. It should be noted that the above notation of the fine structure split energy states is derived from a theoretical study based on the envelope function model,<sup>[1a]</sup> which means that quantitative details (*e.g.*, exact energy levels) cannot be simply extrapolated towards these ultra-small clusters. Independent from the limitations of the envelope function model, the occurrence of magneto-optically active and magneto-optically inactive transitions becomes obvious from our experimental data (Fig. 4.7a and Fig. 4.8).

By excluding magneto-optically inactive transitions (See the red curve in Fig. 4.7a, where the new absorption maxima show the same energy as the

MCD zero-crossings.), we can extract the giant Zeeman splitting of  $\text{Mn}^{2+}$ -doped clusters (Fig. 4.7b). The experimental values for the effective  $g$ -factor of the 4%  $\text{Mn}^{2+}$ -doped clusters are  $81(\pm 8)$  and  $-8(\pm 1)$  for the  $\pm 1^L$  and  $\pm 1^U$  states, respectively; those of the 10%  $\text{Mn}^{2+}$ -doped clusters are  $63(\pm 18)$  and  $-6(\pm 2)$  for the  $\pm 1^L$  and  $\pm 1^U$  states, respectively. These huge  $g$ -factors (at least 60 times greater than in the case of undoped CdSe nanocrystals<sup>[11a]</sup>) clearly indicate substantial exchange coupling between the localized  $3d$ -electrons of the manganese and delocalized band charge carriers in the conduction and valence band. Note that the  $g$ -factors are still small compared to record data obtained on DMS nanocrystals, where the highest experimentally achieved  $g_{\text{eff}}$  is of order of  $907^{\text{[11b]}}$  (at 1.8 K and  $x_{\text{Mn}} = 29\%$ , corresponding to a  $g_{\text{eff}}$  of  $\sim 390$  at 4.2 K). In our studies we still have undoped clusters within an ensemble, which contribute to the total absorption but not to the magneto-optical activity, resulting in a reduction of the extracted Zeeman splitting. Moreover in the extremely small structures studied here, the quantum confinement is expected to affect both the spin-spin exchange interaction between the charge carriers and the dopants<sup>[2d,5b,c]</sup> as well as the valence-band mixing,<sup>[1a,11c]</sup> possibly leading to a decrease of the magneto-optical response. The 10%  $\text{Mn}^{2+}$ -doped clusters exhibit a slightly lower Zeeman splitting than the 4% doped ones. This result points to the formation of

antiferromagnetically coupled  $\text{Mn}^{2+}$ - $\text{Mn}^{2+}$  pairs in  $\text{Cd}_{11}\text{Mn}_2\text{Se}_{13}$  clusters that are the major products when the average doping concentration is high. In addition, we observed a MCD signal up to 128 K for the 4% doped clusters (Fig. 4.7c). The decrease of the MCD amplitude with increasing temperature can be fitted well with a Brillouin equation (Fig. 4.7d). This provides another strong evidence that the origin of the magneto-optical activity is the exchange coupling between the semiconductor charge carriers and the spins of the dopant ions.<sup>[11d]</sup>

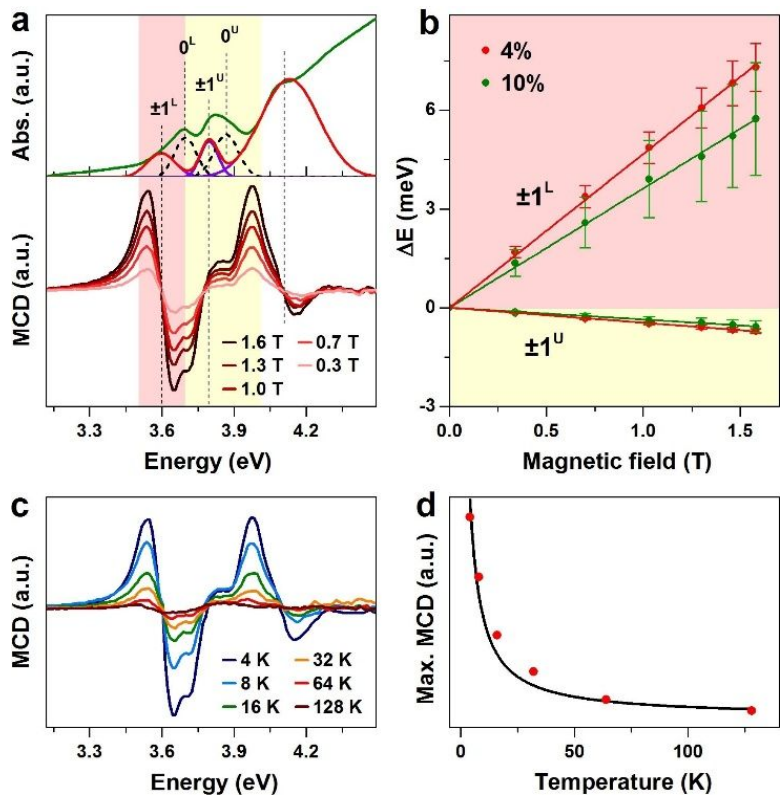


**Figure 4.7** (a) Absorption (upper) and MCD (lower) spectra 4.2 K ( $x_{\text{Mn}} = 4\%$ ). In the upper panel, green, violet, and black dashed lines indicate measured data, magneto-optically active, and inactive peaks, respectively. The red curve is the summation of the magneto-optically active transitions. (b) Giant Zeeman splittings extracted from 4% (red) and 10% (green) Mn<sup>2+</sup>-doped clusters. (c) Temperature-dependent MCD spectra ( $x_{\text{Mn}} = 4\%$ ) under the magnetic field of 1.6 T. (d) Maximum amplitude of the MCD signal in panel c as a function of temperature. The black curve represents a theoretical Brillouin fit.

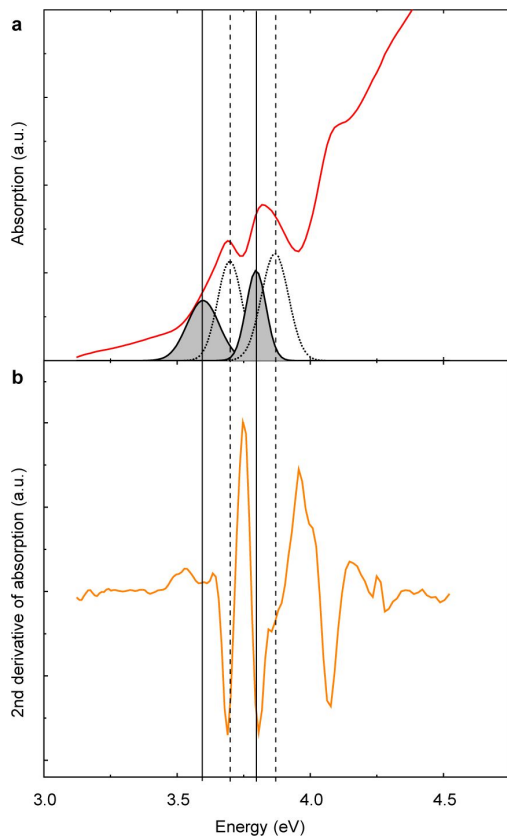


**Figure 4.8** Determination of the absorption peak maxima. (a) Raw absorption data with the fitted peaks and (b) second derivative of the absorption data. The lines indicate the center energy of the fitted peaks. The grey peaks are the magneto-optically active ones, while the magneto-optically inactive ones are represented by the dashed peaks.

## 4.4 Conclusion

In summary, we present a successful magnetic doping of CdSe clusters that produces the smallest dilute magnetic semiconductor. Not only do our results uncover a previously unknown pathway for the nanoscale doping process, but they also improve the understanding of the doped semiconductors at the interface of molecules and quantum dots, which paves the way for future applications of nanoscale spin-based devices.

\*\*Parts of this chapter were published in the article, “Route to the Smallest Doped Semiconductor:  $\text{Mn}^{2+}$ -Doped  $(\text{CdSe})_{13}$  clusters.” *Journal of the American Chemical Society* **2015**, *137*, 12776.

## 4.5 References

- [1] (a) Efros, Al. L.; Rosen, M.; Kuno, M.; Nirmal, M.; Norris, D. J.; Bawendi, M. *Phys. Rev. B* **1996**, *54*, 4843. (b) Murray, C. B.; Norris, D. J.; Bawendi, M. G. *J. Am. Chem. Soc.* **1993**, *115*, 8706. (c) Lee, J.-S.; Stoeva, S. I.; Mirkin, C. A. *J. Am. Chem. Soc.* **2006**, *128*, 8899. (d) Talapin, D. V.; Lee, J.-S.; Kovalenko, M. V.; Shevchenko, E. V. *Chem. Rev.* **2010**, *110*, 389. (e) Kovalenko, M. V.; Cabot, A.; Manna, L.; Hens, Z.; Talapin, D. V.; Kagan, C. R.; Klimov, V. I.; Rogach, A.; Reiss, P.; Milliron, D.; Guyot-Sionnest, P.; Konstantatos, G.; Parak, W. J.; Hyeon, T.; Korgel, B. A.; Murray, C. B.; Heiss, W. *ACS Nano* **2015**, *9*, 1012.
- [2] (a) Peng, X. G.; Manna, L.; Yang, W.; Wickham, J.; Scher, E.; Kadavanich, A.; Alivisatos, A. P. *Nature* **2000**, *404*, 59. (b) Manna, L.; Milliron, D. J.; Meisel, A.; Scher, E. C.; Alivisatos, A. P. *Nat. Mater.* **2003**, *2*, 382. (c) Joo, J.; Son, J. S.; Kwon, S. G.; Yu, J. H.; Hyeon, T. *J. Am. Chem. Soc.* **2006**, *128*, 5632. (d) Yu, J. H.; Liu, X.; Kweon, K. E.; Joo, J.; Park, J.; Ko, K. T.; Lee, D. W.; Shen, S.; Tivakornsasithorn, K.; Son, J. S.; Park, J. H.; Kim, Y. W.; Hwang, G. S.; Dobrowolska, M.; Furdyna, J. K.; Hyeon, T. *Nat. Mater.* **2010**, *9*, 47. (e) Ithurria, S.; Tessier, M. D.; Mahler, B.; Lobo, R. P. S. M.; Dubertret, B.; Efros, Al. L. *Nat. Mater.* **2011**, *10*, 936. (f) Liu, Y.-H.;

Wang, F.; Wang, Y.; Gibbons, P. C.; Buhro, W. E. *J. Am. Chem. Soc.* **2011**, *133*, 17005.

[3] (a) Shim, M.; Guyot-Sionnest, P. *Nature* **2000**, *407*, 981. (b) Yu, D.; Wang, C.; Guyot-Sionnest, P. *Science* **2003**, *300*, 1277. (c) Talapin, D. V.; Murray, C. B. *Science* **2005**, *310*, 86. (d) Mocatta, D.; Cohen, G.; Schattner, J.; Millo, O.; Rabani, E.; Banin, U. *Science* **2011**, *332*, 77. (e) Sahu, A.; Kang, M. S.; Kompch, A.; Notthof, C.; Wills, A. W.; Deng, D.; Winterer, M.; Frisbie, C. D.; Norris, D. J. *Nano Lett.* **2012**, *12*, 2587. (f) Ye, X.; Hickey, D. R.; Fei, J.; Diroll, B. T.; Paik, T.; Chen, J.; Murray, C. B. *J. Am. Chem. Soc.* **2014**, *136*, 5106.

[4] (a) Mikulec, F. V.; Kuno, M.; Bennati, M.; Hall, D. A.; Griffin, R. G.; Bawendi, M. G. *J. Am. Chem. Soc.* **2000**, *122*, 2532. (b) Norris, D. J.; Yao, N.; Charnock, F. T.; Kennedy, T. A. *Nano Lett.* **2001**, *1*, 3. (c) Pradhan, N.; Goorskey, D.; Thessing, J.; Peng, X. *J. Am. Chem. Soc.* **2005**, *127*, 17586. (d) Wang, F.; Han, Y.; Lim, C. S.; Lu, Y.; Wang, J.; Xu, J.; Chen, H.; Zhang, C.; Hong, M.; Liu, X. *Nature* **2010**, *463*, 1061. (e) Yu, J. H.; Kwon, S.-H.; Petrášek, Z.; Park, O. K.; Jun, S. W.; Shin, K.; Choi, M.; Park, Y. I.; Park, K.; Na, H. B.; Lee, N.; Lee, D. W.; Kim, J. H.; Schwille, P.; Hyeon, T. *Nat. Mater.* **2013**, *12*, 359. (f) Whitham, P. J.; Knowles, K. E.; Reid, P. J.; Gamelin, D. R. *Nano Lett.* **2015**, *15*, 4045.

- [5] (a) Beaulac, R.; Schneider, L.; Archer, P. I.; Bacher, G.; Gamelin, D. R. *Science* **2009**, *325*, 973. (b) Bussian, D. A.; Crooker, S. A.; Yin, M.; Brynda, M.; Efros, Al. L.; Klimov, V. I. *Nat. Mater.* **2009**, *8*, 35. (c) Fainblat, R.; Frohleiks, J.; Muckel, F.; Yu, J. H.; Yang, J.; Hyeon, T.; Bacher, G. *Nano Lett.* **2012**, *12*, 5311. (d) Ochsenbein, S. T.; Feng, Y.; Whitaker, K. M.; Badaeva, E.; Liu, W. K.; Li, X.; Gamelin, D. R. *Nat. Nanotech.* **2009**, *4*, 681. (e) Awschalom, D. D.; Flatté, M. E. *Nat. Phys.* **2007**, *3*, 153. (f) Pandey, A.; Brovelli, S.; Viswanatha, R.; Li, L.; Pietryga, J. M.; Klimov, V. I.; Crooker S. A. *Nat. Nanotech.* **2012**, *7*, 792.
- [6] (a) Erwin, S. C.; Zu, L.; Haftel, M. I.; Efros, Al. L.; Kennedy, T. A.; Norris, D. J. *Nature* **2005**, *436*, 91. (b) Bryan, J. D.; Gamelin, D. R. *Prog. Inorg. Chem.* **2005**, *54*, 47. (c) Norris, D. J.; Efros, Al. L.; Erwin, S. C. *Science* **2008**, *319*, 1776. (d) Santangelo, S. A.; Hinds, E. A.; Vlaskin, V. A.; Archer, P. I.; Gamelin, D. R. *J. Am. Chem. Soc.* **2007**, *129*, 3973. (e) Du, M.-H.; Erwin, S. C.; Efros, A. L. *Nano Lett.* **2008**, *8*, 2878. (f) Buonsanti, R.; Milliron, D. J. *Chem. Mater.* **2013**, *25*, 1305.
- [7] (a) Herron, N.; Calabrese, J. C.; Farneth, W. E.; Wang Y. *Science* **1993**, *259*, 1426. (b) Vossmeier, T.; Reck, G.; Schulz, B.; Haupt, E. T. H.; Weller, H. *Science* **1995**, *267*, 1476. (c) Alivisatos, A. P. *Science* **1996**, *271*, 933. (d) Kudera, S.; Zanella, M.; Giannini, C.; Rizzo, A.; Li, Y.; Gigli, G.; Cingolani,

R.; Ciccarella, G.; Spahl, W.; Parak, W. J.; Manna, L. *Adv. Mater.* **2007**, *19*, 548. (e) Soloviev, V. N.; Eichhofer, A.; Fenske, D.; Banin, U. *J. Am. Chem. Soc.* **2000**, *122*, 2673. (f) Kasuya, A.; Sivamohan, R.; Barnakov, Y. A.; Dmitruk, I. M.; Nirasawa T.; Romanyuk, V. R.; Kumar, V.; Mamykin, S. V.; Tohji, K.; Jeyadevan, B.; Shinoda, K.; Kudo, T.; Terasaki, O.; Liu, Z.; Belosludov, R. V.; Sundararajan, V.; Kawazoe, Y. *Nat. Mater.* **2004**, *3*, 99. (g) Wang, Y.; Liu, Y.-H.; Zhang, Y.; Wang, F.; Kowalski, P. J.; Rohrs, H. W.; Loomis, R. A.; Gross, M. L.; Buhro, W. E. *Angew. Chem. Int. Ed.* **2012**, *51*, 6154. (h) Beecher, A. N.; Yang, X.; Palmer, J. H.; LaGrassa, A. L.; Juhas, P.; Billinge, S. J. L.; Owen, J. S. *J. Am. Chem. Soc.* **2014**, *136*, 10645. (i) Evans, C. M.; Love, A. M.; Weiss, E. A. *J. Am. Chem. Soc.* **2012**, *134*, 17298. (j) Zhang, J.; Rowland, C.; Liu, Y.; Xiong, H.; Kwon, S.; Shevchenko, E.; Schaller, R. D.; Prakapenka, V. B.; Tkachev, S.; Rajh, T. *J. Am. Chem. Soc.* **2015**, *137*, 742. (k) Kim, B. H.; Shin, K.; Kwon, S. G.; Jang, Y.; Lee, H.-S.; Lee, H.; Jun, S. W.; Lee, J.; Han, S. Y.; Yim, Y.-H.; Kim, D.-H.; Hyeon, T. *J. Am. Chem. Soc.* **2013**, *135*, 2407. (l) Dass, A.; Stevenson, A.; Dubay, G. R.; Tracy, J. B.; Murray, R. W. *J. Am. Chem. Soc.* **2008**, *130*, 5940.

[8] Strohmalm, M.; Kavan, D.; Novák, P.; Volný, M.; Havlíček, V. *Anal. Chem.* **2010**, *82*, 4648.

- [9] (a) Beaulac, R.; Archer, P. I.; Liu, X.; Lee, S.; Salley, G. M.; Dobrowolska, M.; Furdyna, J. K.; Gamelin, D. R. *Nano Lett.* **2008**, *8*, 1197. (b) Na, C.W.; Han, D. S.; Kim, D. S.; Kang, Y. J.; Lee, J. Y.; Park, J.; Oh, D. K.; Kim, K.S.; Kim, D. *J. Phys. Chem. B* **2006**, *110*, 6699. (c) Suyver, J. F.; Wuister, S. F.; Kelly, J. J.; Meijerink, A. *Phys. Chem. Chem. Phys.* **2000**, *2*, 5445. (d) Beaulac, R.; Ochsenein, S. T.; Gamelin, D. R. in *Nanocrystal Quantum Dots*; Klimov, V. I., Ed.; CRC Press: Boca Raton, FL, 2010.
- [10] Chen, X.; Samia, A. C. S.; Lou, Y.; Burda, C. *J. Am. Chem. Soc.* **2005**, *127*, 4372.
- [11] (a) Kuno, M.; Nirmal, M.; Bawendi, M. G.; Efros, Al.; Rosen, M. *J. Chem. Phys.* **1998**, *108*, 4242. (b) Vlaskin, V. A.; Barrows, C. J.; Erickson, C. S.; Gamelin, D. R. *J. Am. Chem. Soc.* **2013**, *135*, 14380. (c) Fainblat, R.; Muckel, F.; Barrows, C. J.; Vlaskin, V. A.; Gamelin, D. R.; Bacher, G. *ACS Nano* **2014**, *8*, 12669. (d) Gaj, J. A.; Planel, R.; Fishmann, G. *Solid State Comm.* **1979**, *29*, 435.

# Bibliography

## 1. International Publications

### First Author Papers

- 1) Franziska Muckel\*, **Jiwoong Yang\***, Severin Lorenz, Woonhyuk Baek, Hogeun Chang, Taeghwan Hyeon, Gerd Bacher, Rachel Fainblat  
“Digital Doping in Magic-Sized CdSe Clusters.”  
*ACS Nano* **2016**, accepted. (\*co-first author)
- 2) Jisoo Lee\*, **Jiwoong Yang\***, Soon Gu Kwon, Taeghwan Hyeon  
“Nonclassical Nucleation and Growth of Inorganic Nanoparticles.”  
*Nature Reviews Materials* **2016**, *1*, 16034. (\*co-first author)
- 3) **Jiwoong Yang**, Moon Kee Choi, Dae-Hyeong Kim, Taeghwan Hyeon  
“Designed Assembly and Integration of Colloidal Nanocrystals for Device Applications.”  
*Advanced Materials* **2016**, *28*, 1176.
- 4) Jae-Yup Kim\*, **Jiwoong Yang\***, Jung Ho Yu, Woonhyuk Baek, Chul-Ho Lee, Hae Jung Son, Taeghwan Hyeon, Min Jae Ko  
“Highly Efficient Copper–Indium–Selenide Quantum Dot Solar Cells: Suppression of Carrier Recombination by Controlled ZnS Overlayers.”  
*ACS Nano* **2015**, *9*, 11286. (\*co-first author)
- 5) **Jiwoong Yang**, Rachel Fainblat, Soon Gu Kwon, Franziska Muckel, Jung

Ho Yu, Hendrik Terlinden, Byung Hyo Kim, Dino Iavarone, Moon Kee Choi, In Young Kim, Inchul Park, Hyo-Ki Hong, Jihwa Lee, Jae Sung Son, Zonghoon Lee, Kisuk Kang, Seong-Ju Hwang, Gerd Bacher, Taeghwan Hyeon

“Route to the Smallest Doped Semiconductor: Mn<sup>2+</sup>-Doped (CdSe)<sub>13</sub> Clusters.”

*Journal of the American Chemical Society* **2015**, *137*, 12776.

- 6) Moon Kee Choi\*, **Jiwoong Yang**\*, Kwanghun Kang, Dong Chan Kim, Changsoon Choi, Chaneui Park, Seok Joo Kim, Sue In Chae, Tae-Ho Kim, Ji Hoon Kim, Taeghwan Hyeon, Dae-Hyeong Kim

“Wearable Red-Green-Blue Quantum Dot Light-Emitting Diode Array Using High-Resolution Intaglio Transfer Printing.”

*Nature Communications* **2015**, *6*, 7149. (\*co-first author)

- 7) **Jiwoong Yang**, Jae Sung Son, Jung Ho Yu, Jin Joo, Taeghwan Hyeon

“Advances in the Colloidal Synthesis of Two-Dimensional Semiconductor Nanoribbons.”

*Chemistry of Materials* 2013, *25*, 1190.

- 8) **Jiwoong Yang**, Jae-Yup Kim, Jung Ho Yu, Tae-Young Ahn, Hyunjae Lee, Tae-Seok Choi, Young-Woon Kim, Jin Joo, Min Jae Ko, Taeghwan Hyeon

“Copper–Indium–Selenide Quantum Dot-Sensitized Solar Cells.”

*Physical Chemistry Chemical Physics*, **2013**, *15*, 20517.

**Co-author papers**

- 9) Vinayak S. Kale, Uk Sim, **Jiwoong Yang**, Kyoungsuk Jin, Sue In Chae, Woo Je Chang, Arun Kumar Sinha, Heonjin Ha, Chan-Cuk Hwang, Junghyun An, Hyo-Ki Hong, Zonghoon Lee, Ki Tae Nam and Taeghwan Hyeon  
“Sulfur-Doped Graphitic Carbon Nitride Nanogeodes for Oxygen Evolution Electrocatalysts.”  
**2016**, Submitted.
- 10) Donghee Son, Sue In Chae, Myungbin Kim, Moon Kee Choi, **Jiwoong Yang**, Kunsu Park, Vinayak S. Kale, Ja Hoon Koo, Changsoon Choi, Minbaek Lee, Ji Hoon Kim, Taeghwan Hyeon, Dae-Hyeong Kim  
“Colloidal Synthesis of Uniform-Sized Molybdenum Disulfide Nanosheets for Wafer-Scale Flexible Nonvolatile Memory.”  
*Advanced Materials* **2016**, Under Revision.
- 11) Moon Kee Choi, Inhyuk Park, Dong Chan Kim, Eehyung Joh, Ok Kyu Park, Jaemin Kim, Myungbin Kim, Changsoon Choi, **Jiwoong Yang**, Kyoung Won Cho, Jae-Ho Hwang, Jwa-Min Nam, Taeghwan Hyeon, Ji Hoon Kim, Dae-Hyeong Kim

“Thermally Controlled, Patterned Graphene Transfer Printing for Transparent and Wearable Electronic/Optoelectronic System.”

*Advanced Functional Materials* **2015**, 25, 7109.

- 12) Rachel Fainblat, Julia Frohleiks, Franziska Muckel, Jung Ho Yu, **Jiwoong Yang**, Taeghwan Hyeon, Gerd Bacher

“Quantum Confinement-Controlled Exchange Coupling in Manganese (II)-Doped CdSe Two-Dimensional Quantum Well Nanoribbons.”

*Nano Lett.* **2012**, 12, 5311.

- 13) Jae Sung Son, Kunsu Park, Soon Gu Kwon, **Jiwoong Yang**, Moon Kee Choi, Junhyeong Kim, Jung Ho Yu, Jin Joo, Taeghwan Hyeon

“Dimension-Controlled Synthesis of CdS Nanocrystals: From 0D Quantum Dots to 2D Nanoplates.”

*Small* **2012**, 8, 2394.

## **2. Awards**

- 1) Best Student Award by Seoul National University (February, 2011).
- 2) Material Research Society 2016 Spring Meeting Best Poster Award by MRS (March, 2016).
- 3) Best Research Award by Seoul National University & Donjin Co. (June, 2016).

## 국문 초록 (Abstract in Korean)

나노 물질의 다양한 응용을 위해서는 잘 설계된 합성과 물질 분석이 중요하다. 최근, 더욱 뛰어난 물성과 다양한 기능성을 가지는 다원자종을 포함하는 나노 물질로 나노 화학의 관심사가 옮겨가고 있다. 이러한 측면에서 I-III-VI 반도체 물질과 도핑된 II-VI 반도체 물질은 기초 과학 연구와 미래 응용에 있어 중요한 대표적인 물질군이다. 본 학위 논문에서는 산-염기 반응을 이용한 삼성분계 셀렌화 반도체 양자 나노구조의 합성과 그 분석에 대해 다루었다. 크기 조절이 가능한 Cu-In-Se 양자점의 합성, 분석 및 광발전 특성 향상을 위한 표면개질 방법에 대해 논의하였다. 또한, 망간 이온(II)이 도핑된 매우 작은 CdSe 나노클러스터의 합성과 그 성질에 대해 조명해 보았다.

첫째로, 대표적인 I-III-VI 반도체 물질인 Cu-In-Se 양자점을 합성하였으며 크기에 따른 성질 변화를 연구하였다. 본 합성법에서는 셀레노카바메이트를 셀레늄 전구체로 사용하여 2 nm에서 10 nm 크기의 균일한 크기의 양자점을 얻을 수 있었다. 양자점의 크기에 따라 광흡수와 TiO<sub>2</sub>로의 전자 전달이 효율적으로 이루어지도록 에너

지 준위가 조절 가능하였다. 이러한 에너지 준위 개질에 따른 태양 전지 특성을 체계적으로 연구하였다. 가장 효율적인 양자점의 크기는 대략 4 nm 정도로, 중금속을 사용하지 않고도 표준 조건에서 4.30%의 광에너지 변환 효율을 얻을 수 있었다.

두번째로, 광전극의 표면 개질에 따른 전하 운반체의 재결합 억제를 통한 Cu-In-Se 양자점의 광발전 특성 향상에 대해 조명하였다. 양자점-TiO<sub>2</sub> 전극의 ZnS 보호층의 두께를 다양하게 조절하여 광에너지 변환 효율을 향상 시킬 수 있었다. 두꺼운 ZnS 보호층을 사용할 때 전극의 에너지 특성은 유지된 반면, 전해질과의 전자 재결합과 양자점에서의 비방사 재결합이 모두 억제되었다. 결과적으로 8.10%의 광에너지 변환효율을 얻었으며 이는 중금속이 포함되지 않은 양자점 태양전지에서 최고의 변환 효율이다(2015년 10월 기준).

끝으로, 망간 이온 (II) 이 도핑된 CdSe 클러스터의 합성과 분석에 대해 논의하였다. 질량 분석법을 통해 도핑된 클러스터들은 Cd<sub>13</sub>·<sub>x</sub>Mn<sub>x</sub>Se<sub>13</sub> (x = 0, 1, 2)의 화학식을 가짐을 확인할 수 있었다. 또한, 균일한 크기의 도핑된 클러스터를 대량으로 합성할 수 있었다. 이 클러스터들은 매우 작은 크기에도 불구하고 묽은 자성 반도체의 특성

을 지니고 있었다. 서로 다른 자기분광학적 활성을 지닌 다중 엑시톤 전이를 보여주었는데 이는 반도체 에너지 구조의 미세구조 분열과 연관이 있다고 볼 수 있다. 그리하여 자기분광학적으로 활성화된 상태의 경우  $81(\pm 8)$  유효  $g$  인자에 해당하는 거대 지만 분열을 나타내었다. 본 연구 결과는 도핑된 나노물질을 얻는 새로운 방법을 제시할 뿐만 아니라 분자와 양자점 경계상에 있는 도핑된 반도체 물질의 성질을 이해하는데 의의가 있다고 볼 수 있다.

**Keywords:** 삼성분계 셀렌화 반도체, 양자 나노구조, 셀렌화 구리 인듐, 광발전, 셀렌화 카드뮴 클러스터, 도핑, 뭍은 자성 반도체.

학 번: 2011-22922